Effect of an adhesive layer on the mode I delamination in unidirectional CFRP bonded joints

THÈSE Nᵒ 7858 (2017)

PRÉSENTÉE LE 22 SEPTEMBRE 2017
À LA FACULTÉ DES SCIENCES ET TECHNIQUES DE L'INGÉNIEUR
LABORATOIRE DE MÉCANIQUE APPLIQUÉE ET D'ANALYSE DE FIABILITÉ
PROGRAMME DOCTORAL EN MÉCANIQUE

ÉCOLE POLYTECHNIQUE FÉDÉRALE DE LAUSANNE

POUR L'OBTENTION DU GRADE DE DOCTEUR ÈS SCIENCES

PAR

Nassima NASRI

acceptée sur proposition du jury:

Dr M. Farhat, président du jury
Prof. J. Botsis, Dr J. Cugnoni, directeurs de thèse
Prof. D. Karalekas, rapporteur
Prof. M. Alfano, rapporteur
Prof. D. Pioletti, rapporteur

ÉCOLE POLYTECHNIQUE
FÉDÉRALE DE LAUSANNE

Suisse
2017

« Le plus grand bonheur de l'étude consiste à trouver les raisons soi-même. »
René Descartes

Acknowledgements

First of all I thank Prof. John Botsis, for giving me the opportunity to carry out my thesis under his supervision and for making available all the necessary means to complete this thesis at the LMAF. He guided my work during the past four years, and was extremely available for discussions.

I would also like to express my heartfelt gratitude to Dr. Joël Cugnoni, my thesis co-adviser, for all the invaluable scientific discussions, the out-of-the-box solutions, and the intense problem solving sessions. I will always remember your remarkable expertise, your kindness, your patience; I realize I owe you so much. It was indeed a pleasure working with you.

I would like to thank the jury committee members of my defense, Prof. Dominique Pioletti, Dr. Mohammed Farhat, Prof. Dimitris Karalekas, and Prof. Marco Alfano for kindly accepting to participate in the examination and for sharing their interesting comments.

I am also grateful to my colleagues Anne Legrand, Marco Lai, Marco Piccinini, Laurent Humbert, Matteo Galli, Ehsan Sarfaraz Roohollah, Ebrahim Farman-Ashtiani who was also my office mate, for the friendly atmosphere in the lab. I particularly enjoyed the "very efficient" French-Italian tandem sessions with Marco Borotto, the never ending discussions about everything that improved my argumentation skills with Georgios Pappas, the first April jokes and the late reprisal with Robin Amacher (I also thank him a lot for his hilarious conversations, and his positive thinking). Many thanks to Guillaume Frossard for all the valuable discussions, and for helping me mounting the mode I testing set up every time I came with sports injuries... Many thanks to Prof. Thomas Gmür for saving me from some boring conversations, but also for giving me a wonderful example of what a professor can be.

My dear friend Vahid, I was extremely fortunate to meet you. Thank you so much for you kindness, your amazing discussions, and your invaluable friendship.

I am not sure I would have completed this thesis without the incommensurable help from Viviane Magnenat, the secretary of the lab. Thank you so much for sharing with me all the keys for a successful and healthy life. You improved my well-being in so many ways. You're one of the most interesting and helpful person I have ever met.

A special thank goes to my closest friend and neighbour Kadja Kardiatou. Thank you for your support, your kindness and your wisdom. Whenever I was sick, sad, or desperate, you've been there for me. I cannot imagine how I could ever have accomplished this thesis without your help.

During my thesis I had the chance to supervise student projects and I would like to thank some of them: Jeff, Olivier, Martin, Florian, Franck, Mélanie, Edouard and Lucien. You guys made teaching a truly enriching experience. I also enjoyed the time spent on building rockets with the dream team Eric, Jonathan, Héloïse, Maxime, Emilien, and their team leader John Stevenson, who will be for sure a great manager in the near future.

I am very grateful to Marc Jeanneret, first for teaching me in great details how to design a set up, and how to make a good 3D model with Catia®, but also for his continuous encouragements, his kind

words, his availability and his invaluable expertise. Thank you so much Marc. I would like to extend my gratitude to the other members of the mechanical workshop, especially Romain and Stephan.

My dear Sabrina Oismayo, despite the distance and your busy schedules you've never forgotten me. Your frequent kind messages were very helpful and cheered me up more than once. You're more than a friend, you're a sister.

I also thank my sensei René Amstutz for teaching martial arts in such an informal and funny (though efficient) way that I was always willing to come for training. I also thank all the members of the club, especially Jean Jacque for your sense of humor, Anne Laure for your advice and kindness, and Shawnee for being my favourite opponent and uke!

Now, to the people who inspired me and motivated me to come this far: my family of course! To my father, thank you for your support, for trusting me all these years, and letting me travel so freely for my studies. To my mother, thank you for giving me more love and support than anyone could ask for. Thank you for raising me the way you did, for all the countless times you've been there for me, and for being such a wonderful and exemplary human being. I am truly blessed to have you as a mother. To my sister Yasmine, for your patience, your kindness, sometimes for our shared craziness, and often for your healing voice on the phone, thank you. To my uncle Abbas, for your continuous love and support, thank you.

Last but not least, I warmly thank my dear husband Nicolas Chobaut, I love you with a special love that deepens every day. Thank you for sharing your life with me.

Abstract

The use of fibre reinforced composites has significantly increased in the last decades. Almost every designed structure requires connections between component members, and for composite structures, the main methods of assembly are bolting and adhesive bonding. The second one has a high potential, since the stress distribution is more uniform compared to mechanical fasteners. However, crack propagation in this type of material requires studies on a case by case basis to determine if the structure can tolerate the damage of if a repair is necessary.

Several toughening mechanisms, such as fibre bridging, can occur during delamination of fibre reinforced composites. In structures made of composite substrates, delamination can occur either in the composite or in the adhesive layer. In the first case composite toughness might be affected by the presence of the adhesive, especially if the crack propagates nearby the bond layer. The interaction of an adhesive layer with the propagation of sub-surface delamination cracks within the adherent remains a mechanism which is not well understood.

In this work, the mode I delamination behavior of Asymmetric Double Cantilever Beam bonded joint specimens is investigated and compared with bulk composite specimens in order to assess the influence of an adhesive layer. Fracture resistance measurements show that the bond layer considerably affects the steady state fracture toughness of the composite with a significant reduction of the bridging contribution. This effect is extended to two different types of epoxy adhesive: different curing cycles and different elasto-plastic properties. The extent of mode II due to the asymmetric position of the crack starter and to the adhesive layer is assessed both experimentally and numerically, and found negligible for the considered configurations. Besides, it is demonstrated that the change of compliance of a specimen due to the presence of an adhesive layer has almost no effect on the delamination behavior.

Using an inverse identification methodology, the parameters describing the bridging traction relation are determined for both joint and bulk specimens. It is found that the rate of decay of bridging tractions is significantly higher for joints compared to bulk specimens. Those identified tractions-separation relations are subsequently implemented in cohesive zone models to simulate delamination of each configuration. Load displacement and crack growth are successfully predicted, demonstrating that this method, which consists in identifying a cohesive model for a specific crack position offset in the presence of an adhesive layer, can be used for prediction purposes. Moreover, it is shown that the identified tractions based on the steady state strain measurements predict the strains at the transient phase of bridging development.

The isolated fibres and bundles of fibres participating to bridging are quantitatively measured in both bulk and joint specimens, and results show that mostly isolated fibres participate to bridging in the case of joints, whereas they tend to congregate to form clusters in bulk specimens, which require much more energy to break.

A 3D finite element model show that the elasto-plastic properties of the adhesive create a local perturbation of the stress field around the crack tip. A shielding effect of the adhesive layer has been ascertained, preventing stresses from spreading continuously. The changes of amplitude and the

spatial repartition of stresses in the process zone compared to bulk specimens with the same geometry are highlighted.

Processing induced microstructure features that influence the development of bridging are investigated with microscopic observations of transverse sections and fractured surfaces of the tested specimens. A clear link is established between extent of bridging and roughness of the crack surface: more homogeneous fibre distribution leads to a smoother crack surface and less bridging. It is found that the tortuosity of the crack is mainly controlled by the spatial fibre and matrix distribution, since the crack tends to grow in fibres-rich zones, avoiding regions with high resin content. The influence of an adhesive layer is far less critical for the development on large scale bridging than a change of microstructure.

A multiscale FE model with an embedded cell based on given microstructure and material properties is used to compare the micromechanisms at the onset of damage in joint versus bulk specimens during a mode I loading. It is found that in the presence of a joint, due to the more compliant response of the adhesive, a significantly different microcrack initiation pattern is observed compared to the bulk composite case. Moreover, a significantly more discontinuous crack propagates within the centre of the ply for the bulk composite, whereas the crack is much smoother with fewer discontinuities and it migrates towards the interfaces of the ply in the presence of an adhesive. Therefore, fracture behavior differences observed at the macroscale between bulk and joint specimens can be attributed, at least in part, to the changes of damage micromechanisms that trigger the formation of bridging fibre bundles in mode I delamination.

Résumé

Une forte croissance de l'utilisation des matériaux composites a été observée ces dernières décennies. Dans une même structure, pour assembler la plupart des composites, l'utilisation d'adhésifs prévaut pour une répartition plus uniforme des contraintes. Cependant, des fissures peuvent se propager dans ce type de matériaux, qui, étant relativement coûteux, nécessitent alors des études pour déterminer si la structure peut tolérer le dommage ou si une réparation est inévitable. Lorsque la fissure se propage dans un composite renforcé avec des fibres, plusieurs mécanismes dissipatifs peuvent se produire. L'intérêt se porte en particulier sur le pontage de fibres, qui augmente énormément la résistance du matériau, c'est pourquoi de nombreuses études portent sur la délamination des composites fibreux. Cependant, l'influence d'une couche de colle à proximité de la fissure dans le composite n'est pas documentée, et n'est dont actuellement pas prise en compte dans les tests mécaniques standards.

Dans ce travail, la délamination en mode I de laminés unidirectionnels asymétriques est étudiée, et comparée à celle de laminés asymétriques contenant un joint de colle, l'objectif étant de déterminer l'influence de l'adhésif au voisinage d'une fissure se propageant dans le composite.

Des spécimens standards sont produits et soumis à des tests quasi-statiques, montrant que le film de colle impacte considérablement la valeur plateau de la résistance à la propagation de fissure du composite étudié. Cet effet est également observé en utilisant un autre type d'adhésif, avec une épaisseur, un cycle de cuisson et des propriétés mécanique relativement différents. Plus précisément, une importante diminution de la contribution du pontage de fibre a été mis en évidence lors de la présence d'un film adhésif.

Il a été vérifié numériquement et expérimentalement que la présence de mode II due à l'asymétrie des laminés est négligeable, et n'est donc pas responsable de l'effet observé. De même, le changement de rigidité des spécimens dû à la présence d'une couche relativement souple comme un adhésif n'a presque pas d'influence sur le comportement en délamination du composite.

Une procédure d'identification inverse pour quantifier les tractions de pontage montre que la vitesse de déclin des tractions de pontages est significativement plus élevée dans le cas des joints comparés au laminé sans colle. La courbe de force versus déplacement ainsi que la propagation de la fissure sont prédites avec succès, montrant que cette méthode, qui consiste à identifier une loi cohésive pour une position de fissure donnée, et en présence d'une couche de colle, peut être utilisée à des fins prédictives. De plus, il est démontré que les tractions identifiées en se basant sur des mesures de déformation à l'état stationnaire peuvent prédire les déformations à l'état transitoire du développement du pontage de fibres.

Les fibres isolées et les faisceaux de fibres participant au pontage sont quantifiés pour le cas d'un composite fibreux et celui d'un joint collé. Les résultats montrent qu'une majorité de fibres isolées participent au pontage dans le cas des joints collés, tandis que dans le cas des laminés sans joint, les fibres se rassemblent en faisceaux, qui nécessitent bien plus d'énergie pour rompre et participent donc d'avantage à la résistance à la propagation de fissure.

Une simulation en 3D par éléments finis montre que les propriétés elasto-plastique du joint de colle créent une perturbation de l'état de contrainte aux environs de la pointe de fissure. Un effet de bouclier est mis en évidence, empêchant une répartition continue des contraintes.

Les caractéristiques microstructurales induites par les procédés de fabrication influencent le développement du pontage de fibres : un lien a été clairement établi entre l'ampleur du pontage de fibre et la rugosité de la surface fissurée du composite. En effet, une distribution homogène des fibres de carbone dans les plis du laminé conduisent à une surface fissure plus lisse, corrélée à un faible pontage de fibre, et vice versa. Il est également montré que la tortuosité du crack est principalement contrôlée par la répartition spatiale de fibres et de matrice époxy : la fissure se propage préférentiellement dans les régions riches en fibres, évitant les zones avec un taux élevé de matrice. D'ailleurs, il est observé que l'influence de la couche de colle relevée précédemment est bien moins critique pour le développement du pontage de fibres qu'un changement de microstructure.

Un model multi-échelle par éléments finis avec cellule intégrée, basée sur la microstructure d'un composite similaire, est utilisé pour comparer les micromécanismes à l'initiation du dommage dans les joints collés et dans les laminés sans colle, pour un état de déformation correspondant à un chargement en mode I. Il est montré qu'en présence du joint de colle, un motif d'initiation de microfissures très différent du cas du composite seul est observé. De plus, la fissure se propage de manière très discontinue dans le cas du composite seul, alors que le chemin de fissure est moins tortueux et migre vers l'interface du pli en présence de l'adhésif. C'est pourquoi les différences de comportement en délamination observées à l'échelle macroscopique entre composite et joints collés, peut être attribuée, au moins en partie, aux changements de micromécanismes qui provoquent la formation de faisceaux de fibres pontant lors de la délamination en mode I.

Mots-clés: Délamination, réparations collées, composite renforcé avec des fibres, pontage de fibres, joints collés, éléments cohésifs.

Contents

Chapter 3: Mode I delamination of DCB2-P1-B bulk specimens

Chapter 4: Experimental Results

Chapter 5: FE Modeling

Chapter 6: Mechanistic investigations at the microscopic scale

Conclusions and Perspectives

References

Appendix I

Appendix II

Curriculum Vitæ

List of figures

XIV

XV

XVII

List of Tables

ACRONYMS AND ABBREVIATIONS

2D	Two dimensional
3D	Three dimensional
ADCB	Asymmetric Double Cantilever Beam
ASTM	American Society for Testing and Materials
A1	Adhesive Resoltech 3350-3358T
A2	Adhesive Gurit SA80
B	Bulk
BK	Benzaggagh-Kenane
CCD	Charge Coupled Device
CCM	Compliance Calibration Method
CFRP	Carbon Fibre Reinforced Polymers
CLT	Classical Laminates Theory
COD	Crack Opening Displacement
CZM	Cohesive Zone Model
DCB	Double Cantilever Beam
DIC	Digital Image Correlation
DSC	Differential Scanning Calorimetry
ELSJ	End Loaded Shear Joint
ENF	End Notched Flexure
ERR	Energy Release Rate
FBG	Fibre Bragg grating
FE	Finite Element
GFRP	Glass Fibre Reinforced Polymers
ILSS	InterLaminar Shear Strength
MCCM	Modified version of the Compliance Calibration Method
MMB	Mixed Mode Bending
OLCR	Optical Low-Coherence Reflectometry
4PB	4-Points Bending
P1, P2	Prepreg 1, Prepreg 2
PTFE	PolyTetraFluoroEthylene
RVE	Representative Volume Element
SDEG	Stiffness DEGradation of the matrix
SE70	epoxy prepreg system with low energy cure cycles (70°C)
SEM	Scanning Electron Microscope
SLS	Single Lap Shear
TDCB	Tapered Double Cantilever Beam
UD	Unidirectional
VCCT	Virtual Crack Closure technique

LATIN CHARACTERS

a	mm	crack length
b, B	mm	specimens' width
$\boldsymbol{C}$	mm.N^{-1}	compliance
D	-	damage
E_1	MPa	longitudinal Young's modulus
E_2, E_3	MPa	transverse Young's moduli
E_{11}^{f}	MPa	effective flexural modulus
G_{12}, G_{13}, G_{23}	MPa	shear moduli
F^{sbs}	MPa	short beam strength
G	J.m^{-2}	Energy Release Rate
G_c	J.m^{-2}	fracture toughness
G_I, G_{II}, G_{III}	J.m^{-2}	Energy Release Rate in mode I, II and III
$G_{I,i}$	J.m^{-2}	Energy Release Rate at initiation
$G_{I,C}$	J.m^{-2}	fracture toughness at initiation in mode I
$G_{I,b}$	J.m^{-2}	contribution of bridging to fracture resistance in mode I
G_{ss}	J.m^{-2}	Energy Release Rate at steady state
G_{total}	J.m^{-2}	total Energy Release Rate
h	mm	specimen thickness
H	-	Parameter of the MCCM
I_i	m^4	quadratic momentum of beam i
J	N.m^{-1}	J-integral
J_{tip}	N.m^{-1}	contour integral extracted around the crack tip
Q		parameter of the CCM
K		degraded penalty stiffness
K_p	MPa.mm^{-1}	initial cohesive penalty stiffness
K_{nn}, K_{ss}, K_{tt}	MPa.mm^{-1}	interface stiffness properties
M		parameter of the MCCM
n	(-)	slope of log (δ_i/P_i) versus log (a_i)
n_e	(-)	refractive index
n		parameter of the CCM
p	(-)	spline smoothing parameter
p_e		Pockel's photo elastic coefficient
P	N	Load
P_m	N	Maximum observed load
R		Correlation function
R^2	(-)	coefficient of determination (statistics)
r	mm	distance from crack tip
T_g	°C	glass transition temperature

t	s	time
$\underline{u,v}$	mm	displacements
U	J	strain energy
W_s	J	work to create new crack surfaces during propagation
z_{max}	mm	maximum bridging length

GREEK CHARACTERS

γ	-	decay rate of the tractions along bridging zone
δ_b	mm	crack opening displacements associated to bridging
δ_c	mm	critical crack opening displacements
δ_i	mm	vertical displacement of one beam
δ_{max}	mm	maximal crack opening displacements
δ	mm	crack opening displacements
Δa	mm	crack increment
$\Delta\lambda_B$	nm	Bragg wavelength variation
ε_z	-	dominant elastic strain component
ε_{FBG}	-	axial strain profile measured by FBG
ε_{FEM}	-	axial strain profile simulated by FE method
η	-	fitting parameter of BK mixed mode fracture criterion
θ	degree	relative angle between the arms of the DCB specimen
λ_{B0}	nm	Bragg wavelength
Λ		grating spacing
$\nu_{12},\ \nu_{13},\ \nu_{23}$	-	Poisson's ratio
ξ	°C^{-1}	thermo-optic constant
Π	J	potential energy of the system
σ_b	MPa	parametric surface traction to represent the bridging zone
σ_c	MPa	critical stress level
σ_{max}	MPa	maximum tractions at the crack tip
$\hat{\sigma}_b(\delta)$	MPa	identified bridging law / cohesive traction-separation law
χ	mm	parameter accounting for uncertainty on crack tip position
ψ	J	total energy of the body
ω	(-)	weight of initial fracture toughness in the optimization

NOTATION

$\left.\dfrac{\partial\Pi}{\partial a}\right|_{\Delta}$	partial derivative of Π with respect to a for constant Δ
$a;b$	concatenation of 1D vectors a and b
$\lVert a\rVert^2$	norm of vector a

Introduction

Motivation

Almost every structure requires connections between component members, and for composite structures, the main methods of assembly are bolting and adhesive bonding. The second one has a high potential, and its use in the aircraft industry has seen a large increase in recent years. Indeed, the use of adhesively-bonded joints instead of the traditional types of joining such as welding or mechanical fasteners, leads to a reduction in weight and allows complex shapes. It also improves the aerodynamic of aircrafts, since the surface is smoother than it would be with the use of rivets and bolts. Moreover, the advantage of bonding is that no stress concentrations are introduced around rivet holes, thus the stress distribution is far more uniform in the surroundings of adhesively bonded joints as compared to mechanical fasteners.

Despite its many advantages this technique is not extensively applied in this domain because of the lack of knowledge of bonded joints behavior concerning their durability and fracture toughness, and the difficulty to inspect the adhesive layer quality following manufacture and in-service life. Thus various methods have been developed to improve material selection, surface and adhesive quality, and stress analysis [1]. In current repair strategies, bonded composite patching is used to restore the strength of aerospace, naval and civil structures after non-catastrophic damage because the cost of component replacement is much higher. Composite patch repair can increase the service life of advanced structures with a better efficiency than standard fastened metallic patches since they are less damaging to the parent structure. This technology is highly efficient and has been widely investigated but is not yet fully understood and some issues are still not settled [2]. To evaluate the behavior of adhesively-bonded joints once a crack has initiated, three different ways of failure are defined (see Figure 1.1):
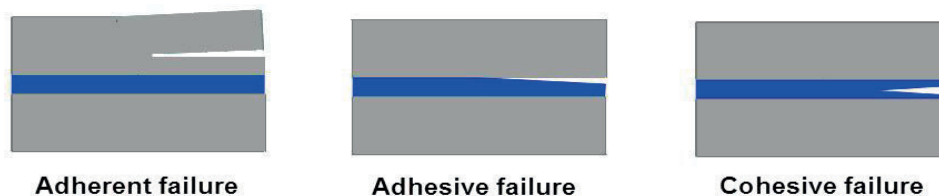
Figure 1.1: Failure modes of bonded joints

<u>Case 1: Adherent failure</u> (or interlaminar failure)
An interlaminar failure occurs when the substrate suffers delamination, i.e. crack propagation between two consecutive plies, leaving the adhesive bondline intact. This failure indicates that the adhesive strength is higher than the interlaminar strength of the composite. This is the case of interest in this work.

<u>Case 2: Adhesive failure</u>
When an adhesively-bonded joint fails at the interface, the surface of one adherent is clean of adhesive while the other is covered with adhesive. This type of failure occurs when the surface treatment prior to bonding is improper.

Case 3: Cohesive failure
This type of failure happens if a crack propagates within the adhesive layer. In this case of failure the surfaces of both adherents are covered by adhesive.

Thus a trustworthy prediction of the strength of adhesively bonded composites requires reliable material data of both adhesives and joining partners. This explains the extensive effort of researchers to develop dependable testing methods in order to obtain the constitutive behavior of adhesive layers [3-4]. However, the interaction of an adhesive layer with the propagation of sub-surface delamination cracks within the adherent (case 1) remains a mechanism which is not well understood. Experimental works reported in the literature demonstrate that several toughening mechanisms can occur during delamination of fibre reinforced composites. Fibre bridging for instance occurs when intact fibres link both surfaces of a propagating crack, hence exerting closing pressure to the crack faces. Such a toughening phenomenon has a substantial impact on the fracture behavior of a composite; hence any interference of the adhesive layer with fibre bridging might have important repercussions on the delamination behavior.

Objectives

Given the potential cost savings if composite bonded joints and composite patch repairs were more used in the aircraft industry, several questions need to be addressed: in the case of adherent failure, does the adhesive layer interfere with the normal delamination / fiber bridging fracture of the composite? Which parameters control those potential interactions? Does it depend on the position of the crack, on the adhesive type, or on the composite microstructure? How to model such phenomena and what are the mechanisms causing it?

Because of the lack of deep understanding of the influence of an adhesive layer on delamination, this work has the following objectives:

> ➢ Characterization and understanding of interlaminar delamination of both asymmetric FRP bonded joints and asymmetric FRP bulk laminates under monotonic mode I loading.
> ➢ Evaluation of the influence of initial defect position on the extent of mode mixity and on delamination behavior of asymmetric unidirectional CFRP bonded joints.
> ➢ Determination of the influence of the adhesive layer on interlaminar delamination behavior of asymmetric unidirectional CFRP bonded joints for different types of adhesive.
> ➢ Identification of bridging tractions distribution in mode I delamination of adhesively bonded unidirectional laminates and cohesive modelling of the fracture processes observed experimentally.
> ➢ Evaluation of the microstructural features and damage mechanisms influencing the development of fibre bridging.

Structure of the thesis

This thesis is divided into 7 chapters as follows:

Chapter 1 gives a short review of the available literature in the domains of delamination of fibre reinforced composites, fibre bridging, adhesively bonded joints and composite patch repairs.

Chapter 2 provides a description of materials and manufacturing process employed to fabricate the specimens. The method of strain monitoring using optical fibres, and the inverse identification method are also detailed. All the testing methods obtained from standardized protocols that are used to perform the experimental work are outlined. Furthermore, the different Finite Element (FE) modelling methods are described.

In **Chapter 3**, the delamination behavior of asymmetric unidirectional laminates made of bulk composite is experimentally characterized. The bridging parameters and the traction-separation relation is identified and then compared with the scaling function available in the literature. Additionally, strain measurements using optical sensors positioned at the steady state region are employed in an inverse identification method to numerically predict the loading response and crack growth at intermediate propagation states.

Chapter 4 addresses the experimental results involving adhesively bonded joints. Two types of adhesives are investigated. The potential presence of shear during the mode I delamination is assessed. A quantification of the fibres and bundles of fibres involved in the bridging phenomenon is presented, as well as a study on the roughness of the crack profile.

Chapter 5 is dedicated to the different methods of FE analysis at the macroscale used to understand and characterize the mechanical behavior of the investigated specimens.

Chapter 6 provides a study on the microstructural features and micromechanisms that affect the delamination behavior of the composite.

Finally, **chapter 7** presents the conclusions and some suggestions for possible future works.

Chapter 1: State of the art

1.1 Patch repair

Among the different repair methods of advanced structures, the adhesively bonded composite patch is one of the most efficient, and has been widely investigated. Since its introduction by Bakker [5,6] many experimental and numerical studies have been reported [7,8]. There is now a clear understanding of the importance to design an optimal patch shape (rectangular, circular, trapezoidal, etc.) to maximize the safety-cost ratio [9-11].

A closer look at a typical laminate repair (see Figure 1.2) reveals that damage can initiate either in the adhesive or in the composite between the plies. The effect of adhesive disband on the performance of the repair was investigated by many researchers [2, 13-15] whereas a crack initiating and propagating in the bulk of the composite part is considered to depend only on the composite properties.
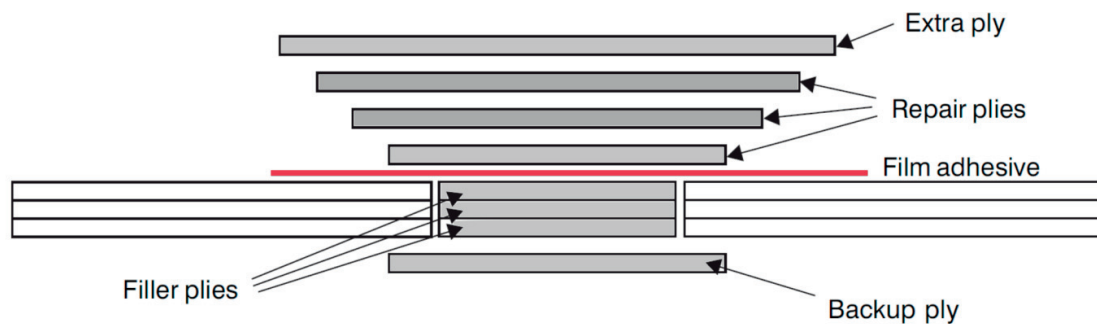
Figure 1.2: Typical laminate patch repair (adapted from [12]).

1.2 Delamination

Delamination is a frequent mode of failure in composites laminates. Delamination can originate from many sources, among which manufacturing imperfections, fatigue loading, low velocity impact, stress concentration near geometrical discontinuity, or even from high interlaminar stresses [16]. This explains the large amount of available papers and literature reviews on that matter. A good summary of the current knowledge can be found in [17].

1.3 Fibre bridging

Experimental works reported in the literature demonstrate that several toughening mechanisms can occur during delamination of FRP composites bonded joints and composite laminates as shown in Figure 1.3. Among these mechanisms, fibre bridging is considered very important. Fibre bridging occurs when a crack jumps from one fibre/matrix interface to another without breaking the fibre. Experiments show that if the apparent fracture toughness is plotted as a function of crack extension, an increase is observed, and this is usually described by the concept of resistance curves (R-curves).

In laminated composites, it is shown that this increase is mainly due to the fibre bridging behind the crack tip [18].
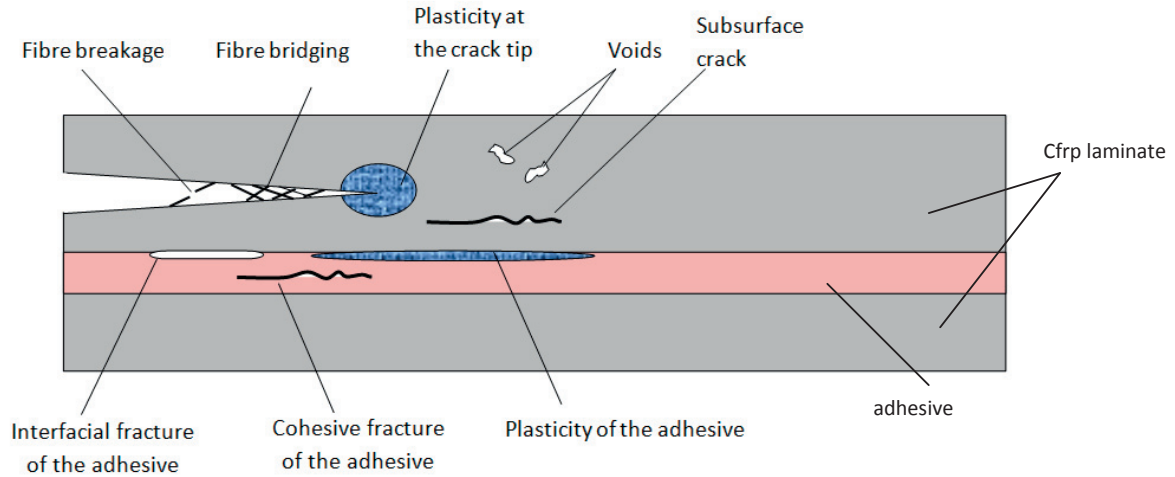
Figure 1.3: Possible damage mechanisms in an Asymmetric CFRP bonded joint
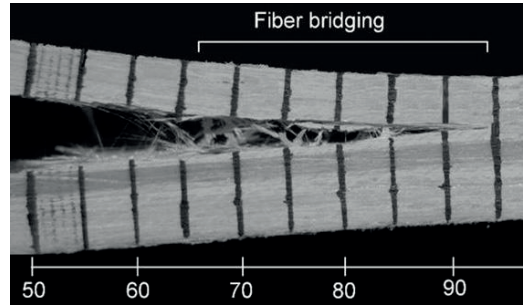
Figure 1.4: Fibre Bridging observed during crack propagation in an Asymmetric DCB specimen [32].

The contribution of fibre bridging to the fracture toughness is hard to quantify and a large effort is observed in the literature to model this phenomenon. One method consists in measuring the crack opening displacement (COD) and deriving the Energy Release Rate (ERR) with respect to COD [53] to obtain the bridging law but this approach requires accurate measure of the maximum crack opening. Another way is to idealize the bridging law and then fit the computed R-curves to measured R-curves to obtain an approximate bridging law [20]. Stutz *et al*. [18] proposed a semi-experimental method to accurately evaluate the bridging tractions in delamination of FRP laminates using embedded multiplexed Fibre Bragg grating (FBG) strain sensors and parametric Finite Element (FE) modelling. This method consists in an inverse numerical identification scheme that matches the strain distribution obtained from the FGB's with those simulated by the FE model, in order to calculate the involved bridging tractions. Recently, Farman-Ashtiani *et al*. demonstrated the specimen thickness dependence of monotonic mode I delamination in unidirectional carbon epoxy laminates: the amount of fibre bridging increases with specimen's thickness due to the change of the specimen arm curvature [21]. Thus, the identified cohesive traction-separation relations representing delamination and fibre bridging cannot be considered as a material property and are at least dependent on the bending stiffness of the adherent.

1.4 Fracture mechanics approach

To investigate fracture in different materials, concepts of fracture mechanics are used. Three modes of failure can be defined (Figure 1.5): mode I, or opening, mode II or sliding shearing, and mode III or tearing. Besides these three basic modes there exist mixed mode loading cases, the most important being the mixed-mode I / II.

| Mode I (opening) | Mode II (Sliding Shear) | Mode III (tearing) |
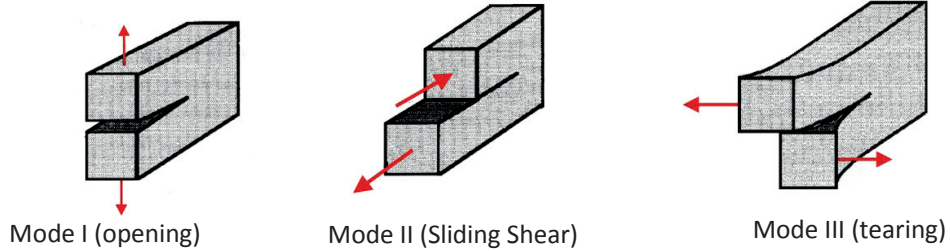
Figure 1.5: Modes of failure

Using concepts of fracture mechanics, the fracture is usually expressed by the ERR which corresponds to the energy dissipated during fracture per unit of new created surfaces [22]. The ERR failure criterion, first established by Irwin in 1957 [23] states that a crack will grow when the available ERR is greater than or equal to a critical value G_c, referred to as fracture toughness. All the different possible types of loading result in different stress fields at the crack tip and therefore different fracture toughnesses as shown in Figure 1.6.
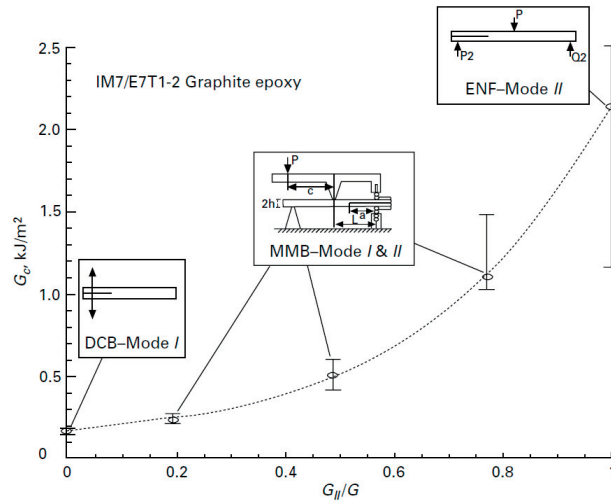
Figure 1.6: Typical mixed mode I and II delamination criterion (6)

Finite Element (FE) analysis is a powerful tool for predicting the fracture behavior of laminated composites and bonded joints. Extensive work on that matter is available [4]. Modelling the effects of the asymmetry and fibre bridging on the fracture behavior and determination of their influence on ERR calculations are necessary to accurately describe the fracture behavior of asymmetric adhesively-bonded joints. Among the available methods, the Virtual Crack Closure Technique (VCCT)

[24-26] is of interest as it allows determining the mode I and II ERR components G_I, G_{II}, respectively, while the FE-based J-integral calculation can provide accurate estimates of the total ERR.

1.5 Standardized testing methods

Figure 1.6 shows existing tests configuration for each type of loading: DCB for mode I, ENF for mode II and MMB for mixed mode I and II. Standards already exist for mode I (ASTM D 5528 – 01 [27]) and mixed mode (ASTM D 6671/D 6671M [28]) but the pure mode II remains controversial [29]. Moreover, it is demonstrated that for composite bonded joints, the thickness of the adhesive layer modifies the measured value of the ERR (for fracture in the bondline) as shown in Figure 1.7 for both mode I and mode II testing [1,24].
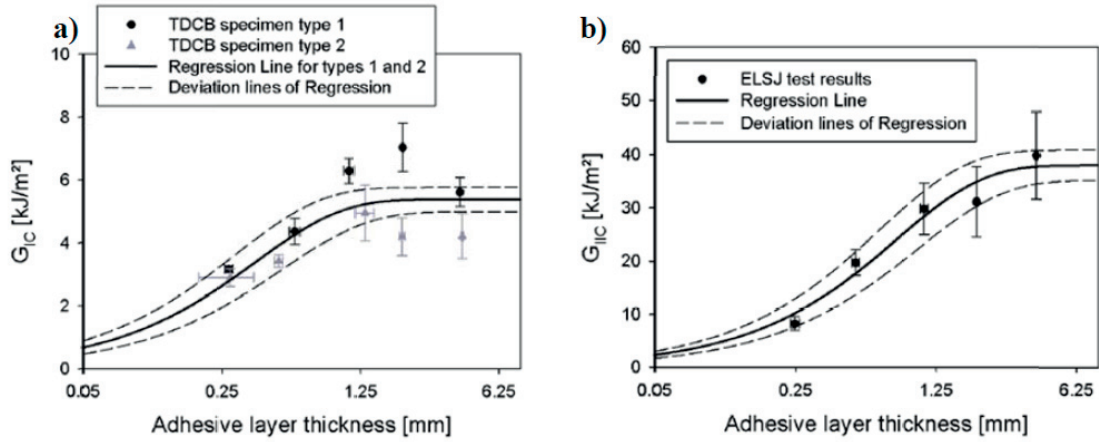
Figure 1.7: Maximum fracture energy versus bondline thickness for a) mode I tapered Double Cantilever Beam (TDCB) test, and for b) mode II end-loaded shear joint (ELSJ) test [24].

Laminated composites and composite bonded joints are rarely subjected to pure mode loading during in-service life. Consequently, the fracture behavior of those materials must be investigated under mixed-mode I/II loading.

Mixed mode testing and analysis

Several testing methods are proposed in the literature to characterize the delamination on a laminated composite subjected to both shear and tensile loading [33,34]. The most widely used configuration is the MMB (Mixed Mode Bending) method [28]. Though Mòllon et al. [35] showed that the Asymmetric Double Cantilever Beam (ADCB) test is an interesting alternative test method to the MMB test to produce a mixed mode loading at the crack tip. Indeed, ADCB joints tested in Mode I, the crack propagates in the adherent away from the symmetry plane constituted by the bondline thus a mixed mode loading can be created. It can be accompanied by considerable fibre bridging [30-32] as shown in Figure 1.4.

Based on that, different data reduction methods are proposed to calculate the different ERR components. Actually, there is still a challenge to find an accurate way to quantify the resulting ratios of mode I and of mode II in such a test. Analytical approaches can be found in the literature, such as the "global approach", proposed by Williams [36], based on the beam theory, or the "local approach"

proposed by Hutchinson [37] based on the calculation of the stress intensity factor near the crack tip. It is worth noticing that the ''global approach'' results in pure mode I for any ADCB specimens, which means that the component of mode II is negligible. This result is experimentally and numerically confirmed by Shahverdi et al. [30] who investigated the effect of the geometrical asymmetry on pultruded GFRP DCB joints, and a negligible mode II component (less than 1% of G_I) is found. Also, Zhang et al. [31] studied the fracture behavior of pultruded asymmetric joints with different standards procedures [38-39] and showed that the induced mode II fracture component is less than 1% of mode I for specimens tested under mode I, and that the induced mode I component is limited to 1% of the mode II component for End Loaded Split specimens. According to this study, the asymmetry of this type of specimen does not affect the results and Zhang showed thereby that the use of above mentioned existing standard methods is valid for asymmetric specimens.

1.6 Micromechanics

Composites laminates can be considered on different scales for analysis. At the microscopic scale, the local states of deformation and stress of the constituents (matrix and reinforcing fibres) and their interactions are relatively complex but their knowledge is essential since they heavily impact the macroscopic properties (such as the yield strength, the onset of damage [40], etc.). The behavior of each lamina is a non trivial function of the constituent properties and geometric characteristics, such as fibre volume fraction and fibre packing geometry [41]. It is demonstrated that a simple relation involving the phase volume fractions such as rule of mixtures is not sufficient to describe some effective properties of a heterogeneous material such as the conductivity [44] or strength.

The spatial distribution of the phases (shape, nesting of fibres, connectivity, etc) is a key feature to predict a laminates' constitutive behavior. Torquato [44] developed a *systematic theory* to relate quantitatively the changes in microstructures of general random heterogeneous materials to changes in the macroscopic properties. Moreover, several numerical approaches have been developed (Finite differences, FE modelling, periodic cell, etc.) and bring good predictions but their computational time is too high for use in design.
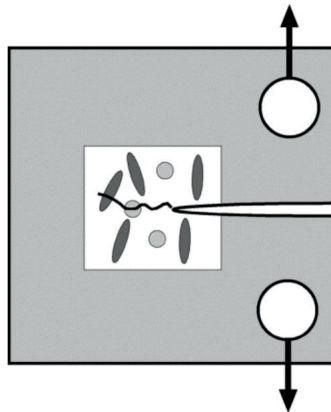
Figure 1.8: Schematic of an embedded cell simulation of fracture. The details of the composite microstructure (matrix, reinforcements and interfaces) are included in front of the notch tip, while the remaining material is represented as a homogeneous anisotropic material [48].

Great progress has been achieved in the last years in terms of performance/cost ratio by employing multiscale modelling strategies: a representative volume element of the material microstructure is simulated in the fracture region as an embedded cell (see Figure 1.8), taking into account the spatial distribution of matrix and fibres, but also the relevant micro-damage and fracture processes (epoxy matrix hardening, fibre/matrix decohesion, damage evolution, etc), while the remaining material is simulated as a homogeneous solid whose properties are obtained from a suitable homogenization model. This approach has proven to successfully predict the fracture behavior of heterogeneous materials for some types of mechanical tests (3 Point Bending of a notched beam [46,48], DCB test [43]). In addition to their prediction capability, micromechanics finite element models can be highly valuable to give insight on the dominant factors affecting the performance of composites and highlight the sequence of damage mechanisms leading to their final failure.

Chapter 2: Materials and methods

This chapter presents the manufacturing procedures of the different specimens used in this work, and also the details of the mechanical testing, data reduction methods and optical techniques for strain measurements. Finally the employed numerical analysis methods are described. Note that details about specimen's specifications and numerical models are provided in the respective chapters.

2.1 Choice of the materials

Prepreg system

In order to follow the framework of the laboratory, and therefore benefit from the available literature and knowledge of the considered composite [21,42,50], the epoxy prepreg system SE70 produced by Gurit® is chosen for this work. This material, with a resin content of 37% and a consolidated ply thickness of 0.2mm, is employed in the construction of large components using low energy cure cycles (70°C). A curing temperature of 82°C is chosen for all the specimens manufactured in this study (see Figure 2.9).
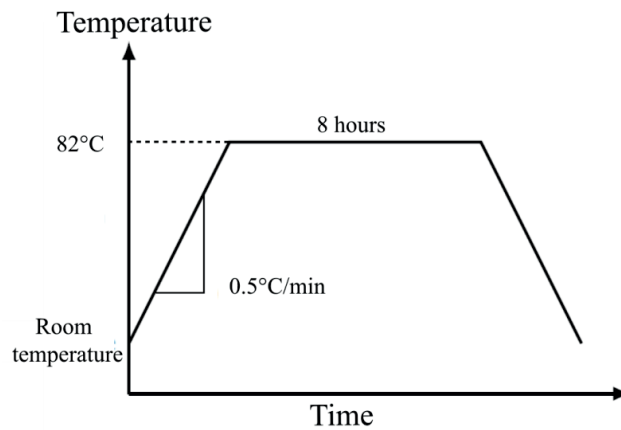
Figure 2.9: Curing cycle of the composite SE70.

The elastic properties of the obtained unidirectional composite are determined as follows:

- The longitudinal modulus E_1 (most dominant elastic constant for DCB tests) is measured with 4-points bending tests (ASTMD7264/D7264M-07).
- The strength and transverse moduli $E_2=E_3$ are determined with tensile tests (ASTM D3039/D3039M-08).
- The shear moduli $G_{12} =G_{13}$ are measured with a tensile test of the $\pm 45°$ composite (ASTM D3518/D3518M-13).

A summary of the obtained elastic constants used for subsequent numerical simulations is provided in table Table 2.1.

E_1 [GPa]	E_2 [GPa]	E_3[GPa]	ν_{12}[-]	ν_{13}[-]	ν_{23}[-]	G_{12}[GPa]	G_{13}[GPa]	G_{23}[GPa]
120	7.2	7.2	0.3	0.3	0.45	3.9	3.9	3.1

Table 2.1: SE70 Elastic constants used for simulations

Adhesive systems

In advanced structures, toughened adhesives are required to provide a high toughness in the long term (same service life as the substrates). In this work, a bi-component adhesive 3350-3358T produced by Resoltech® is used to assess the effect of a bond layer on the interlaminar properties of the composite. This toughened epoxy is designed for high-performance lightweight bonding of composites in naval structures. It consists of a resin (3350) and a hardener (3358T) that are mixed together to form a paste adhesive which has a gel time of about 30 minutes, and a viscosity low enough to obtain very thin layers (100μm).

In order to extend the investigation to another adhesive used in similar applications but with a very different thickness (400 μm) and elasto-plastic properties, the thin film adhesive SA80 manufactured by Gurit® is chosen. It contains a single glass carrier 25 g/m2 plain woven fabric with 22 fibres/cm in both warp and weft directions. By considering those two particular adhesives, that represent the two classes of products employed in advanced composite structures, the studied effect of the adhesive layer on the delamination behavior of the composite covers a wide range of possible toughened adhesives typically used for such applications.

2.2 Nomenclature
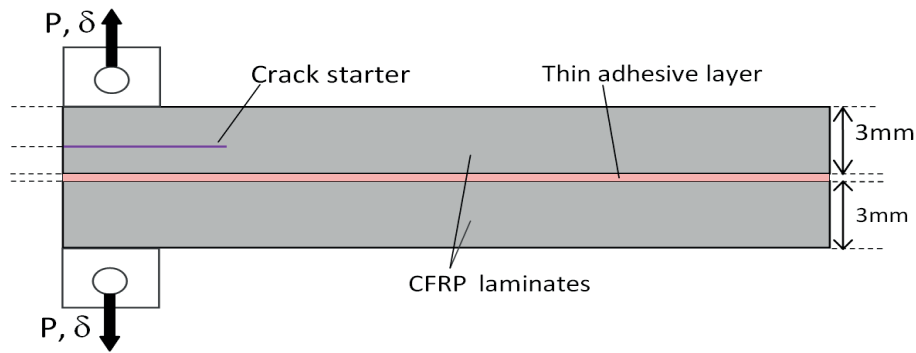
Figure 2.10: Schematic of Asymmetric DCB bonded joint specimen

The delamination behavior of adhesively bonded joints and of bulk ADCB specimens are investigated in this work. In this configuration, the crack propagates in the composite along paths outside the symmetry plane, depending on the position of the initial crack starter. Knowing that 2 different prepreg systems, 2 types of adhesives and 2 positions of the initial crack are employed in this study, the following nomenclature is introduced:
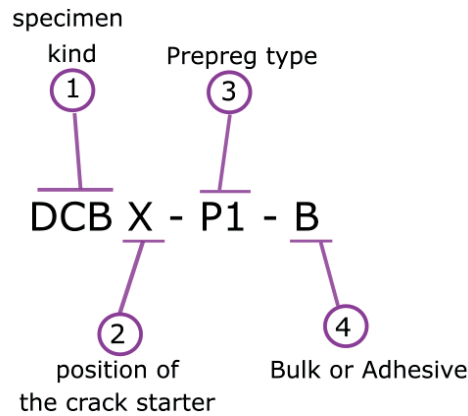
Figure 2.11: Adopted nomenclature

1. First the kind of test is specified (DCB).
2. Then the depth of the crack starter is written in number of plies from the midplane: for instance X=1 when the Teflon insert is positioned 1 ply from the midplane; X=2 for two plies from the midplane, etc.
3. The third specification is the prepreg type. A first version of the prepreg system SE70 produced by Gurit® is denominated by P1, and a second version of this same reference (exhibiting a different microstructure) is designated by P2.
4. Finally the 4th and last term informs if the specimen is made of bulk composite (B), or contains a bond layer of the adhesive paste Resoltech 3350-3358T (A1), or a bond layer of the adhesive plastic film SA80 (A2).

For example DCB2-P1-A1 designates a DCB specimen manufactured with the original prepreg, bonded with the glue Resoltech 3350-3358T according to the procedure described in section 3.2.1, with the initial defect 2 plies from the bond layer.

Note that all the composite parts used in this work are unidirectional (UD) laminates.
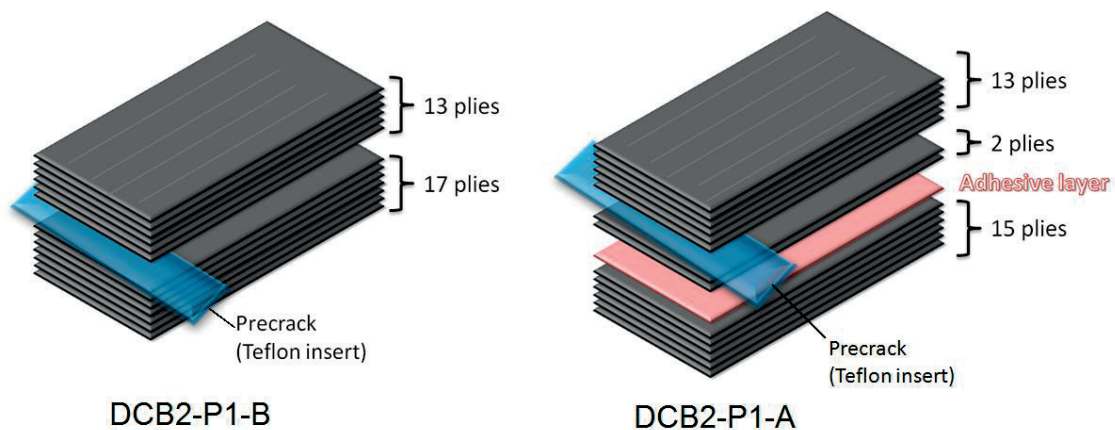
Figure 2.12: Schematic representation of the manufactured asymmetric DCB specimens and the corresponding nomenclature.

2.3 Specimen preparation

2.3.1 Jig to control the adhesive layer thickness

Since the thickness of the adhesive layer is of prime importance [24], a special jig is designed to ensure a constant bondline thickness along the specimens' length (see Figure 2.13). The jig allows to insert machined spacers with the desired thickness to control the minimum gap, while a vacuum bag compresses the joint down to that controlled thickness with a tolerance of 30 μm.

2.3.2 DCB specimens with A1 adhesive system

Unidirectional composite beams are produced using 15 plies of carbon/epoxy prepreg SE70 from Gurit SP[TM], with a nominal cured ply thickness of 0.2 mm resulting in a 3 mm-thick plate. To create a 60mm asymmetric crack starter in the CFRP bonded joints specimens, a 13 μm-thick Polytetrafluoroethylene (PTFE) film (A6000 from Aerovac®) is introduced between the 13th and 14th layer (for DCB2-P1-A1) or between the 14th and the 15th layer (for DCB1-P1-A1). The plate is cured under vacuum in an autoclave at 82°C with 3 bars pressure for 8 hours, with a plate of aluminium placed on its top and precise spacers on the edges to obtain a uniform thickness.

1: lower arm of DCB joint
2: Steel mold
3: weight with chamfers to use vacuum bag
4: upper arm of DCB joint
A: tailored bondline thickness by using adequate spacer
B: excess of adhesive is removed without lowering with the joint quality
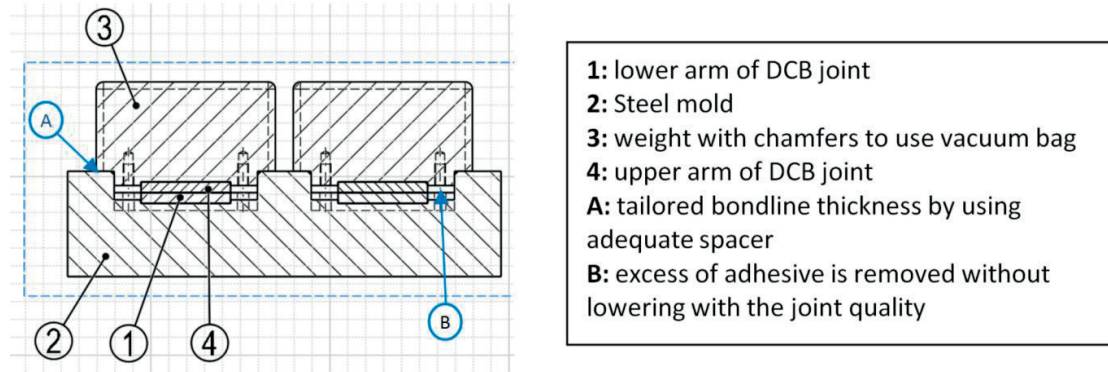
Figure 2.13: Schematic of the jig used to control bondline thickness

The following curing cycle is applied (see Figure 2.9) : a ramp heating with a rate of 0.5°C/min to 82°C, then the composite is held at 82°C during 8 hours, and then cooled down up to room temperature. The plate is then cut with a diamond saw to obtain beams with a width of 25 mm. The resulting beams are sandblasted at 4 bars, and cleaned from dust and sand with cleaning pad (from HBM®) soaked with acetone, which are designed not to leave any fibre on the surface. The bi-component epoxy adhesive Resoltech 3350-3358T is used to bond the 3mm-thick CFRP beams. First the resin is weighted with a precise balance then the hardener is added and a spatula is used to mix them together, with care to avoid the formation of bubbles, during at least 2 minutes. The spatula is used to spread the adhesive paste on the sanded surfaces of CFRP to form a relatively thin and uniform layer. The bonded joints are subsequently placed within a special jig (see Figure 2.13) designed to ensure a constant bondline thickness of 0.1 mm along the specimen length thus achieving a nominal thickness of 6.1 mm for the final ADCB joint specimen. A vacuum bag is placed over the jig before the gel time of the adhesive, which is about 30 minutes, and vacuum is held during 24 hours for a first stage of curing at room temperature (~20°C). To ensure a complete polymerization of the glue the bonded beams are kept in the jig and placed in the oven at 70°C

during 5 hours. After curing, the sides of the specimens are polished with sandpaper to remove the excess of adhesive.

The side of all specimens is painted white and marked every millimetre to help monitor the crack tip during crack propagation. Steel loading blocks (5x5x25 mm) are glued with an Araldite Rapid epoxy adhesive on the pre-cracked part to obtain ADCB-Joint specimens with the following dimensions: 220x25x6.1 mm.

2.3.3 DCB specimens with A2 adhesive

Asymmetric CFRP bonded joints are also fabricated with another adhesive system: SA80, a toughened thin film adhesive supported with a glass carrier, produced by Gurit SP^{TM}. Following the same procedure as in section 3.2.1, 25mm-wide CFPR beams are manufactured, sanded, and cleaned with acetone. Strips are cut with a knife in the adhesive film SA80 using a spare piece of substrate as a template to make them slightly wider than the CFRP beams to bond. The adhesive-strips are then carefully placed on the sanded and cleaned surface of the to-be-bonded CFRP, using cold spray to remove the protective sheet from the adhesive layer. The other part of CFRP is immediately placed on the top, and the bonded composite is put in the special jig that ensures a constant bondline. No spacer is added in the jig to control the minimum gap, though the obtained thickness of the cured adhesive is satisfactorily reproducible (400μm ±50μm). Following the directions of the manufacturer, the bonded specimens are cured at 80°C during 14hours. After curing, the sides of the specimens are polished to remove the excess of adhesive.

2.3.4 Asymmetric DCB Bulk composite laminates

To compare the delamination behavior of bonded joints versus bulk composite, 6mm-thick ADCB specimens – i.e. without adhesive layer – are fabricated by stacking 30 plies of the same prepreg and following the same curing procedure. The Teflon insert is placed during stacking at the adequate position to create the desired asymmetry.

2.4 Optical measurements using FBG sensors

Optical FBG sensors are used in this work to measure the strain field in selected regions of a DCB2-Bulk specimen submitted to mode I delamination. The obtained strain data are used as an input in an inverse method described in section 2.10.3.

2.4.1 Fibre Braggs Grating sensors

In this section the main principles of optical fibres and Fibre Bragg Grating (FBG) sensors are described. An FBG sensor consists of a short segment of optical fibre that reflects particular wavelengths of light and transmits all others, due to a periodic variation in the refractive index created in a specific length of the fibre core (see Figure 2.14). Thus if a broad band light source is coupled into the optical fibre, the sensor reflects a sharp peak at a wavelength called Bragg wavelength λ_{B0} given by the equation $\lambda_{B0} = 2 n_e \Lambda$, where n_e is the refractive index and Λ the grating spacing.
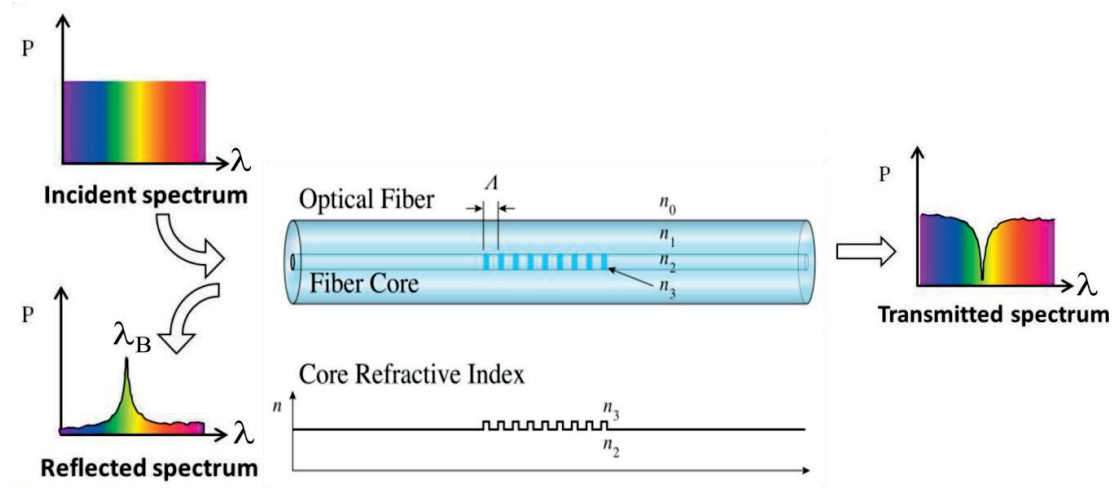
Figure 2.14: Fibre Bragg grating scheme and its wavelength spectra (adapted from [42] and [72]).

When the fibre is subjected to a load, Λ and n_e change hence the wavelength λ_B is shifted. This shift of the wavelength can be converted to a strain value using equation (2.1):

$$\frac{\Delta \lambda_B}{\lambda_{B0}} = (1 - p_e)\varepsilon_z + (\alpha_f + \xi)\Delta T \qquad \textbf{(2.1)}$$

Here $\Delta \lambda_B$ is the Bragg wavelength variation during loading, p_e is the Pockel's photo elastic coefficient that takes into account Poison's effect, with a value of 0.2148 determined experimentally; ε_z is the dominant strain component; α_f is the thermal expansion coefficient; ξ is the thermo-optic constant [54] and ΔT is the variation of temperature. Since FBG's are sensitive to stress field and thermal change it is necessary to work at constant temperature to ensure that the shift is only due to the load, which leads to the following expression for converting a shift of wavelength to a measure of strain:

$$\frac{\Delta \lambda_B}{\lambda_{B0}} = (1 - p_e)\varepsilon_z \qquad \textbf{(2.2)}$$

Using multiplexing capabilities of FBG sensors, both optical fibres used in this work contains 10 short FBG's that are interrogated simultaneously during loading (see Figure 2.15), using the SM 130 from Micron Optics ® electronic device for data acquisition. Thus a discrete strain field (with 10 points) in the debonding face can be extracted and used as input in an inverse method developed in section 2.10.3 to obtain the bridging law.

Note that the length of each FBG sensor is 1mm, the sensor spacing is about 3mm (the procedure to measure the precise location of each FBG is described in section 2.4.3) and the wavelengths range between 1520 and 1570 nm.
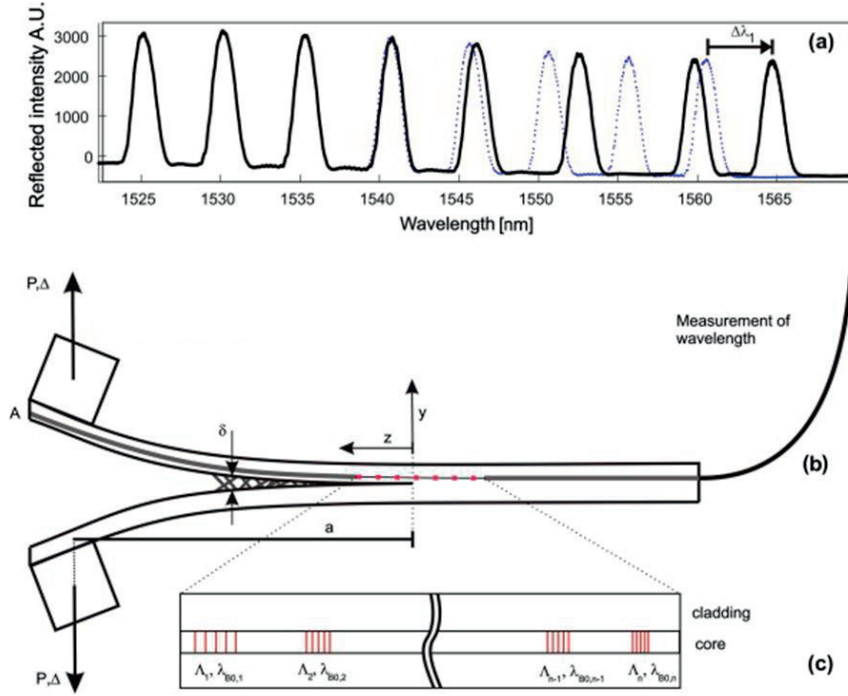
Figure 2.15: FBG's multiplexing capabilities [42]. Note that in this work, the optical fibres are positioned on the surface of the specimen. (a) A typical reflection spectrum of an FBG array before (dotted line) and when the crack tip is in the array (solid line). (b) The setup with the position of the multiplexed FBGs. (c) A schematic representation of an FBG array.

2.4.2 Integration of FBG sensors

Two optical fibres containing each 10 wavelength multiplexed FBG sensors are bonded with Loctite®401 instant glue on the upper surface of a selected specimen, parallel to the direction of the reinforcing fibres, to measure the axial strain during delamination. The choice of gluing the fibres instead of embedding them during stacking is made in order to avoid excessive handling of the specimen knowing that the glass fibres are very fragile. Also this position is far away from the neutral axis of the beam, ensuring that the strain field to measure is non-zero. The precise position of FBG sensors is shown in Figure 3.29. As shown in Figure 2.16 the polyimide coating is removed with sulphuric acid at the location of the sensors to improve the sensitivity of the gratings. To ensure a complete polymerization of the adhesive, the specimen is tested 48 hours after bonding the optical fibres.
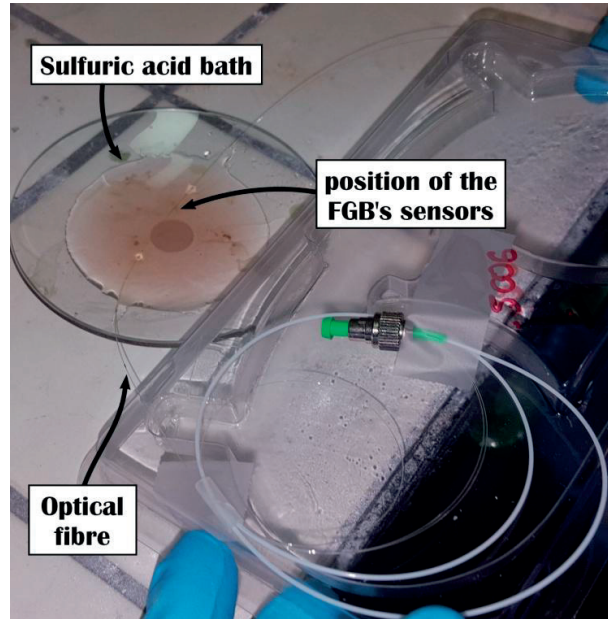
Figure 2.16: Photographs of the polyimide coating removal on the optical fibre at the location of the sensors and a few millimetres more from both ends.

2.4.3 OLCR measurements

Before the delamination test, the exact position of the FBG sensors along the longitudinal axis of the specimen containing optical fibres is determined by means of Optical Low-Coherence Reflectometry (OLCR) measurements with a HP 8504B reflectometer. This measurement is conducted in a temperature-controlled room at 23 ± 1.0 °C. A schematic of the OLCR setup is shown in Figure 2.17.
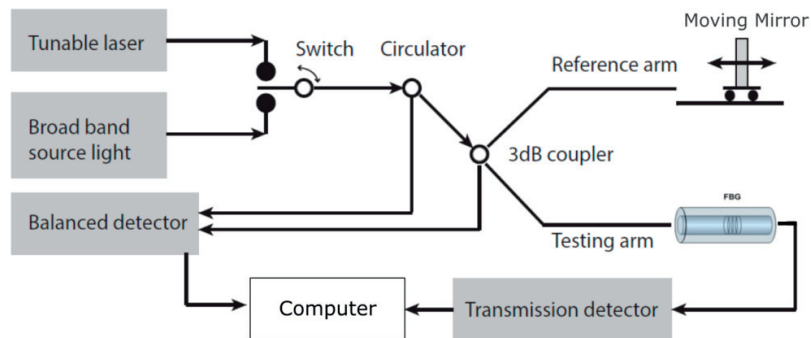
Figure 2.17: Schematic of the OLCR setup [adapted from 49].

Using a coupler, a broadband light is split into two arms. One arm consists of the specimen with the optical fibre, while a second arm that acts as a reference, consists of a mirror which can move as a function of the distance at which the optical fibre is interrogated. When the distance between a sensor and the coupler is within the coherence length of the broad band light, the reflected lights coming from the two arms produce a constructive interference in the coupler. Hence by moving the mirror with a step length of 25 µm, which is the spatial resolution of the setup, the optical fibre can

be scanned, and the relative position of each sensor can be determined with a high precision because the coherence length that gives a peak of light is unique for each FBG of the fibre. Since the end of the optical fibre also gives a reflection peak in the OLCR spectrum (see Figure 2.18), the precise position of each FBG sensor are determined relatively to this reference. Indeed the end of the optical fibre is visible on the surface of the specimen thus its position is known. Note that a sharp cut of the fibre end is needed to avoid birefringence.
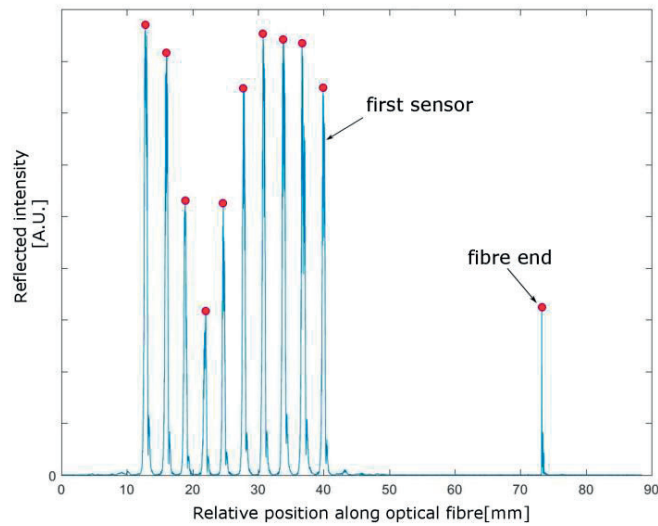
Figure 2.18: OLCR amplitude measurements

2.5 Mechanical testing

2.5.1 Delamination under Mode 1 testing

Mode I delamination tests are conducted in an Instron 5848 machine with a 2kN load cell. Data acquisition rate is set at 10Hz for all tests. The specimens are subjected to monotonic mode I loading in displacement control (1 mm/min), following the tests procedure of the ASTM standard D5528-03 [27]. A high resolution CCD camera is used to monitor the crack propagation during delamination by taking pictures at 1 Hz of the marked side of the specimens.

Note that all specimens are first subjected to precracking stage: the specimen is loaded under mode I until a drop of the load is observed coming along with a small crack increment due to the fragile resin accumulated during manufacturing at the end of the Teflon insert. Indeed the initial crack starter does not represent a sharp crack due to its geometry and to the resin rich region which forms at the end of the PTFE film during curing. This precracking step produces a natural mode I initial crack which allows capturing the true fracture toughness of the composite.
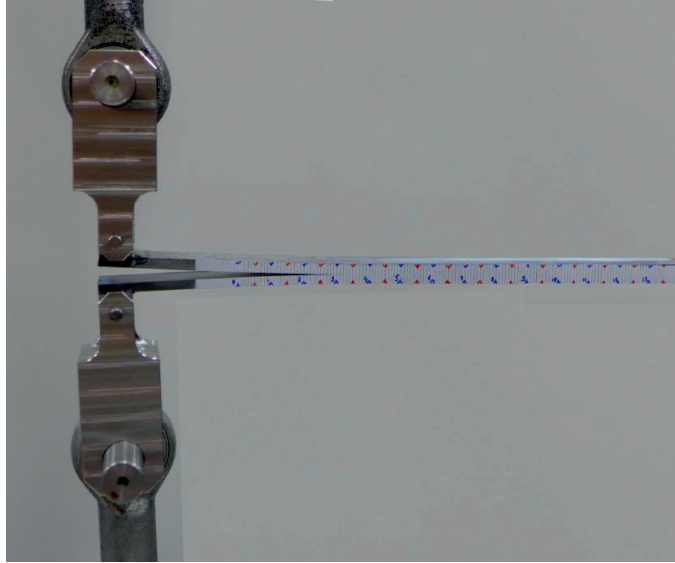
Figure 2.19: Picture of the DCB testing set-up. The marks on the side of the specimens help the monitoring of the crack tip during delamination.

2.5.2 Dogbones testing

To characterize the tensile properties of the adhesive paste Resoltech 3350-3358T, five dogbones specimens are fabricated with the adhesive, cast in molds made of aluminium covered with release agent. To minimize the presence of bubbles in the specimens, a degassing step in a vacuum chamber is applied during 30 seconds. Specimens are cured with the same thermal cycle as CFRP bonded joints: they are held at room temperature during 24 hours and then cured at 70°C in an oven during 5 hours. Then they are removed from the mold and painted with black and white acrylic sprays to obtain a fine pattern proper for DIC (Digital Image Correlation) purposes. A tensile test is performed in an Instron machine on 5 dogbones specimens following the ASTM D638 standard.

(a)

(b)
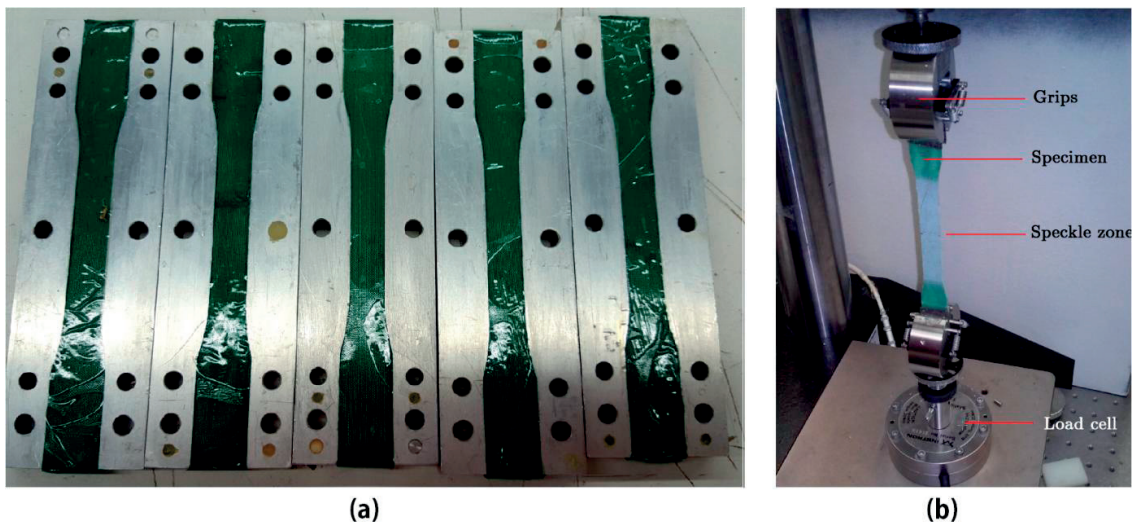
Figure 2.20: Dogbones fabricated with a stacking of adhesive SA80 in aluminium moulds before curing (a), and dogbone tensile test set-up (b).

The load is recorded with a 2kN load cell. A high resolution CCD camera is used to register the images during the test and using the software VIC-2D-2009, the displacement field is extracted from DIC.

To characterize the tensile properties of the adhesive film SA80, dogbones are produced by stacking 8 plies of the adhesive film cut at the dimensions of the mould (see Figure 2.20-a), using cold spray to remove the protective sheet from the adhesive layer. The following curing cycle is imposed: 14h at 80°C under vacuum.

After curing, one side of the samples is painted black and white with acrylics sprays to obtain a very fine speckle pattern which allows to use Digital Image Correlation (DIC, see Section 2.6) for data analysis. A total of 5 dogbones specimens are tested and analysed according to the procedure described in the ASTM D368, using the Instron 5848 machine with a 2 kN load cell (see Figure 2.20-b).

2.5.3 Single Lap Shear test (SLS)

In order to determine the shear strength of the adhesive SA80, Single Lap Shear Test (SLS) are conducted following the specifications of ASTM D3165-07 standard. One side of the samples is painted black and white with acrylic sprays to obtain a fine speckle which allows analysing the data using DIC (see section 3.4). The machine used is a MTS model 809, which is a servohydraulic test system for static and dynamic tests with a 100kN load cell. Hydraulic grips are used with 90bars of applied pressure to ensure that the specimens do not slip during the test. A total of 6 specimens are tested at a rate of 1.27mm/min and pictures are recorded at 0.5 Hz.

2.5.4. Interlaminar shear strength test (ILSS)

Interlaminar shear tests are performed accordingly to ASTM D2344/D2344M-00 using the MTS model 809 with the 10kN load cell and appropriate beams/loading nose and supports (see Figure 2.21).
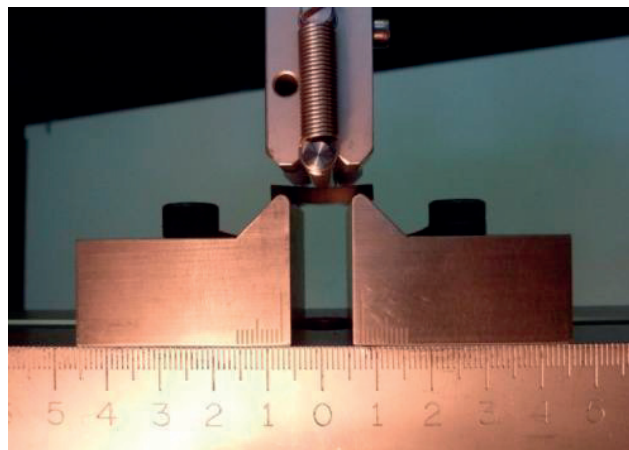
Figure 2.21: ILSS test set-up
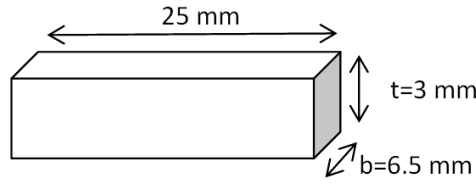
Figure 2.22: ILSS specimens' dimensions

The specimens' dimensions are shown in Figure 2.22. The short beam strength in MPa is calculated using the following equation:

$$F^{sbs} = 0.75 \frac{P_m}{b.h} \qquad \textbf{(2.3)}$$

where P_m is the maximum observed load in [N], b and h respectively the measured specimen width and thickness in [mm].

2.6 Digital Image Correlation in 2D

Digital Image Correlation (DIC) technique is an optical method to determine the displacements fields of an object's surface. This method is used in this thesis for the characterization experiments (SLS and Dogbones tests), and also for determining the extent of mode mixity during a mode I delamination of an asymmetric DCB.

Since accurate 2D image correlation depends on the specimen being planar and parallel to the camera, careful alignment is ensured to obtain highly accurate results.

The principle of this method is to compare successive digital images of an event to estimate the motion of the surface of interest. To be able to perform this comparison, the surface of the sample is sprayed with paint to create a random pattern. For a given point and its signature in the undeformed image, the point having a signature which maximizes a correlation function, is tracked in the deformed image. In practice, a single value is not a unique signature of a point, hence neighbouring pixels, called subsets, are used. Note that to achieve an effective correlation, the speckle patterns must be non-repetitive and must show a high contrast. Two successive image frames from times t and t+Δt are represented by two functions $I_1(x,y)$ and $I_2(x,y)$ respectively. These two images are correlated thanks to an algorithm that minimizes the following correlation error function:

The correlation analysis of dogbones tests is performed with the commercial software VIC-2D® while the correlation analysis of SLS tests is run using a custom Matlab code "VideoextWizard" developed by Dr. J. Cugnoni. The choices of the subset size, step size, and of the splines type for interpolation are test-dependent in order to optimize the robustness and the precision of the analysis, and hence are specified in the dedicated chapters.

2.7 Energy release rate calculation under constant displacement

In this section some basic fracture mechanics concepts based on Griffith's theory (energy approach) are briefly developed.

Assuming a solid with linear elastic properties, containing a through the thickness crack (see Figure 2.23) subjected to a remote force P, the total energy of the body is:

$$\psi = \Pi + W_s \quad \textbf{(2.4)}$$

where Π is the potential energy of the system, and W_s the work required to create new crack surfaces during crack propagation.
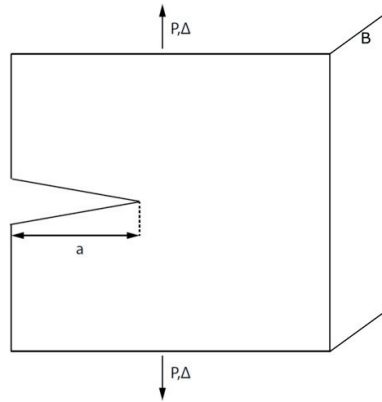
Figure 2.23: Edge crack in a specimen under load

In the case of a constant applied displacement, the work done by the applied load is zero; hence the potential energy is given as:

$$\Pi = U = \frac{1}{2}P\Delta \qquad \textbf{(2.5)}$$

Where U is the strain energy, and Δ the applied displacement.

Irwin defined the Energy Release Rate (ERR), also called G, as the gradient of the potential energy per unit crack extension for a constant displacement:

$$G = \left. -\frac{1}{B}\frac{\partial \Pi}{\partial a}\right|_{\Delta} = \left. -\frac{1}{B}\frac{\partial U}{\partial a}\right|_{\Delta} = -\frac{\Delta}{2B}\left(\frac{\partial P}{\partial a}\right)_{\Delta} \qquad \textbf{(2.6)}$$

Where B is the specimen width.

Introducing the compliance $C = \dfrac{\Delta}{P}$ in eq. 2.6 the ERR becomes:

$$G = \frac{P^2}{2B}\left(\frac{\partial C}{\partial a}\right) \qquad \textbf{(2.7)}$$

2.8 Data reduction methods

In the present DCB tests, the ERR can be expressed as the sum of the energy associated to crack initiation and the energy due to fibre bridging. Thus the total ERR, G_{total}, is calculated using the following expression:

$$G_{total} = \frac{P^2}{2B}\left(\frac{\partial C}{\partial a}\right) = G_{I,i} + G_{I,b} \qquad \textbf{(2.8)}$$

where $G_{I,i}$ is the ERR at initiation and $G_{I,b}$ is the contribution of bridging to fracture resistance.

The compliance measured experimentally is fitted by the following power law, which is a Modified version of the Compliance Calibration Method (MCCM) [45]:

$$C = F(a+H)^m \qquad \textbf{(2.9)}$$

where F, H and m are parameters obtained by least mean square fitting. As the accuracy of the method completely depends on the quality of the fitting, an excellent fit quality is required with a typical R^2 in the range of 0.98 to 1. The compliance is then analytically differentiated. This data reduction method gives a satisfying fitting of the ERR at both initiation and propagation. In some cases the calculated value of the parameter H is too large ($H \geq 70$) and the MCCM is not valid (the numerical fitting fails) hence the Compliance Calibration Method (CCM) [27] is used instead, in which the compliance is fitted as follows:

$$C = Qa^n \qquad \textbf{(2.10)}$$

where Q and n are fitting parameters. The CCM has the advantage to produce an ERR curve with a clear steady state whereas it is difficult to distinguish the plateau on the ERR curve with the MCCM. However the CCM lacks precision to capture the fracture toughness at initiation and at steady state as it is usually found difficult to fit the slope of the compliance curve accurately with this function. Consequently, to improve the compliance fit quality at initiation and at steady state, the parameters Q and n are determined not from all the propagation points, but from adequate selected parts, i.e. from the first propagation points to calculate the ERR at initiation, and from the propagation points at steady state to determine the plateau value.

In the present work, although delamination is accompanied by large scale bridging, the composite behavior is assumed linear elastic based on three reasons:

1) Axial strain measured by FBG sensors during delamination is less than 0.3% which is well below the elastic limit of the material (onset of damage strain is larger than 1% in longitudinal direction). This excludes the possibility of having significant energy dissipation due to secondary damages in the composite beams.

2) As described in the ASTM standard, the residual displacement after unloading in less than 5% of the maximal applied displacement even for long crack lengths. Thus, the non linear visco-plastic effects can be considered negligible.

3) Independent measurements of the ERR are carried out using the J-integral defined as follows:

$$J = P\frac{\theta}{B} \qquad \textbf{(2.11)}$$

where θ is the relative angle between the arms of the DCB specimen measured by DIC (see Figure 2.24). Comparison of these measurements and the ones given by compliance calibration (eq. 2.10) show small differences (<10%) thus, geometrical and material nonlinearities can be considered negligible.
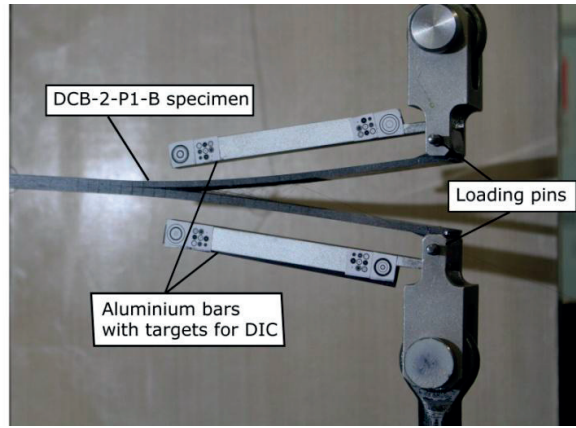
Figure 2.24: DCB-2-P1-B specimen subjected to mode I delamination. Aluminium bars with painted targets are bonded to loading blocks to measure the rotation angle θ with DIC.

2.9 Inspections and microscopy

After delamination of the specimens, transverse sections are polished (down to grit 4000) and observed with a microscope Keyence® VHX5000 with different magnifications from x20 to x1000 to inspect the quality of the cured material (porosity, ply waviness, etc.) and to have an insight on the microstructure heterogeneity of the composite.

Fracture profiles issued from the delaminated surfaces are coated with carbon or iridium and examined with a Scanning Electron Microscope (SEM). The topology of the fracture surfaces is also obtained using the Keyence VHX® microscope images and the VHX-5000-communication software provided by Keyence®.

2.10 Numerical analysis

The different modelling approaches used in this work are presented in this section. All simulations are FE models using the commercial software Abaqus® v.6.12. For all the simulations involving an adhesive layer, the composite and the glue are introduced as separate parts tied together. One of the surfaces is the master surface whereas the other is the slave surface. For all the FE models where a seam is introduced to simulate the crack, elements are collapsed at the crack tip and their mid-

nodes are shifted to ¼ of the edge to create a $1/\sqrt{r}$ singularity (*r* being the distance from the crack tip).

2.10.1 Virtual Crack Closure Technique (VCCT)

Since the crack starter is not placed at the midplane of the asymmetric DCB specimens, the asymmetry may cause a non negligible component of mode II even during mode I loading. A numerical study using the VCCT is carried out to quantify the amount of mode II as a function of the crack starter position, in absence of bridging tractions on the crack faces. Indeed by extracting the forces at crack tip and displacements in the vertical and horizontal directions (see Figure 2.25), the VCCT allows determining the mode I and II ERR components G_I, G_{II}, respectively, using the following formulas:

$$G_I = -\frac{1}{2.\Delta a} F_y (u_y - u'_y) \qquad \textbf{(2.12)}$$

$$G_{II} = -\frac{1}{2.\Delta a} F_x (u_x - u'_x) \qquad \textbf{(2.13)}$$

Figure 2.25: Virtual Crack Closure technique: extracted valued at the nodes to determine the fracture components in mode I and mode II

VCCT is based on Irwin's crack closure integral and assumes that when a crack grows, the energy release is equal to the energy necessary to close the crack. This numerical method is simple and effective, though the elements size must be chosen carefully: if they are too small the solution does not converge since the VCCT suffers from stability issues (stress oscillation close to singularity in the FE model), whereas if the elements are too large the precision decreases. All models are 2D plain strain models, with the 20 μm thick initial crack contained in the upper beam. Both components of Strain energy release rate at the crack tip in mode I and in mode II, (ENRRT1 and ENRRT2 respectively) are extracted to calculate the mixed mode ratio.

2.10.2 Contour integral evaluation

For linear elastic materials, the value of J-integral, *J*, is the same as the ERR. Thus 2D plane strain FE-models are constructed to compare the J-integral values at initiation of bulk and joints configurations. The phenomenon of bridging is not taken into account, since tractions are not applied on the crack faces at initiation. The elasto-plastic behavior (Von Mises plasticity) of the adhesive layer is introduced as a material behavior. Around the crack tip, a refined radial mesh is employed to

26

extract the contour integrals (see Figure 2.26). The crack front is modelled with a sharp tip and singular elements are generated to capture the crack tip fields. Calculation of at least 10 contour integrals are carried out for each configuration. The simulations are performed with displacement control at the loading pins with a value corresponding to the experimental displacement at onset of crack propagation. Quadrilateral plane strain elements with reduced integration (CPE8R) are employed.
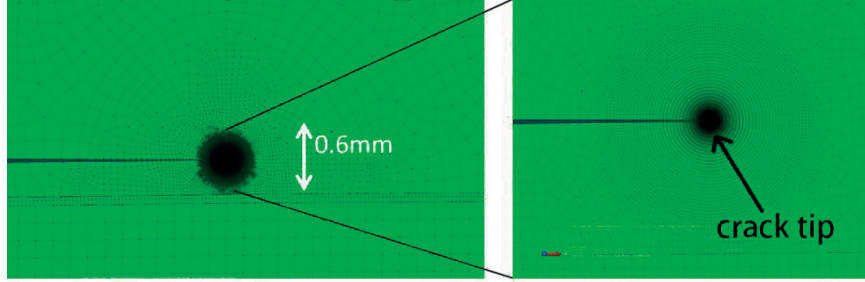
Figure 2.26: refined radial mesh to extract contour integrals

2.10.3 Inverse method to identify bridging tractions

This method [18] consists in an inverse numerical identification scheme that matches the longitudinal strain distribution obtained from the FGB's with those simulated by the FE model, in order to identify the involved bridging tractions. The basic principle of this method is based on the fact that local bridging tractions affect the local curvature of the DCB arms and thus introduce a perturbation of the longitudinal strain field in the bridging zone. The configurations DCB2-P1-A1 (joint) and DCB2-P1-B (bulk) are simulated with 2D-plane strain FE models. A parametric surface traction $\sigma_b(z)$ is implemented to represent the bridging zone as follows:

$$\sigma_b(z) = e^{-\gamma z}\left(\sigma_{max} - \frac{\sigma_{max}}{z_{max}}z\right), \quad 0 \leq z \leq z_{max} \qquad \textbf{(2.14)}$$

where γ is an identified parameter taking into account the non linearity of the tractions, σ_{max} is constant and represents the maximum tractions at the crack tip; z_{max} is the maximum bridging length, extracted from the experimental results of crack length vs. displacement. The value of z_{max} can also be extracted from the experimental R-curve.

The simulation is run with an initial guess for the parameters of the bridging tractions, and the simulated axial strain profile ε_{FEM} is extracted at the upper surface of the sample, corresponding to the exact location of the FBG sensors embedded in the optical fibre 2, where the measured axial strain profile ε_{FBG} is extracted. Then ε_{FEM} is compared to ε_{FBG}, and an error vector is calculated using the following equation:

$$F(\sigma_{max}, \gamma, z_{max}, \chi, h) = \frac{1}{2}\left\|\frac{\varepsilon_{FBG} - \varepsilon_{FEM}}{\langle\varepsilon_{FBG}\rangle}\right\|^2 \qquad \textbf{(2.15)}$$

Where $\sigma_{max}, \gamma, z_{max}$, are the parameters of the bridging tractions and χ and h are two additional parameters to take into account respectively the uncertainty on crack tip position (the crack length is allowed to vary by $\chi = \pm 2$ mm) and the actual strain transfer coefficient that accounts for the geometrical offset of the actual position of the FBG with respect to the top surface of the FE model.

Indeed the strain data from the 2D model are extracted at the surface of the CFRP specimen, whereas in reality the FBG sensors are slightly above the surface (estimated at 0.063mm from the surface, this distance corresponds to half a fibre diameter). By a linear extrapolation of the strain field between the surface of the specimen and the centre of the optical fibre, the FE simulated strains can be corrected to match those measured at the FBG location. This strain transfer parameter h is estimated as a first guess at 1.0677.

The best set of the 5 parameters is found by minimizing the nonlinear problem (eq. 15) with the 'lsqnonlin' optimization routine of Matlab R2015b based on a nonlinear least-squares minimization algorithm. The residual error norm defined in eq.2.15 is minimized using the trust-region-reflective Newton's algorithm. The Jacobian of the error is evaluated by direct finite difference of the FE solution with a relative perturbation of the parameters of 1%. The optimisation process ends when the variation of the residuals is lower than a given threshold, or if the maximum allowed number of iterations is reached. Note that the optimization was then repeated for different sets of initial values to verify the uniqueness of the solution.

In a second phase the fracture toughness at initiation $G_{I,i}$ is taken into account in the optimization process. For that purpose the contour integral J_{tip}, extracted at the refined elements surrounding the crack tip, is appended to the error vector as follows:

$$F\left(\sigma_{max}, \gamma, z_{max}, \chi, h\right) = \frac{1}{2} \left\| \frac{\varepsilon_{FBG} - \varepsilon_{FEM}}{\langle \varepsilon_{FBG} \rangle} ; \omega \frac{J_{tip} - G_{I,i}}{G_{I,i}} \right\|^2 \quad \textbf{(2.16)}$$

where ω is the weight attributed to the initial fracture toughness in the optimization and the operator ";" represent the concatenation of 1D vectors. Note that J_{tip} is theoretically domain-independent as bridging tractions are present, but to verify this assumption, contours are extracted through the 10 first rings of elements (distance to crack tip < 5 mm) neighbouring the crack tip, and only the converged value is taken into account.

The Crack Opening Displacements (CODs), $\delta(z)$ extracted from the numerical model, are then combined with the bridging tractions $\sigma_b(z)$ to obtain $\hat{\sigma}_b(\delta) = \sigma_b(\delta(z))$. The contribution of bridging $G_{I,b}$ to the total ERR, G_{total} is calculated with the following equation [9]:

$$G_{total} = G_{I,i} + G_{I,b} = G_{I,i} + \int_0^{\delta_{max}} \hat{\sigma}_b(\delta) d\delta \quad \textbf{(2.17)}$$

In some cases, σ_{max}, z_{max} and in turn δ_{max} can be estimated, for example based on the work of Farmand-Ashtiani [21]. In those cases, it is possible to estimate the remaining parameter γ in such a way that the numerical integration $\int_0^{\delta_{max}} \hat{\sigma}_b(\delta) d\delta$ corresponds to the contribution of bridging $G_{I,b}$.

Cohesive element simulation

Cohesive elements are a very efficient method of simulating crack propagation using FE method. Cohesive elements in a FE model do not correspond to any physical continuum material behavior but instead represent the cohesive forces that occur in the fracture process zone when material elements are being pulled apart, as it is the case in delamination, following a traction-separation curve, also called the *cohesive law*. Many types of cohesive traction separation can be used to model

different type of fracture processes but the most common cohesive law is simply a bilinear relationship. In this case, the stress developed in a cohesive element is directly related with the local COD, and this traction-separation relation consists of two parts:

- First the behavior is linear elastic, characterized by the penalty stiffness K_p (see Figure 2.27) until the critical stress level σ_c and the corresponding displacement δ_c are reached. The damage D is zero.
- A second part in which the tractions decrease to zero, is associated to the fracture of the polymer matrix and the creation of new surfaces. This softening behavior of the cohesive elements is correlated to damage following the relation $K = (1 - D(\delta))K_p$ with K the degraded penalty stiffness for $\delta > \delta_c$. Hence when the COD reaches a given value δ_f, corresponding to a damage D =1, the rigidity of the elements is zero, meaning that they cannot carry any load.
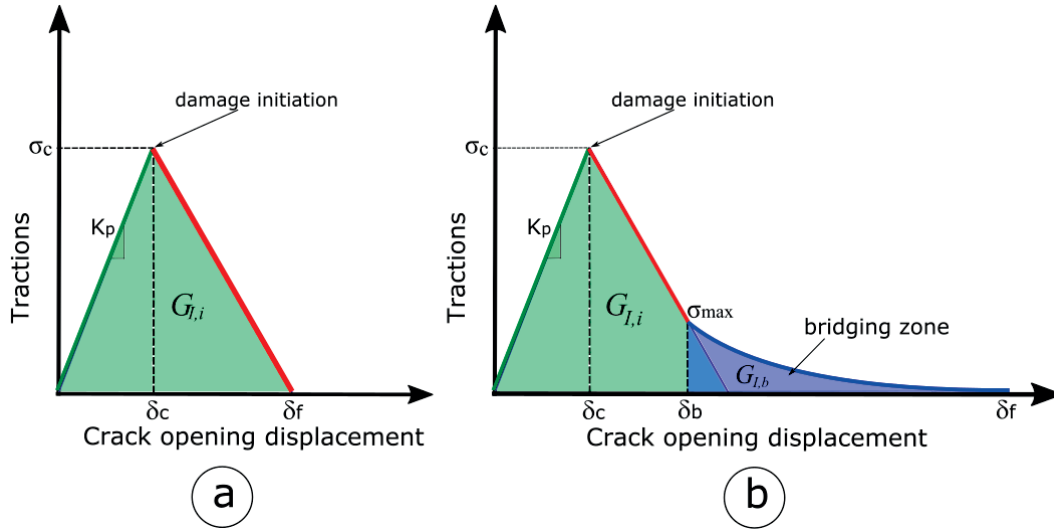
Figure 2.27: Constitutive behavior of a cohesive element without fibre bridging (a), and modified for fibre bridging (b).
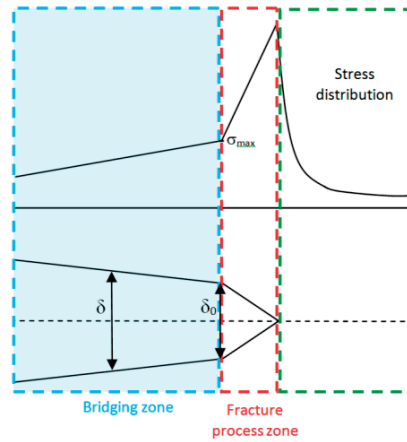
Figure 2.28: Schematic of the stress distribution with respect to the crack.

29

Note that the area under this curve is equal to the initiation fracture toughness $G_{I,i}$ (see Figure 2.27-a). This generic bilinear cohesive law (see Figure 2.27-a) cannot be applied if a toughening mechanism like fibre bridging occurs. To take into account the energetic contribution of bridging, the identified bridging law from the previous section $\hat{\sigma}_b(\delta)$ is appended to the second part of the traction-separation curve (see Figure 2.27-b). The maximum tractions associated to bridging are supposed to be at the crack tip, σ_{max} corresponding to an opening displacement δ_b, followed by a non linear decrease that tends to zero at the critical opening corresponding to the end of bridging zone. In this hybrid cohesive law, the first bilinear part represents the brittle matrix dominated fracture corresponding to $G_{I,i}$ while the nonlinear tail part represents the large scale bridging tractions due to bridging and corresponding to the fracture energy $G_{I,b}$.

This multi-process cohesive law is finally implemented through a tabular multi-linear damage evolution law with at least 300 entries for a good interpolation by the numerical solver. The overall behavior can be summarized as follows:

1: $\qquad D(\delta) = 0$ for $0 < \delta < \delta_p$

2: $\qquad D(\delta) = \dfrac{\sigma_c + \left(\dfrac{\sigma_{max} - \sigma_c}{\delta_0 - \delta_c} \right)(\delta - \delta_c)}{K_p \delta}$ $\qquad$ for $\delta_c < \delta < \delta_b$

3: $\qquad D(\delta) = 1 - \dfrac{\hat{\sigma}_b(\delta)}{K_p \delta}$ $\quad$ with $\delta_b = \delta - \delta$ $\qquad$ for $\delta_b < \delta < \delta_f$

A cohesive element model is run for each configuration (DCB2-P1-B and DCB2-P1-A1) by introducing the respective identified bridging functions for the second part of the cohesive law.

Note that for some cases, the bridging law implemented in the second part is not obtained from strains measures with FBG sensors, but by identification of the bridging parameters σ_{max}, γ, and z_{max} with values respecting the following physical considerations:
- σ_{max} must be smaller than the tensile strength of the epoxy matrix
- z_{max} must be smaller than the distance between the Teflon insert and the crack tip
- The decrease is monotonic, $\gamma > 0$.

For the first part of the cohesive law, the needed parameters (damage initiation, penalty stiffness, etc...), are specified for each case in the dedicated chapters. The value of the penalty stiffness is estimated by performing a convergence study in which the stiffness is increased gradually until the results become insensitive to this parameter.

To verify the cohesive model predictions, the displacement and reaction force are finally extracted from the 2D-cohesive elements model and compared with the experimental load-displacement curve. The quality of the agreement determines if the model can successfully predict the delamination behavior of a specimen with a given configuration.

Chapter 3: Mode I delamination of DCB2-P1-B bulk specimens

3.1 Assessment of bridging model at intermediate propagation states

It has been demonstrated in several studies [21,50,51] that the inverse identification method based on strains from FBG sensors in the steady state propagation satisfactorily predicts the load-displacement curve of composite DCB specimens, following the semi-experimental procedure described in Section 2.10.3.

The question addressed here is whether the cohesive traction-separation relation identified at steady state remains valid throughout the transition phase, i.e. after initiation, and before reaching a fully developed bridging. Thus the objective is to use the inverse identification methodology with FBG sensors placed in the steady state region, and to predict the strain profile occurring in the early stage of delamination, in the transition state.

To achieve this goal, two optical fibres containing 10 FBG sensors each are bonded on the surface of a DCB2-P1-B specimen (see Figure 3.29). The first optical fibre is bonded in the transition state region of the specimen, while the second is bonded in the steady state region. The specimen is delaminated under mode I with the same conditions as the other specimens. The strains at steady state are obtained and an identification of the parameters is performed.
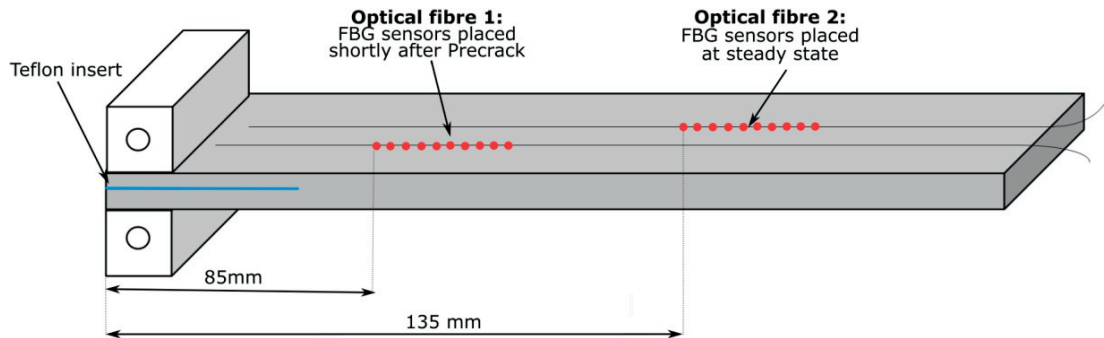
Figure 3.29: DCB2-P1-B specimen with 2 optical fibres on the upper surface, with the FGB sensors placed at transition state and at steady state.

From the identified traction-separation relation, a damage law is implemented in a CZM model.

The purpose is to extract the strains from the model where the FBG sensors are located at the time the crack tip reaches them, and compare the simulated strain profile to the experimental one (measured by the FBG sensors from optical fibre 1). A flow chart of the adopted approach is displayed in Figure 3.30.
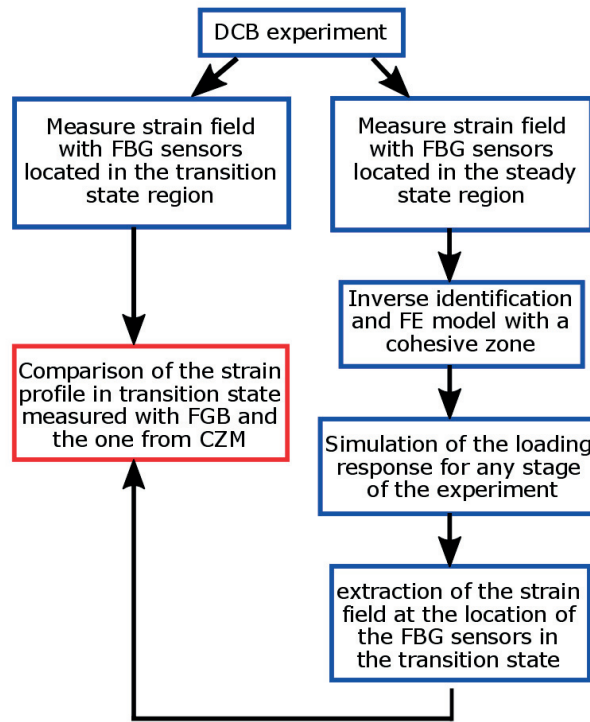
Figure 3.30: Flowchart of the approach used to assess the capability of the inverse method identification to predict strain field at early stage of delamination.

3.1.1 Specimen preparation, delamination test and data reduction

Specimen preparation

Two optical fibres with 10 FBG sensors each, are bonded on the surface of a DCB2-P1-B specimen (see Figure 3.29). The first fibre is positioned so that the sensors are in the region close to the precrack end, where the bridging zone will not be fully developed during delamination, targeting a crack length in the raising part of the R-curve. The second optical fibre is placed to capture the strains profile at steady state, expected to be around 60mm from the precrack tip (based on the ERR curve of other DCB2-P1-B specimens from the same material).

Delamination test

A precracking stage is first carried out to avoid the influence of the resin rich region ahead of the release film. As soon as the pop-in is noticed (a small jump on the load-displacement curve), the specimen is unloaded. The specimen is then delaminated under mode I with a constant cross-head speed of 1mm/min. During delamination, the load, displacement and crack length are measured, and the FBG sensors response is recorded at 1 Hz using an SM130 interrogator from Micron Optics. Then the wavelength data are converted to strain data following the procedure described in section 2.4.1. Using the recorded strain and crack length data, the strain versus time curves are converted to strain vs crack length curves for further bridging traction identification.

The load displacement response of the DCB2-P1-B is shown in Figure 3.31.
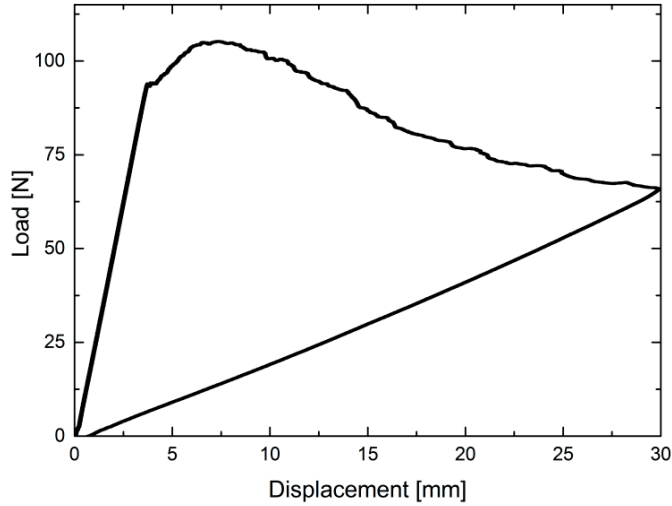
Figure 3.31: Experimental load displacement curve of bulk specimen DCB2-P1-B equipped with 2 optical fibres.

Data reduction method

The compliance calibration data reduction method (CCM) is considered to calculate the ERR curve in this experiment: indeed as explained in section 3.1.1, the MCCM (data reduction method with the modified power law) is not valid for a fitting parameter H>70, which is the case here.

As described in section 2.8, a linear fit of the plot of log (δ_i/P_i) versus log (a_i) is performed, and the slope n is used in the calculation of the Mode I interlaminar fracture toughness as follows :

$$G_I = \frac{nP\delta}{2Ba} \quad \textbf{(3.1)}$$

The value of n is strongly dependant on the range of propagation points taken into account: a significant difference is observed when the slope is calculated over the whole range of propagation values versus if only initiation values of compliance and crack length are considered. The linear fit of the first case is shown in Figure 3.32.a (blue curve). The slope at initiation is not well captured, leading to a large overestimation of the fracture toughness. Hence it is necessary to display the ERR calculated with the three different approaches (see Figure 3.33):

- Case 1: with the slope n calculated with only the 4 initial propagation points for initiation
- Case 2: with n calculated within the steady state range, and
- Case 3: with n calculated from all propagation points.
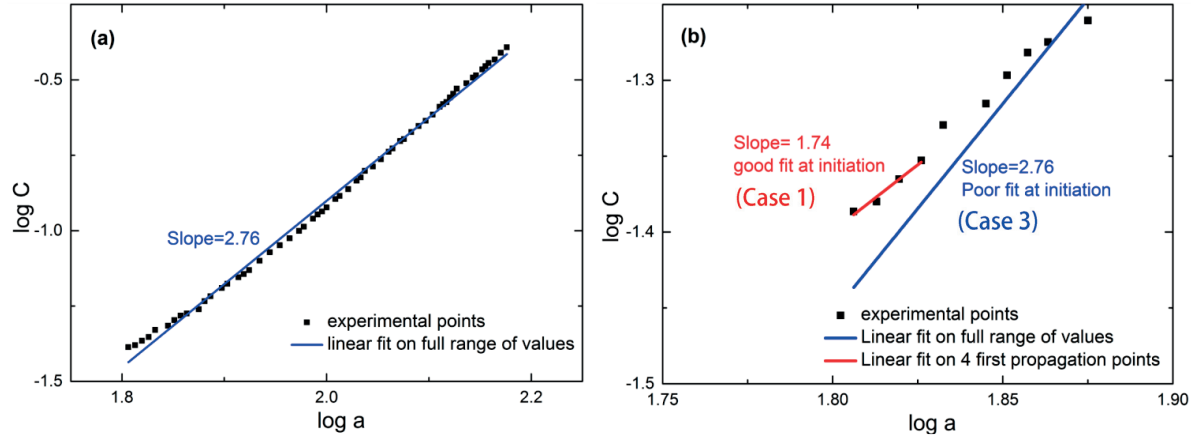
Figure 3.32: Linear fit of the Compliance as a function of crack length in log scale on (a) all propagation values (case 3) and on (b) zoom at initiation (case 1).
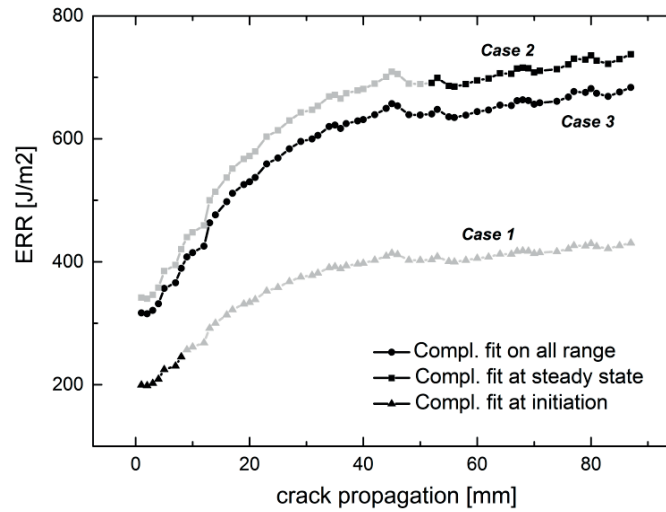
Figure 3.33: Representative R-curves for specimen DCB2-P1-B with 2 optical fibres, calculated with CC Method as follows: slope n calculated with the 4 initial propagation points (Compliance fit at initiation, case 1) ; slope n calculated within the steady state range of values (case 2), and slope *n* calculated on the full range (case 3). Black dots are used for the valid domain while grey dots for the invalid domains.

The difference in terms of ERR between case 2 and case 3 is about 25 J/m^2 at initiation and about 50 J/m^2 at steady state. As the fit of the compliance for case 2 is very good at steady state, it can be considered that it gives the correct ERR value for steady state (Δa > 60mm). The difference of fracture toughness is much more pronounced with case 1: the onset of propagation is calculated at 200 J/m^2, hence 115 J/m^2 lower than case 2. For clarity sake, the whole ERR curve is plotted in Figure 3.33 with the values calculated from case 1, but only the first points (at initiation) can be considered valid for comparison. Considering the above comments, the initial fracture toughness is estimated around 200 J/m^2, and the plateau value at steady state at 720 J/m^2.

3.1.2 Extraction and correction of the strain data

Extraction of the strains distribution at steady state

Each multiplexed FBG sensor gives a wavelength measurement which is recorded during the delamination test. The observable change of wavelength for each FBG sensor during the experiment is correlated with the strains values using equation 2.1, which are matched with crack length data and FBG positions (OLCR measurements) to obtain a point-wise strain profile for each optical fibre. The strains measured by the sensors in a range of ± 1.5mm around the target crack length (half of the distance separating 2 sensors) are combined to reconstruct a quasi continuous strain profile (see Figure 3.34).
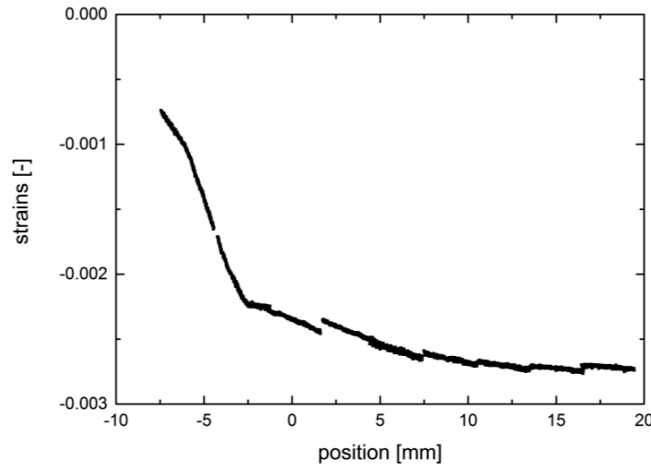
Figure 3.34: Quasi continuous strain field obtained from FBG data for a given crack length (140mm in this case). This strain profile is obtained from the measurements of the optical fibre 2 (located in the steady state region).

Correction of the strains with a 4-Point-Bending test

The optical fibre is bonded at the surface of the specimen hence the transfer of strains can be affected by the compliance of the adhesive layer or microbubbles in the adhesive and thus must be corrected. To obtain an estimation of the needed correction, a 4 point bending (4PB) test has been carried out on the upper delaminated part of the specimen containing the optical fibres after full delamination. The strains measured by the 10 FBG sensors in optical fibre 2 are plotted versus time (see Figure 3.35), and the slope is calculated in the linear part (between 60s and 90s) by a linear fit for each sensor. As the bending moment should be uniform in this section of the beam, all curves should ideally be superimposed. Each slope is normalized by the mean of the 10 slopes and plotted against FGB sensor position obtained from OLCR measurements (see Figure 3.37). A correction vector is constructed to bring all the data to the reference, which corresponds to a perfect transfer of the strains (see Figure 3.37). Finally, strain data from each FBG sensor is divided by the corresponding value of the Correction Vector (see Table 3.2). Please refer to Appendix 1 for the Matlab code leading to this Correction Vector. Before correction, the measured strains data are not superimposed (see Figure 3.35) whereas the match is perfect after correction (see Figure 3.36), except for the 10th FBG sensor that gives a non linear response (possible debonding) and its signal is consequently not considered in the optimization process. This method to correct the strains measured by FBG sensors

involving a 4PB test is considered reliable, fast and simple, and thus could be implemented for any experiment with FGB's sensors to obtain a trustable strain distribution.
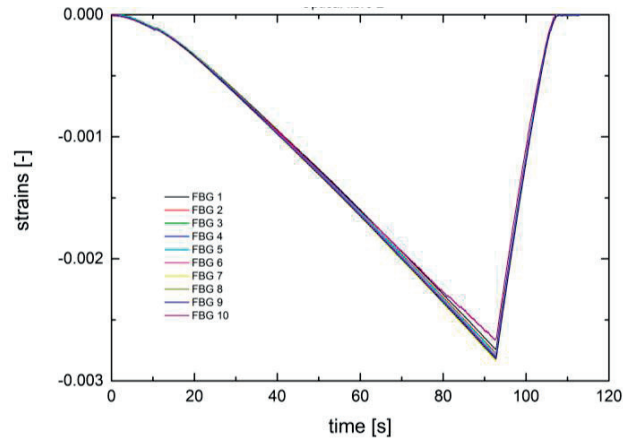
Figure 3.35: Strains recorded by the 10 FBG sensors of optical fibre 2 during a 4 point bending test without correction.
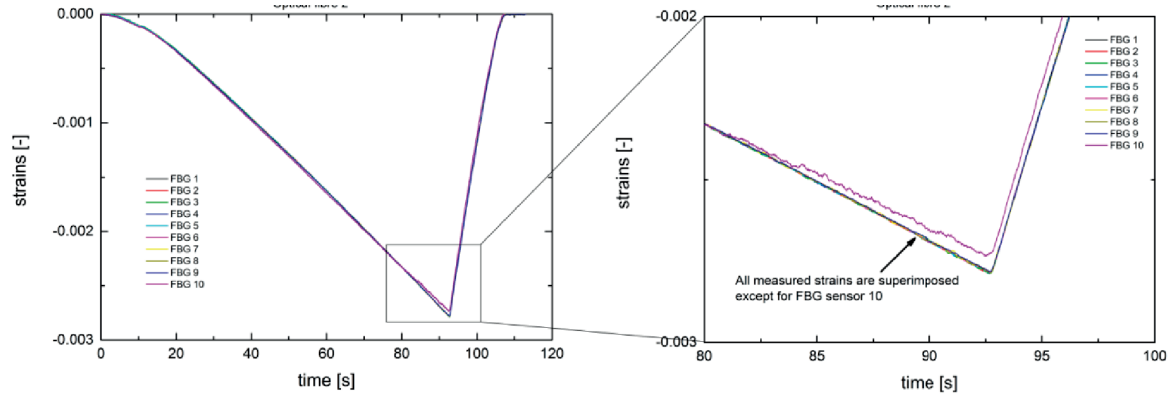
Figure 3.36: Strains recorded by the 10 FBG sensors of optical fibre 2 after correction.
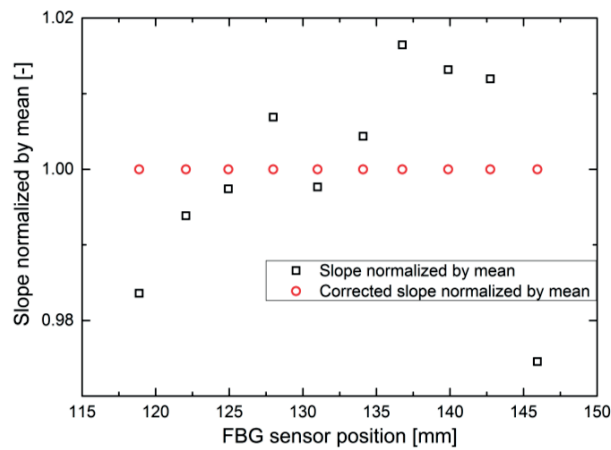
Figure 3.37: Corrected and uncorrected values of slopes normalized by mean from the 4PB test.

FGB sensor	1	2	3	4	5	6	7	8	9	10
Correction value	0.9836	0.9939	0.9974	1.0069	0.9977	1.0043	1.0165	1.0132	1.012	0.9746

Table 3.2: Correction factor for each FBG sensor strains data calculated from the 4PB test

To obtain the strain distribution shown in Figure 3.34, a quasi continuous strain field is assumed. All those superimposed strains values are concatenated and sorted to obtain a representative strain profile (see Figure 3.38.b, black curve). To reduce the sensitivity of the identification to noise, the curve fitting tool from Matlab® is used to smooth the strain profile: a smoothing spline with a smoothing parameter p = 0.99 gives a new strain distribution. Original and smoothed curves are represented in Figure 3.38.b. The latter is used as an objective strain distribution in the optimization process to identify the bridging tractions. As a fully developed bridging is needed to identify all the parameters, only the strains data from optical fibre 2 sensors is used in the identification.
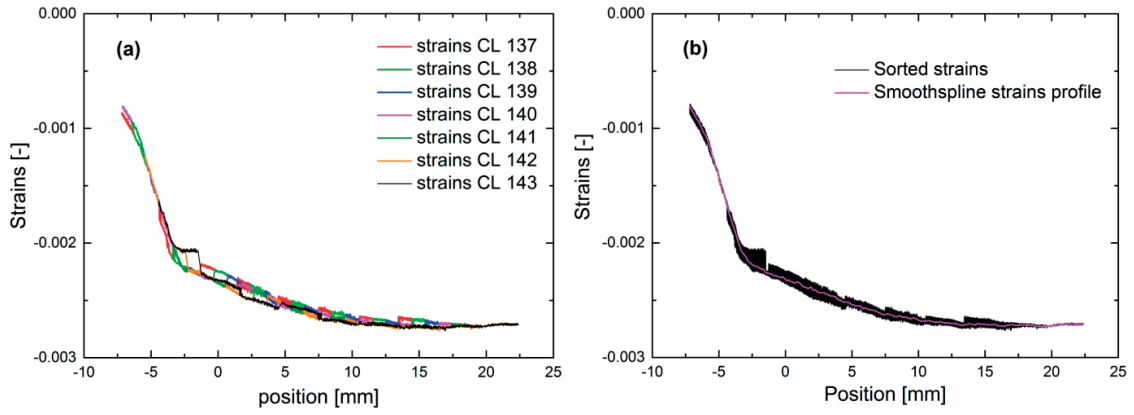
Figure 3.38: (a) Superposition of strains profiles from optical fibre 2 FBG sensors (long crack) for different crack lengths. (b) Concatanated strain data (black curve) and smoothened strain profile of the same data (pink curve). The latter is used as objective input function in the optimization process.

3.1.3 Identification of bridging tractions

Two successive numerical models are employed to complete the DCB2-P1-B analysis.

First a 2D plane strain model of the DCB2-P1-B specimen configuration is simulated, with a parametric bridging traction $\sigma_b(z)$ at the surface of the crack, between the initial crack length and the crack tip. Those tractions are applied vertically to exercise only closing forces (see Figure 3.39). The model should represent realistically the situation when the axial strains distribution ε_{FBG} is measured, thus the experimental crack length and applied displacement are imposed in the simulation. The modulus E_{11} introduced in the FE model is corrected to 109 GPa (instead of 120 GPa) to match the experimental compliance at the onset of delamination.

The global mesh size is set to 0.5mm using CP8R quadratic elements with reduced integration, and a radial mesh refined around the crack tip (see Figure 3.40) with structured quadratic elements allows to extract J integral values corresponding to the ERR at the crack tip ($G_{I,i}$).
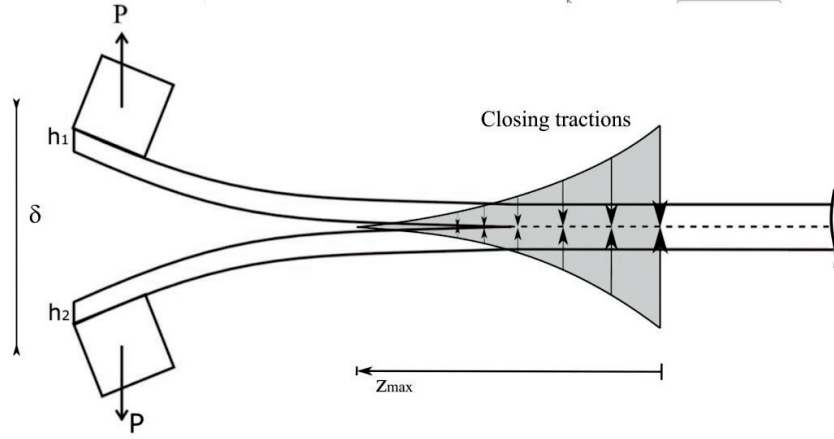
Figure 3.39: Schematic of the numerical model employed in the optimization process.

The simulation is run with an initial guess for the 5 parameters ($\sigma_{max}, \gamma, z_{max}, \chi, h$; see section 2.10.3) of the bridging tractions, and the simulated axial strain profile ε_{FEM} is extracted at the upper surface of the sample, corresponding to the exact location of the FBG sensors embedded in the optical fibre 2, where the measured axial strain profile ε_{FBG} is extracted. Then ε_{FEM} is compared to ε_{FBG}, and an error vector is calculated using eq. 2.14. The optimization process described in section 2.10.3 is employed to minimize the error vector.
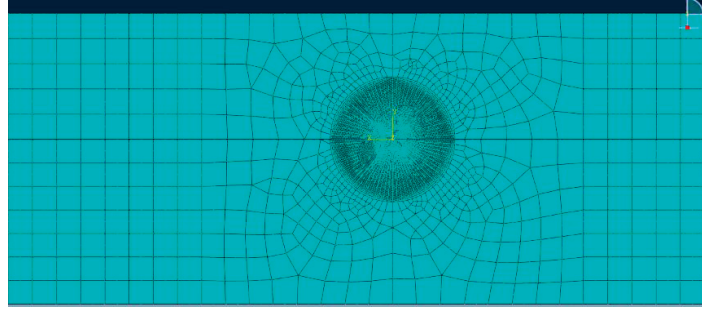
Figure 3.40: Discretization of the 2D plane strain FE model used in the optimization process to identify the bridging tractions with a refined mesh at the crack tip. Note that both arms of the specimen are simulated since it is asymmetric due to the position of the crack two plies above the specimen mid-thickness.

After optimization, the bridging tractions $\sigma_b(z)$ is combined with the crack opening displacement $\delta(z)$ extracted from the FE model to finally obtain the traction-separation law $\hat{\sigma}_b(\delta)$. By integration over the corresponding COD, $G_{I,b}$ is obtained.

In a second phase, the fracture toughness at initiation $G_{I,i}$ = 320 J/m^2 (for a typical DCB2-P1-B specimen) is taken into account in the optimization process as an additional objective. For that purpose the weighted error in crack tip ERR between the experimental value $G_{I,i}$ and the numerically calculated J-integral, J_{tip}, is appended to the error function as follows:

$$F\left(\sigma_{max}, \gamma, z_{max}, \chi, h\right) = \frac{1}{2} \left\| \frac{\varepsilon_{FBG} - \varepsilon_{FEM}}{\langle \varepsilon_{FBG} \rangle}; \omega \frac{J_{tip} - G_{I,i}}{G_{I,i}} \right\|^2 \quad \textbf{(3.2)}$$

where ω *is* the weight attributed to the initial fracture toughness in the optimization. Three different weights are used, leading to three sets of identified parameters that are referred as:

- OPTIM 1: (see Figure 3.41.a) solution resulting from the optimisation to minimize the error vector with a weight of zero for $G_{I,i}$ (this case actually corresponds to the error vector expressed in equation 2.14).
- OPTIM 2: (see Figure 3.41.b) solution resulting from the optimisation to minimize the error vector with a weight ω of 10%.
- OPTIM 3: (see Figure 3.41.c) solution resulting from the optimisation to minimize the error vector with a weight ω of 50%. Note that for this last case, the experimental strains data from FBG sensors at the corner (very close to the crack tip) are not taken into account in the optimization process.

	Identified parameters										
	weight ω (%)	γ	σ_{max} (MPa)	z_{max} (mm)	χ (mm)	h	Sum square error vector	G_b J/m^2	J_{tip} J/m^2	G_{total} J/m^2	error on J_{tip}	Error on force (N)
OPTIM 1	0	0.0276	0.72	49.819	2.415	0.971	0.072	555	176	**730**	-	0.8
OPTIM 2	10	0.00461	0.37	46.641	2.166	0.974	2.529	470	246	**716**	-22%	0.5
OPTIM 3	50	0.00385	0.22	55.990	2.023	0.985	1.965	396	314	**710**	0%	0.9

Table 3.3: Summary of the 3 optimized models

3.1.4 Cohesive zone modelling

For each of the 3 optimized set of parameters, the traction-separation relation $\hat{\sigma}_b(\delta)$ is reconstructed from $\sigma_b(z)$ and is used to predict the loading response of the considered specimen using the procedure described in section 2.10.4. For this purpose, the geometry of DCB2-P1-B specimen is reproduced in a 2D plane strain cohesive model built using 65447 quadrilateral quadratic elements with reduced integration for CFRP beams, and 6080 quadrilateral linear cohesive elements (Abaqus COH2D4) with a thickness of 20 μm for the cohesive layer. Three cohesive elements simulations, Model 1; 2 and 3, are performed with the damage laws defined by the traction separation relation obtained respectively with OPTIM 1, 2 and 3. For each model, the damage law is introduced as a cohesive element property in a tabular form with at least 300 entries for a good interpolation by the numerical solver.

The load-displacement curves obtained from experiment and from models 1 to 3 are displayed in Figure 3.42. None of the models is able to capture the initiation part of the experiment, though it is noticeable that the higher the weight of the initial fracture toughness $G_{I,i}$ in the optimization, the closer the solution: predicted curve from Model 3 almost reaches the onset of nonlinearity. It is worth noting that the calculated fracture toughness at initiation J_{tip} predicted by Model 1 (see Table 3.3) is close to the experimentally calculated $G_{I,i}$ with a fit of the compliance at initiation. For the steady state region (from 18mm displacement) all predicted curves are in very good agreement with

experimental data, solution from Model 1 slightly overestimates the loading response, which is consistent with the calculated value of G_b with OPTIM 1 (730 J/m^2), see Table 3.3. Model 2 matches very well the experimental curve at steady state and Model 3 slightly underestimates it.
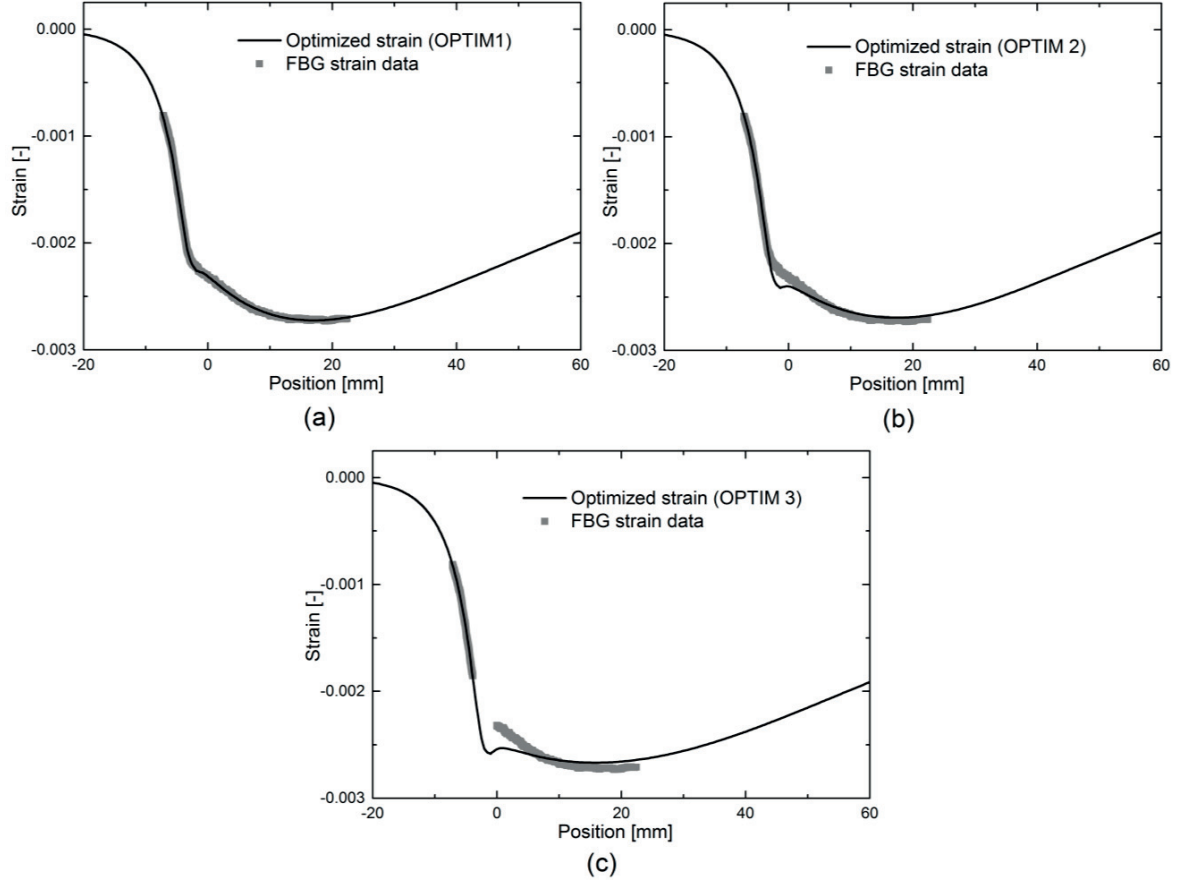
Figure 3.41: Experimental strain data from FBG sensors inscribed in optical fibre 2 and the corresponding strain distributions from the optimized numerical solution with a zero weight for $G_{I,i}$ (a) in the error vector, a weight of 10% (b), and a weight of 50% (c).

In the region of interest of this experiment comprised from 4 to 15mm displacement, which corresponds to the raising part of the ERR curve, none of the 3 cohesive models is able to predict accurately the loading response. Nevertheless it can be observed that Model 1 and 2 offer a satisfying match in the raising part for a displacement above 12mm, making those models more likely than Model 3 to predict the strain distribution at an early stage of delamination.
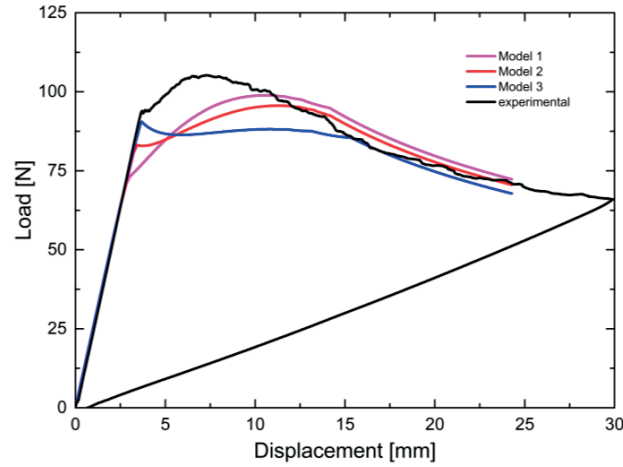
Figure 3.42: Experimental and simulated load displacement curves

3.1.5 Prediction of strains distribution for a short crack

The strain data from FGB sensors inscribed in optical fibre 1 are extracted at 4 different crack lengths (24 to 27mm), then all the values are concatenated and sorted to obtain a representative strain distribution (see Figure 3.43).
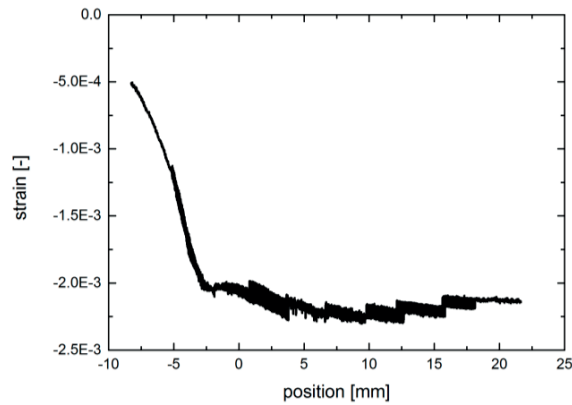
Figure 3.43: Strains distribution obtained by concatenation of strain profiles measured by the optical fibre 1, at 4 different crack extensions (24 to 27mm). The goal of this study is to predict these strains by running an identification of bridging tractions with, as an input data, the strains distribution measured at steady state.

First of all it is necessary to check that the strains from the optical fibre 1 are extracted at a crack length among the transition state, and as shown in Figure 3.44, this condition is satisfied: the strains are extracted in the raising part of the steady state in the ERR curve (before the plateau).

42
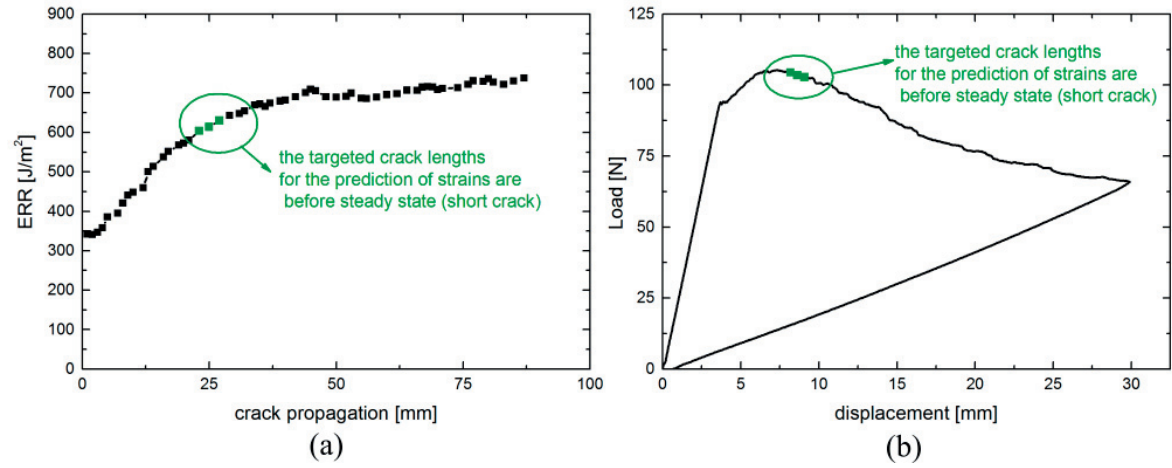
Figure 3.44: experimental ERR and load displacement curves of the specimen with 2 optical fibres, and the region where strains are extracted from optical fibre 1.

As the complete loading response history is obtained from the 3 cohesive simulations (Model 1; 2 and 3), the axial strain profile can as well be extracted from each model at the location of the fibre 1, corresponding to a short crack length (25mm) as the one extracted from optical fibre 1. The three strain profile predictions (from Model 1; 2 and 3) are shown in Figure 3.45.

The best fit is clearly obtained by the Model 1 which captures successfully the entire measured strain distribution. The Model 2 fails to capture the part of the corner (around crack tip) but fits very well otherwise. Finally Model 3 strain prediction fails to fit the experimental data, with a small overshoot at the corner and an underestimation of the strains in the bridging zone. Nevertheless all the models successfully predict the order of magnitude of the strain profile for a crack length of 93 mm.

Moreover, all three models seem to be able to predict the correct crack length: indeed all fits ahead of the crack tip position (usually seen before the corner in the strain profile) are very good, and thus an accurate prediction of crack propagation is expected.

To verify this, the crack length is extracted from each model at 4 different steps of the experiment (corresponding to applied displacements of 7; 12; 18 and 24mm) and compared to the visual crack length. The crack tip is defined as the point where the damage D>0.99. Results (see Figure 3.46) show that all 3 models successfully predict the crack length at different times of the loading, especially Model 1 that gives an accurate prediction for almost all the considered stages of delamination (error below 3.5 mm). Note that the uncertainty of crack length is about 2 mm, attributed to the bowed shape of the crack front, hence it is not exactly equal to the crack length measured on the specimen's edge.
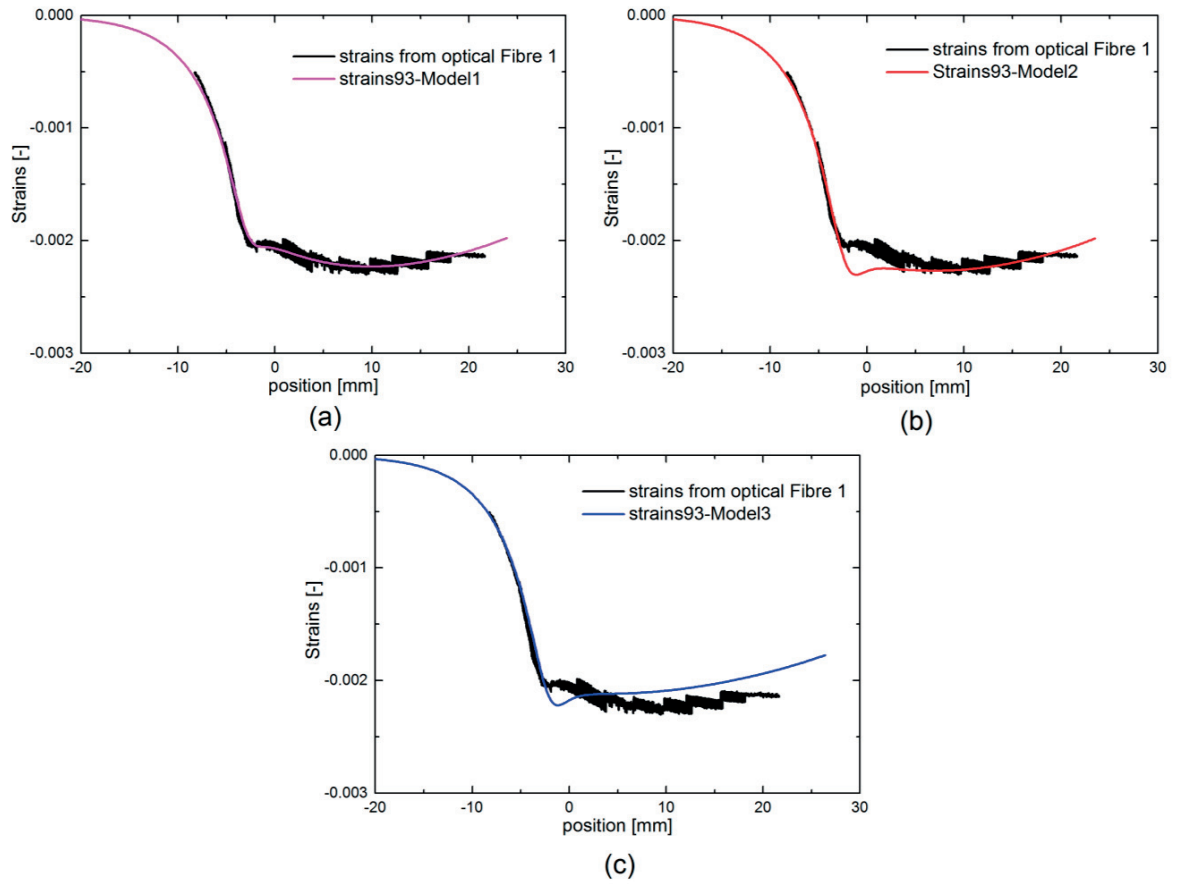
Figure 3.45: Experimental strain data from FBG sensors inscribed in optical fibre 1 and the predicted strain distributions from (a): Model 1 ; (b): Model 2 ; and (c): Model 3.
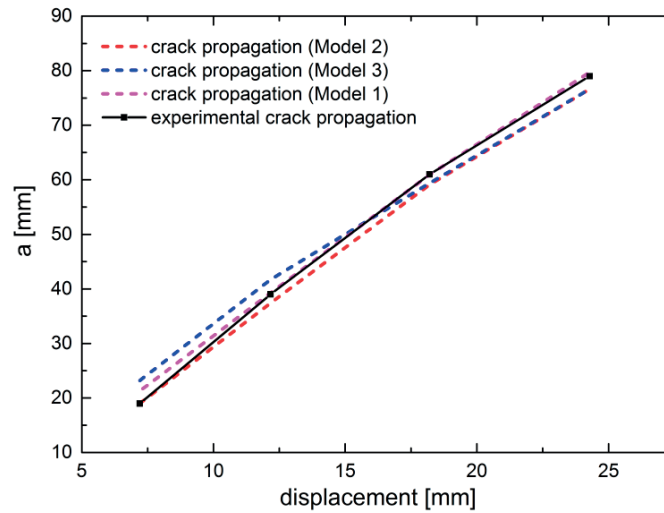
Figure 3.46: Experimental and numerically predicted crack propagation at 4 different stages of the delamination .

44

Summary

A unidirectional carbon epoxy composite DCB2-P1-B specimen is delaminated under mode I with a strain monitoring by means of 2 optical fibres with FBG sensors. The first optical fibre is placed in the transition state, where fibre bridging is not fully developed and the second optical fibre in the region where steady state is reached. Using an inverse procedure based on the strains profile measured by the second optical fibre, 3 traction-separation relations are identified at steady state, and corresponding FE models with cohesive elements are constructed to predict the loading response of the specimen. The predicted load-displacement curve was found to match well with the experimental data for crack extensions larger than 35 mm but significant deviation was observed for shorter crack extensions. Results show that the obtained models are able to predict the crack length with a good accuracy. Moreover, for an intermediate crack extension of 25 mm, the axial strain distribution is very well predicted by the model obtained from the optimization with a weight of zero for $G_{I,i}$, which validates the use of a single cohesive traction separation relationship to predict both the local strain and load-displacement for intermediate to large crack lengths.

45

3.2 Delamination behavior of DCB2-P1-B specimens

In the case of symmetric DCB specimens tested under mode I delamination, the extent of large scale bridging is influenced by the specimen's thickness [21]. Indeed the ERR at steady state increases with thickness since the decay rate of bridging tractions depends on the specimen's curvature in the bridging zone. In the case of Asymmetric DCB specimens the moment of inertia of the upper beam will be different from the lower beams' one, hence the delamination behavior could be affected. In this chapter asymmetric DCB specimens with the crack initiator positioned 2 plies from the midplane are subjected to mode I monotonic delamination test to characterize the effect of a moderate asymmetry on the bridging tractions.

3.2.1 Delamination tests

Asymmetric DCB2-P1-B specimens with a nominal thickness of 6mm are fabricated by hand-lay-up following the manufacturing procedure described in Chapter 2. Five specimens are tested under mode I delamination, using an Instron 5848 machine with a 2kN load cell. The Compliance Calibration method (CC) is used for data reduction to enable comparison with the scaling function established in the literature [21].
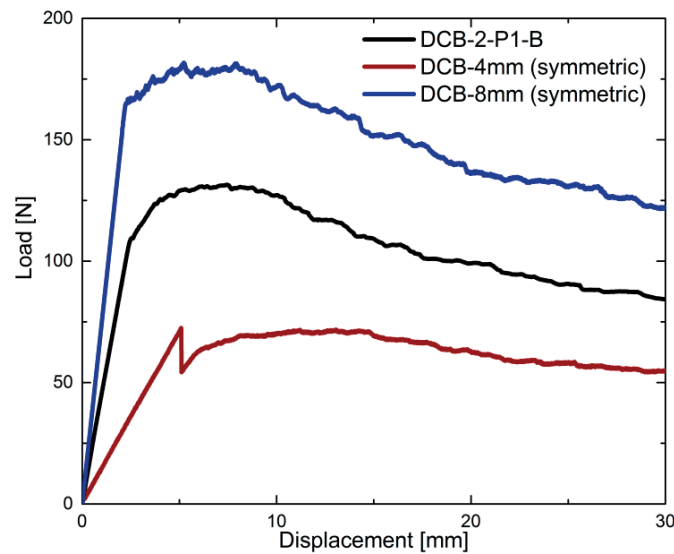
Figure 3.47: Experimental load displacement curves obtained from symmetric [21] and asymmetric DCB specimens of different thicknesses.

Representative load displacement curve (see Figure 3.47) and ERR curve (see Figure 3.48) of a DCB2-P1-B are compared with the ones of symmetric DCB specimens from the same material with different thicknesses. Note that only 4mm- and 8mm-thick symmetric DCB specimens are available in the reference work [21] hence the comparison with data from asymmetric 6mm-thick DCB specimens is firstly qualitative. Both load displacement and ERR curves show a thickness effect comparable to what is reported in the literature: data are positioned in an intermediary level between 4mm- and

8mm-thick DCB specimens. The ERR at initiation is the same for all specimens: ~300 J/m^2, while the plateau level increases with specimens' thickness, hence the asymmetric specimens appear to fit into the thickness scaling effect reported for the symmetric ones.
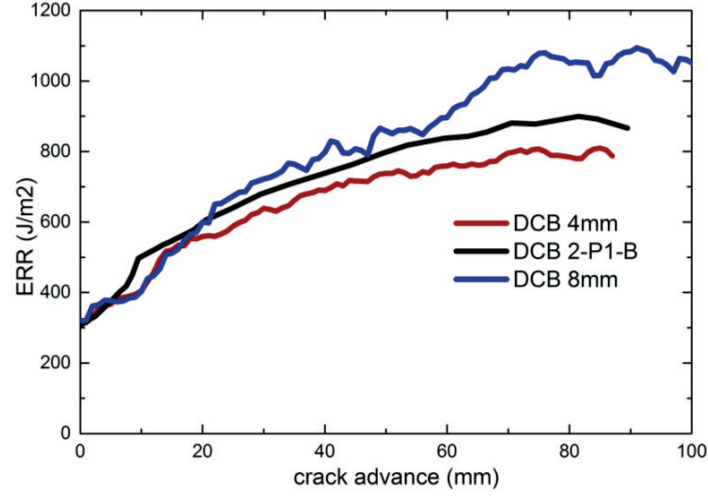
Figure 3.48: ERR curves (CC method) obtained from symmetric [21] and asymmetric DCB specimens of different thicknesses.

3.2.2 Assessment of the thickness scaling effect

In order to determine if asymmetric DCB2-P1-B specimens incur the same scale effect as symmetric DCB specimens, the thickness scaling function of the ERR at steady state G_{ss} available in the literature [21] for symmetric specimens must be adapted to account for the different thicknesses of the upper beam and the lower beam.

Considering the double cantilever beam specimen as 2 clamped beams with different thicknesses h_i, E_i modulus, and quadratic momentum I_i (see Figure 3.49), according to simple beam theory [52] the vertical displacement of one beam is:

$$\delta_i = \frac{P}{E_i I_i} \left(-\frac{x^3}{6} + a\frac{x^2}{2} \right) \tag{3.3}$$

with $I_i = \frac{Bh_i^3}{12}$ (3.4)

For a lever arm $x = a$:

$$\delta_i = \frac{Pa^3}{3E_i I_i} = \frac{4Pa^3}{E_i Bh_i^3} \tag{3.5}$$

47

The compliance of each beam made of the same material ($E_1 = E_2 = E$) is:

$$C_i = \frac{4a^3}{EBh_i^3}$$

(3.6)

To calculate the global compliance of the system C_{total} (including both beams with $h_1 \neq h_2$), the total displacement $\delta_{total} = \delta_1 + \delta_2$ must be considered:

$$C_{total} = \frac{\delta_{total}}{P} = \frac{a^3}{3}\left(\frac{1}{EI_1} + \frac{1}{EI_2}\right) = \frac{a^3}{3}\left(\frac{12}{EBh_1^3} + \frac{12}{EBh_2^3}\right)$$

(3.7)

Hence the compliance of a 6mm-thick DCB2-P1-B is different from a 6mm-thick symmetric DCB specimen. To take this into account, an equivalent EI_{eq} is calculated for each system as follows:

$$EI_{eq} = \frac{1}{\left(\dfrac{1}{EI_1} + \dfrac{1}{EI_2}\right)}$$

(3.8)
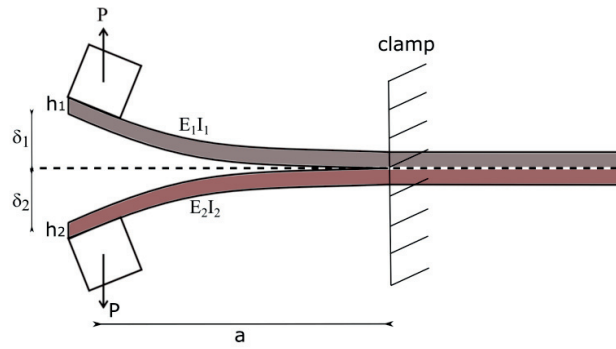
Figure 3.49: Schema representing a double cantilever beam as 2 clamped beams with a lever of length a.

For each symmetric DCB specimen (from h =4 to 10 mm), the EI_{eq} is calculated in order to convert the scale function $G_{ss} = f(h)$ established by Farman-Ashtiani *et al.* [21] to $G_{ss} = f(EI_{eq})$ to account for the different compliances of symmetric and asymmetric specimens. Using a cubic fit of the modified scale function, the obtained values are shown as a continuous function in Figure 3.50-a.

Figure 3.50-b shows that because of the difference in total compliance between the symmetric and asymmetric 6mm-thick specimens, the expected ERR values are not exactly the same. Nevertheless, it should be noted that the reported difference (~25J/m²) is smaller than the typical experimental scatter. It can be concluded that the position of the initial crack starter does not influence the delamination behavior for an offset $\leq$ 0.4mm (with respect to the middle plane), which corresponds to 2 plies. It should also be noted that the experimental G_{ss} for DCB2-P1-B specimens is in excellent agreement with the predicted value (see Figure 3.50) from the scaling function expressed in terms of EI.
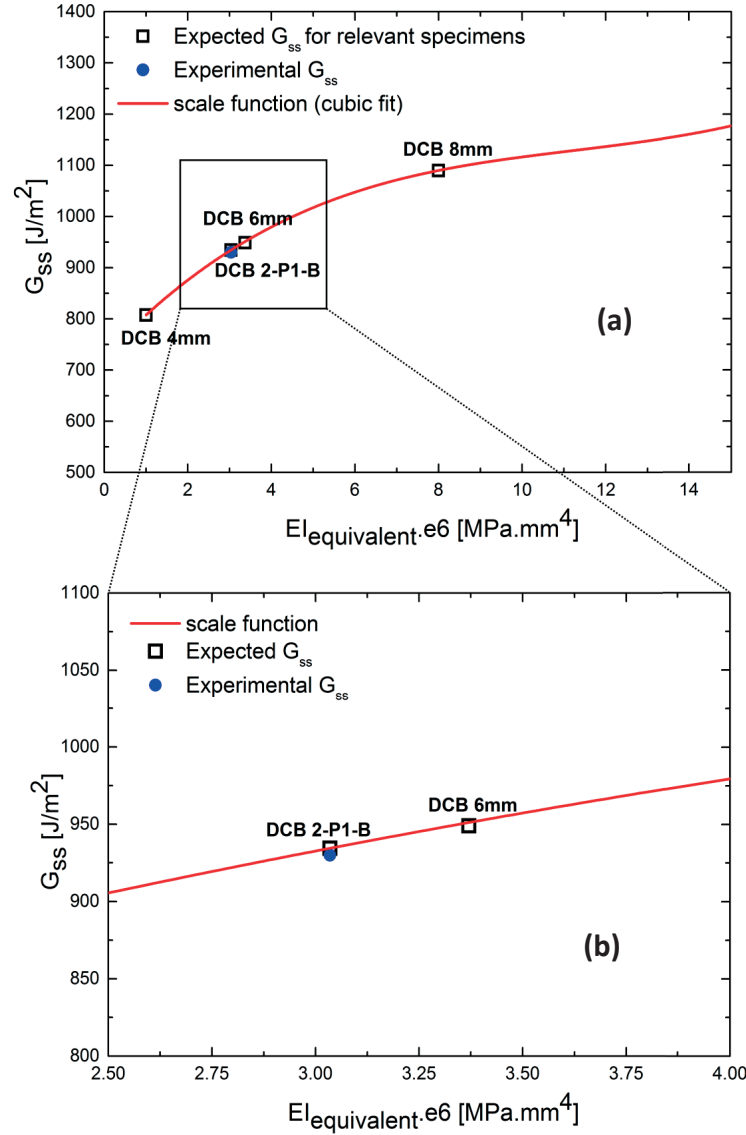
Figure 3.50: Steady state Energy release Rate G_{ss} scale function adapted from [21] as a function of the equivalent EI_{eq}. (a) is the global view and (b) zoom in the region of interest to compare asymmetric DCB2-P1-B with symmetric DCB of the same thickness. The asymmetric specimens' configuration shows an excellent match with the original scaling relation.

3.2.3 Parametric FE Modelling

In this section the objective is to use the inverse identification procedure described in section 2.10.3 to evaluate the traction separation relation representing the delamination behavior of 6mm-thick DCB2-P1-B specimens. Two different numerical models are employed: in the first model, the DCB2-P1-B specimen is simulated and tractions are applied on both crack surfaces to account for fibre bridging (identification model), while the second model contains a cohesive elements layer that connects the arms of the specimen to simulate crack propagation (prediction model). Thanks to the latter FE model, the identified bridging law can be checked with respect to independent experimental test data.

Identifications of the bridging tractions

Since it has been demonstrated in section 4.2 that the thickness scaling established by Farmand-Ashtiani *et al.,* is valid for the considered DCB2-P1-B specimens, the parameters needed to identify the traction separation function representing the fibre bridging (namely the maximum bridging tractions σ_{max}, the decay rate of the tractions along bridging zone γ, and the maximum bridging length z_{max}) should correspond to the ones predicted by the scaling function of identified parameters (see Figure 3.51).

Consequently, no strain monitoring with FBG sensors are used in this section for the inverse bridging tractions identification procedure: a first guess of the triplets of parameters (σ_{max}, γ, z_{max}) is estimated as (1.38 [MPa], 0.08 [mm^{-1}], 53 [mm]) using the scaling function proposed by [21] (see Figure 3.51). Then, these parameters are used to model the bridging traction distribution in a 2D model built with the geometry taken from the experiment (initial crack length=55mm) for identification purposes.
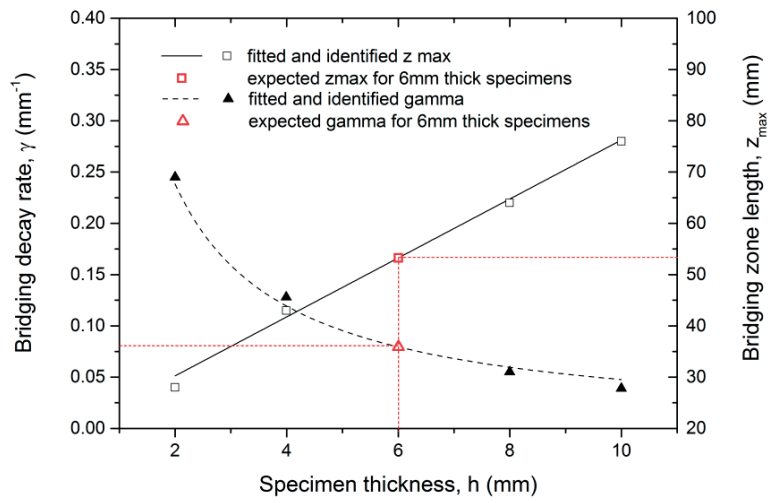
Figure 3.51: Evolution of bridging zone z$_{max}$, rate of tractions decay γ by specimen thickness scaling [21]. The expected values of the parameters for a 6mm-thick specimen are the red symbols.

A total of 128000 quadratic plain strain elements with reduced integration (Abaqus CPE8R) are used for meshing the model. Elements are collapsed at the crack tip and their mid-nodes are shifted to ¼ of the edge to create a $1/\sqrt{r}$ singularity (*r* being the distance from the crack tip). Both arms of the specimens are simulated, since the asymmetry does not allow for simplification. Surface tractions are applied between the crack tip and the end of the Teflon insert. The Crack Opening Displacements (CODs), $\delta(z)$ extracted from the numerical model, are then combined with the bridging tractions $\sigma_b(z)$ to obtain the traction-separation model $\hat{\sigma}_b(\delta)$. The contribution of bridging $G_{I,b}$ to the total ERR, G_{total} is calculated using equation 2.16 and is iteratively compared to the experimental values obtained by compliance calibration to improve the parameter estimates.

In this particular case, σ_{max} is considered constant at 1.38 MPa [21, 42] as it has been observed to be independent of specimen geometry. To determine the geometry dependent parameter z_{max}, the experimental crack length is plotted as a function of the applied displacement to determine the onset of steady state propagation corresponding to a fully developed bridging zone. When the curve

becomes linear; the steady state is considered to be reached and the crack length corresponds to the fully developed bridging zone length. As shown in Figure 3.52, z_{max} is estimated equal to 60 mm.
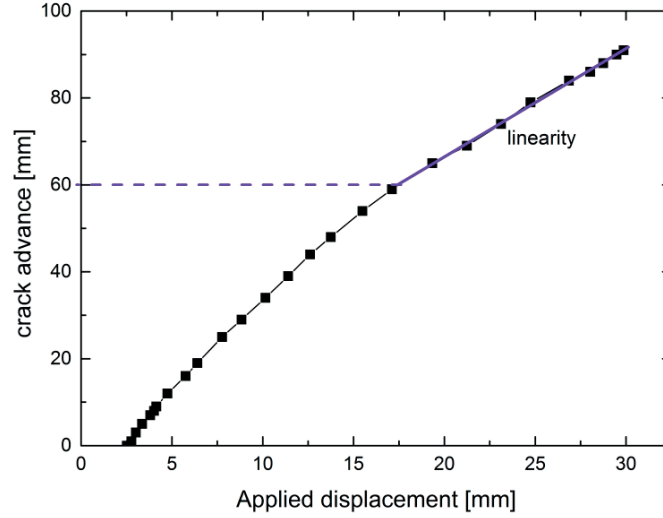
Figure 3.52: Experimental crack growth as a function of applied displacement for a DCB2-P1-B specimen. The curve becomes linear at Δa=60mm.

Finally, the second geometry dependent parameter γ is identified so that the numerical integration of the traction-separation $G_{I,b} = \int_0^{\delta_{max}} \hat{\sigma}_b(\delta) d\delta$ corresponds to the experimental contribution of bridging $G_{I,b}$ = 590 J/m^2 (see Figure 3.53). After a few iterations with the FE model, required to update the COD profile, the estimated value of γ = 0.1 mm^{-1} is obtained.

As a result, the identified triplet of parameters for a DCB2-P1-B specimen is (1.38 [MPa], 0.095 [mm^{-1}], 60 [mm]). While γ is consistent with the scale function predictions, the maximum bridging length z_{max} is slightly offset from the extrapolated value (60mm instead of 53). This difference remains however well within the experimental uncertainties and thus is considered non determinant. Indeed, a precise determination of the steady state region is very difficult to achieve because of the scatter of the experimental data and a general uncertainty of about +/-5 mm (at least) can be expected.

Cohesive law

Then, the identified bridging parameters are used to develop a cohesive law for crack propagation simulation. The initial part of the cohesive law is determined so that the fracture toughness at initiation $G_{I,C}$ is equal to the experimentally determined value of 291 J/m^2 (see Figure 3.53). The critical stress level σ_C is identified at 23MPa, as in [42] and [50] for the same composite material; this value corresponds to the yield point of the composite in transverse tension. The initial cohesive stiffness K_p is taken equal to 12 500 MPa.mm^{-1}, so that the stiffness of the cohesive elements is high enough not to influence the resulting load displacement curve while ensuring convergence of the model (convergence study). With these assumptions, the damage initiates at elastic opening of only 3 μm corresponding to 13% of the opening δ_b = 24 μm occurring at the end of the initial part of the cohesive law.

The identified bridging law from the previous section $\hat{\sigma}_b(\delta)$ is appended to the second part of the curve (see Figure 3.53) to take into account the effect of bridging on the cohesive elements behavior. The area under the obtained traction separation relation is equal to the ERR at steady state $G_{ss} = G_{I,i} + G_{I,b}$.
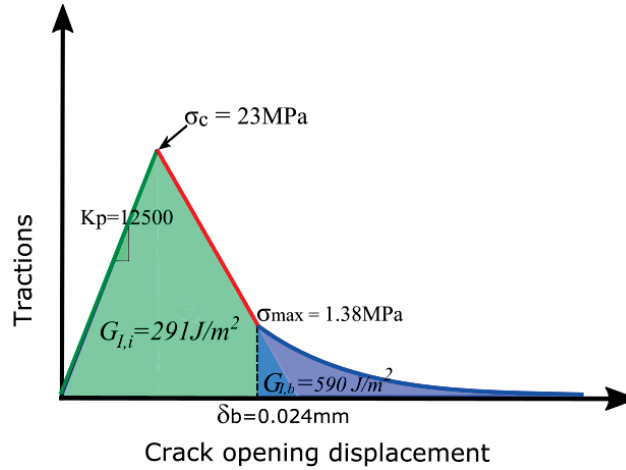
Figure 3.53: Identified cohesive law for DCB2-P1-B specimens.

The resulting cohesive law (see Figure 3.53) is implemented in 2D-cohesive elements through a tabular multi-linear damage evolution function (as described in section 3.10.3) in Abaqus®. The simulation model is used to predict the experimental load-displacement curve and crack length, and hence is compared with experimental data. Both arms of the DCB2-P1-B are modelled, and discretized with 29400 quadratic plane strain (CPE8R) elements for the upper arm and 36000 for the lower arm, since the thickness of the beams is different. A 20 μm-thick layer of 6480 linear cohesive elements (COH2D4) is tied to the two arms along the delamination path, i.e. from the initial crack length to the end of the specimen. The simulation is run with a displacement control until 19.3 mm opening.
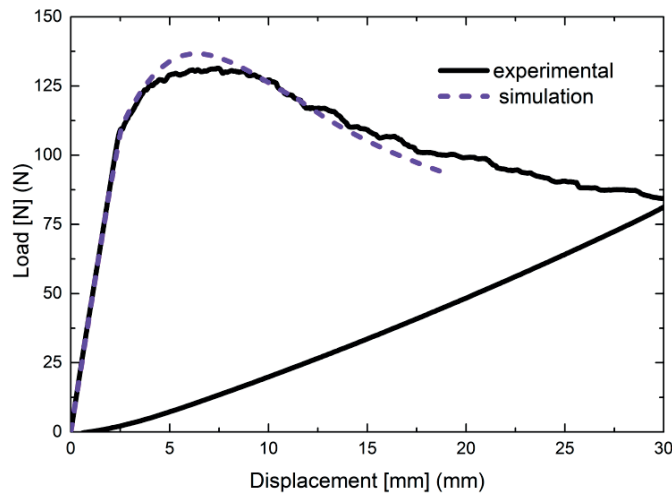
Figure 3.54: Experimental and numerically obtained load displacement curves for a DCB2-P1-B specimen.

The obtained load displacement curve (see Figure 3.54) is in very good agreement with the experimental one, which independently validates the identified cohesive law. In particular, the initiation is well captured, and the overshoot in the raising part of the curve that is regularly encountered using this procedure, is satisfactorily low.

Summary

Mode I delamination of DCB2-P1-B specimens is analysed and compared with symmetric DCB specimens of the same thickness. Experimental results show that the fracture toughness at initiation is not affected by the asymmetry, and its value is found consistent with the literature [21] for the same material. Moreover, the measured steady state ERR of 6mm-thick asymmetric specimens is in good qualitative agreement with the scaling reported previously. This observation reinforces the evidence that the initiation fracture toughness of the composite is actually geometry independent but the bridging contribution is not. An analysis based on the thickness scaling function established by Farman-Ashtiani *et al*. [21] for the same material under the same testing conditions, shows that the difference of thickness between the two beams of a DCB2-P1-B specimen only slightly affects the ERR at steady state compared to a symmetric specimen of the same thickness. This difference is smaller than experimental scatter and can be considered insignificant.

An inverse identification procedure using a parametric FE model and cohesive element simulation is performed to evaluate the traction separation relation describing the delamination behavior of a DCB2-P1-B specimen. The obtained results agree well with experimental data. The identified parameters of the bridging tractions relation are consistent with the values predicted by the thickness scaling function.

It can be concluded from this combined experimental-numerical work that the effect of asymmetry induced by a crack propagation two plies above the central line of a 6mm DCB does not significantly affect the initiation and fibre bridging development during crack propagation in bulk UD composites.

This preliminary study also implies that the mode II component induced by the asymmetry of the specimens is probably negligible since even a small mode II contribution has been shown to drastically reduce the bridging tractions [49]. This hypothesis is experimentally and numerically investigated in details in chapters 4 and 5, respectively.

4. Experimental Results

4.1 Asymmetric DCB specimens bonded with Resoltech 3350-3358T (A1)

As shown in previous chapters, a moderate asymmetry does not significantly influence the delamination behavior of a DCB specimen made of bulk composite. In the case of a bonded repair in an aeronautic structure where the transverse strength and toughness of the adhesive is greater than that of the composite, damage can occur in the composite close to the adhesive layer, leading to interlaminar fracture. The proximity of a relatively compliant glue to the damage process zone might affect the fracture properties of the composite, rendering failure predictions more difficult which could lead to a premature catastrophic failure if not anticipated correctly.

In this chapter the effect of an adhesive layer in the surrounding of a delamination crack plane in unidirectional CFRP laminates is investigated. The delamination behavior of bonded joints in terms of R-curve is compared with the one of bulk composite specimens. Besides, the effect of the postcuring process that bonded joint specimens incur to cure the adhesive is evaluated: bulk specimens (DCB2-P1-B) are submitted to the same thermal cycle prior to mode I delamination tests, and compared with as manufactured bulk specimens. To determine if a smaller asymmetry in the joint specimens influences the results, a configuration with a smaller offset of the crack plane with respect to the adhesive (DCB1-P1-A1) is compared with the reference (DCB2-P1-A1).

4.1.1 Delamination tests

A total of 6 DCB2-P1-A1 specimens are fabricated according to the procedure described in section 2.3.2, and subjected to monotonic (1 mm/min) mode I loading in displacement control, following the protocol of the ASTM standard D5528-03 (see section 2.51 for more details). Typical load-displacement curves from DCB2-P1-B and DCB2-P1-A1 are shown in Figure 4.55.
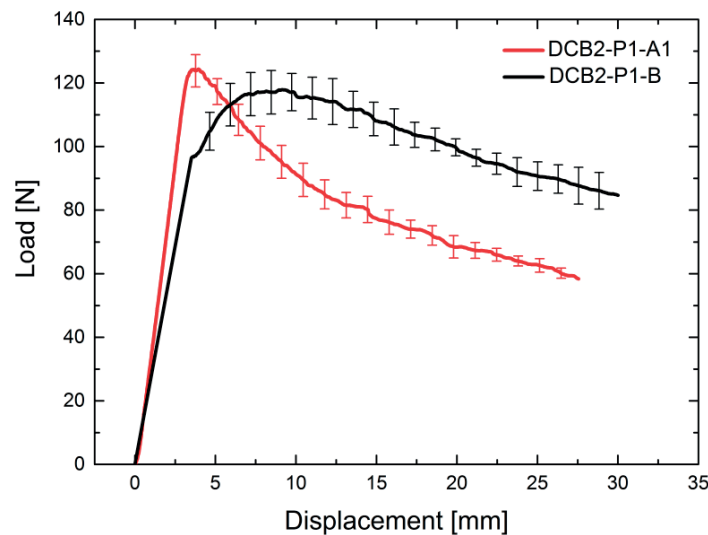
Figure 4.55: Comparison of load-displacement curves of DCB2-P1-B (black curve) and DCB2-P1-A1 (red curve).

For clarity of presentation, the initial jump occurring at the precrack stage to propagate the crack further the resin rich region is omitted. The difference of slopes in the linear parts is due to a small difference of initial crack length.

The significant contrast between those force-displacement curves suggest a different mechanism at initiation since the onset of non linearity, correlated to the onset of crack propagation, occurs at a higher load for the joint for a similar initial crack length. Moreover, the decrease of the load is sharper for joints than for bulk specimens, indicating a lower extent of fibre bridging, corresponding to a lower G_{ss} for joints compared to bulk specimens.
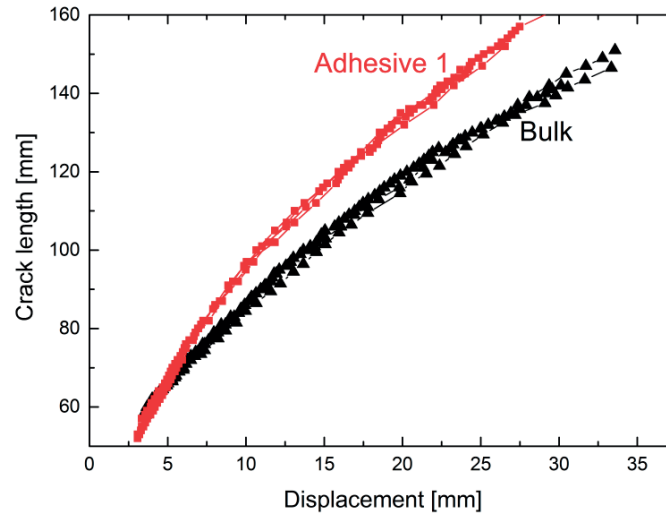
Figure 4.56: Crack growth as a function of applied displacement for DCB2-P1-A1 (red curves) and DCB2-P1-B (black curves).

Indeed crack propagation for a given applied displacement is larger in adhesively bonded specimens than in bulk laminates as shown in Figure 4.56.
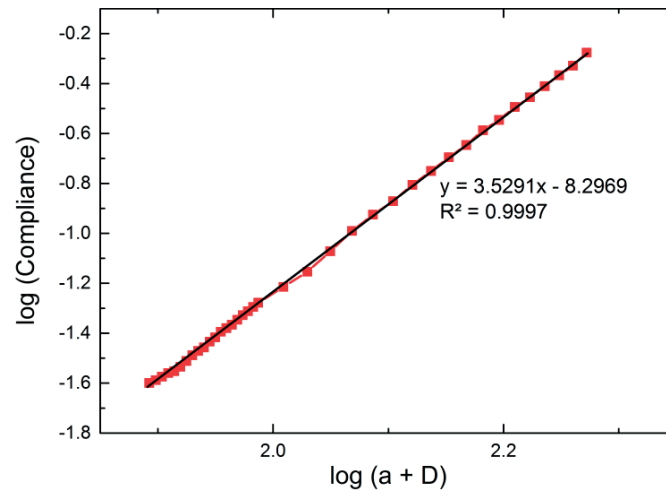
Figure 4.57: Fit of the compliance as a function of modified crack length in log scale. The quality of the fit is excellent at both initiation and propagation.

57

In order to compute the ERR, the MCCM is employed (see section 2.8) to obtain an excellent fit of the compliance as shown in Figure 4.57.

The calculated R-curves for each configuration are shown in Figure 4.58 in which the curve corresponds to the mean value of the batch and error bars represent the standard deviation) for the batch. As suggested from the load displacement curves comparison, the observed fracture toughness at initiation is influenced by the presence of the adhesive layer: $G_{I,i}$ = 270 J/m^2 for DCB2-P1-B while $G_{I,i}$ = 350 J/m^2 for joints. This difference of 80 J/m^2 at initiation might suggest a different failure mechanism in the process zone at the interface matrix/fibre level.
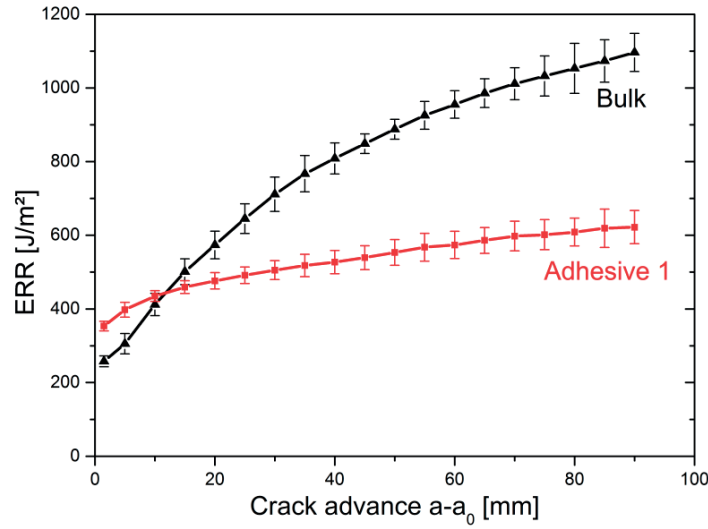
Figure 4.58: Average R-curves for DCB2-P1-B and DCB2-P1-A1 specimens (MCCM).

To verify this hypothesis, observations with both an optical microscope (magnification x20, see Figure 4.59) and an SEM (magnification x650, see Figure 4.60) have been performed on the fracture surface of both types of specimens. The observed damage close to the crack initiation area clearly show that the failure mechanism is different: in the case of bulk composite specimens the crack propagation leaves most of the fibres clean of matrix, indicating a failure occurring mostly at the interface matrix/fibre, whereas the fibres seem to be covered with resin for joint specimens, indicating a matrix failure probably occurring at the resin rich region. Therefore the differences of $G_{I,i}$ between bulk and joints are mostly attributed to material heterogeneities at the crack starter. Those heterogeneities are potentially influenced by the manufacturing process and the distribution of matrix rich regions generated in the vicinity of the mold surface and release film. Those effects might not be representative of other configurations or production methods.

The initiation is followed by a typical R-curve behavior for the bulk specimens, whereas the ERR value for joint specimens increases much less. Indeed the ERR at steady state G_{ss} calculated with MCCM for the joint specimens is 650 J/m^2 whereas the ERR of the bulk specimens is about 1000 J/m^2. This very significant difference of ~350 J/m^2 (35%) denotes a radically different development of the bridging in the presence of an adhesive layer.
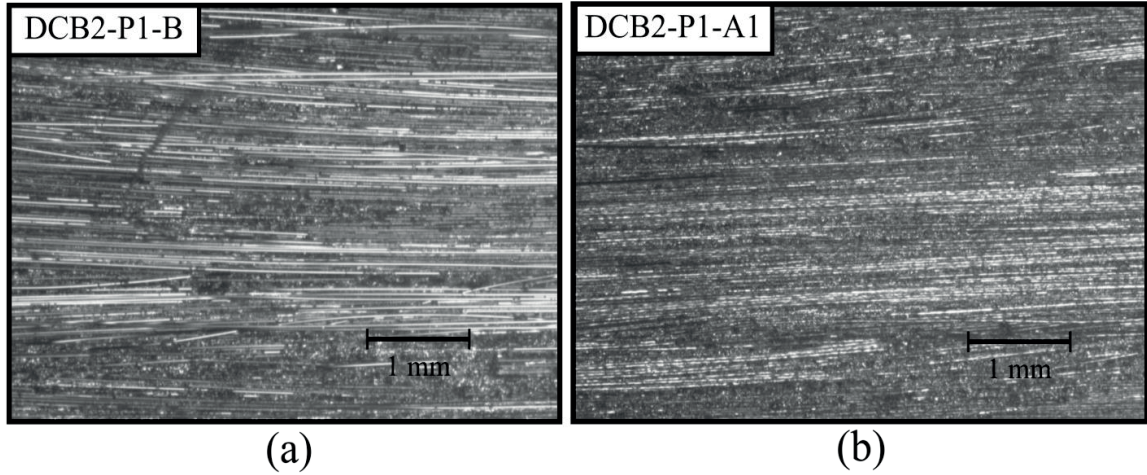
Figure 4.59: Optical Microscope fractographs of (a) DCB2-P1-B specimen and (b) DCB2-P1-A1 specimen. Both pictures are taken within the initiation area. The fibres appear shiny and clean of epoxy matrix in the bulk specimen, whereas in the bonded joint specimen, fibres seem to be covered with resin.
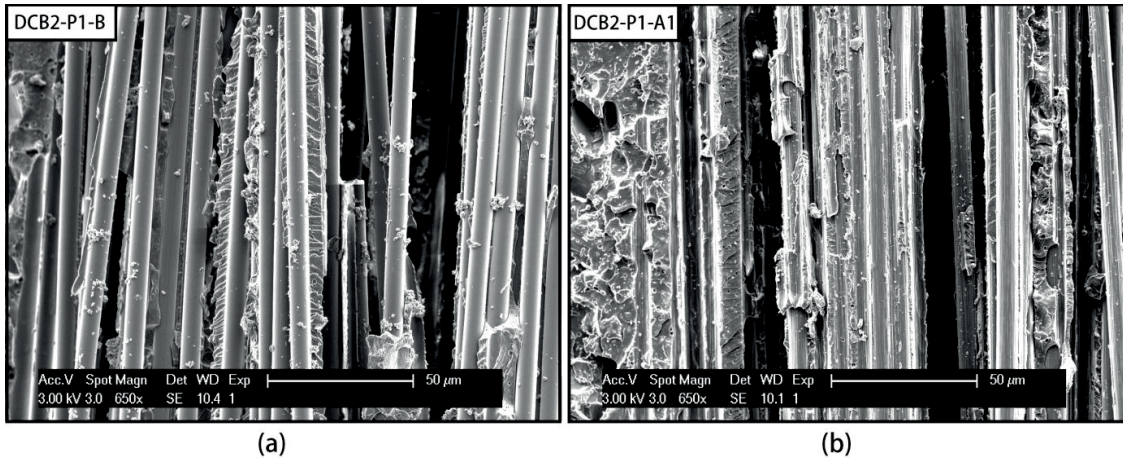
Figure 4.60: SEM Fractographs of (a) DCB2-P1-B specimen and (b) DCB2-P1-A1 specimen. Both pictures are taken within the initiation area. The fibres are clean of matrix in the bulk specimen, contrary to the bonded joint specimen, where there is matrix failure as well as fibre/matrix interface failure. Those pictures are representative of the whole fractured surface.

Such a difference can be caused by either a significant reduction of the number or size of bridging fibre bundle [43,45] or by a significant reduction of their bridging efficiency (loading angle). To evaluate those effects, representative microsections (see Figure 4.61) of DCB2-P1-B and DCB2-P1-A1 specimens are taken at a distance of 7mm from crack tip corresponding to a fully developed bridging zone. These observations show that when an adhesive layer is present, only isolated fibres or small clusters of fibres are involved in the fibre bridging, while many substantial bundles of fibres connect the two arms in the case of bulk composite specimens. As shown in [45], bundles of fibres are associated to a more intense energy dissipation required to break the bridging ligaments, leading to a very different R-curve behavior and G_{ss} values.

Overall, those experimental results show that the mechanisms involved in the fibre bridging are heavily influenced by the presence of the joint as all other parameters are the same in both experiments. Hence, it is reasonable to hypothesize that the presence of a relatively compliant adhesive layer close to the crack is the main factor responsible for the observed change of toughness properties between DCB2-P1-B and DCB2-P1-A1 specimens. More investigations are thus needed to understand how the presence of the adhesive joint interacts with the crack to lead to such a reduction of bridging development. This question is the main topic of the following chapters.
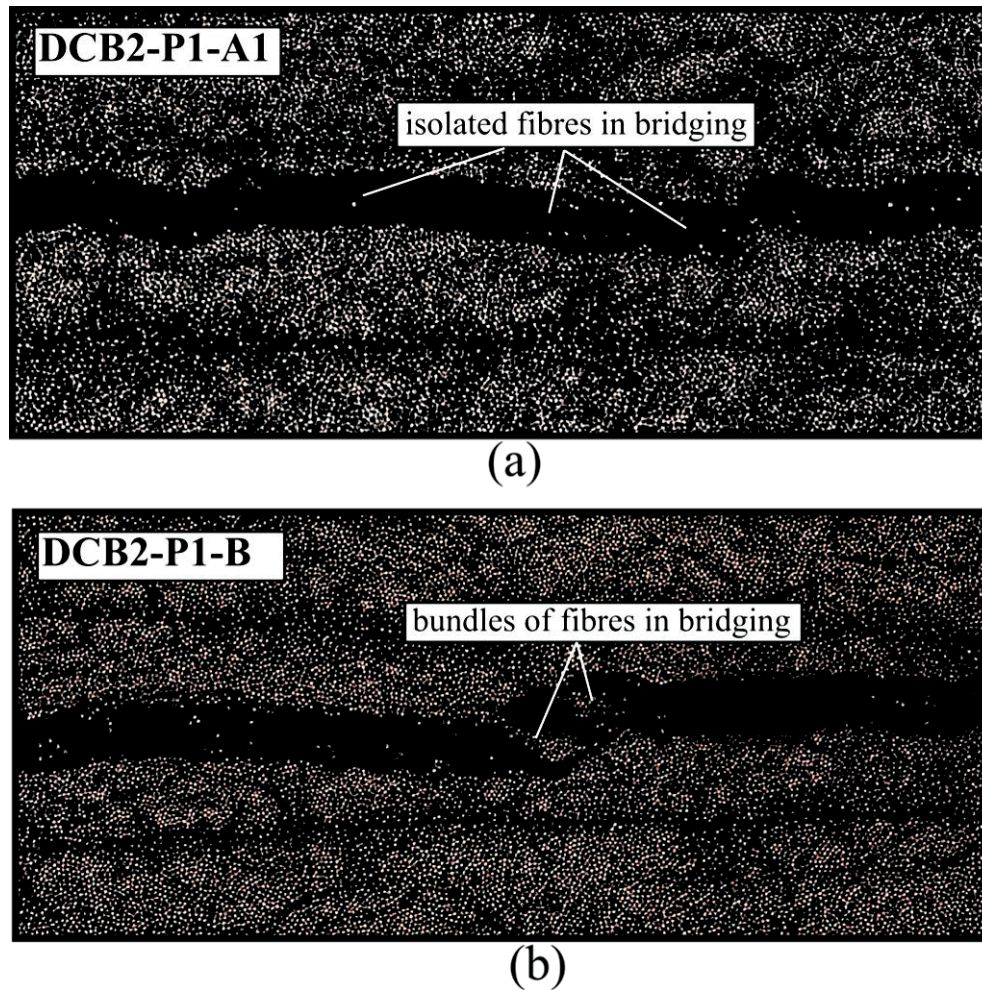
Figure 4.61: Microsections of a) DCB2-P1-A1 specimen and b) DCB2-P1-B specimen after delamination, 7mm from the crack tip

4.1.2 Characterization of the adhesive A1

As the adhesive A1 (i.e. Resoltech 3350-3358T) used in this work consists of 2 components (a resin and a hardener to be mixed together) which must be regularly replaced due to the relatively quick expiration date; each new batch of glue is characterized to ensure that the properties are kept constant from one batch to the other. Moreover, the elastoplastic behavior of the adhesive need to be characterized to perform non linear FE analysis of the crack propagation process.
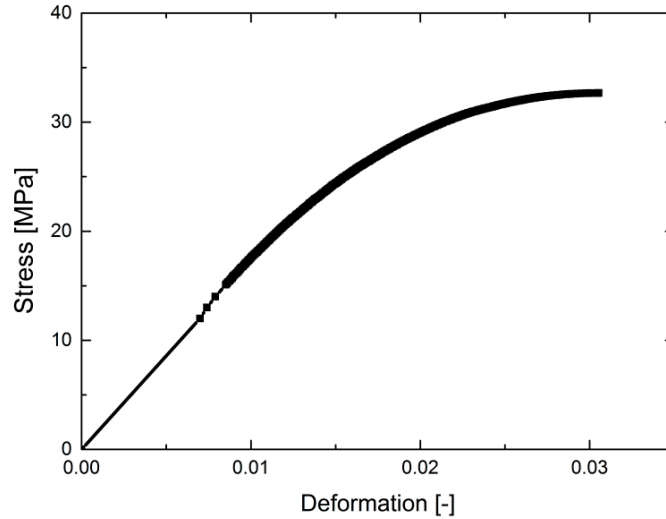
Figure 4.62: Hardening curve of adhesive A1 obtained from dogbones tests.

The fabrication and testing procedures of the samples is described in section 3.3.2. A tensile test is performed with an Instron machine on 5 dogbones specimens following the ASTM D638 standard at a rate of 1mm/min. The displacement field and strains are determined with DIC from the pictures taken at 1Hz with a high resolution CCD camera, and the load is recorded with a 2kN load cell. The mechanical properties extracted from those tests are the following:

- Young's modulus: 1.8 GPa
- Yield strength: 12 MPa

The obtained hardening curve (see Figure 4.62) of the adhesive is employed for subsequent modeling purposes.

4.1.3 Postcuring step influence

The manufacturing process of DCB2-P1-A1 specimens involves a 5h-long post-curing step in the oven at 70°C, in order to cure the adhesive. As the Bulk specimens are not subjected to this post curing cycle, the difference of delamination behavior of joints compared to bulk specimens could be attributed to this stage. Indeed the curing temperature of the adhesive A1 is just 10°C lower than the curing temperature of the prepreg system P1, and is also relatively close to the glass transition temperature T_g of the cured composite, which is around 100°C. If the initial composite is not fully cured, this could lead to a more complete polymerization of the epoxy matrix of the composite for joint specimen, inducing a different matrix cracking behavior during delamination and therefore a different bridging mechanism. Besides, this post-curing step for the composite might induce residual stress relief, possibly leading to a different fibre bridging.

To investigate this hypothesis, three DCB2-P1-B bulk specimens are fabricated and submitted to the same post-curing process as for DCB2-P1-A1 joint specimens, i.e. 5 hours at 70°C. Mode I delamination test results (calculated with MCCM) of the post-cured specimens (see Figure 4.63) are perfectly consistent with those of DCB2-P1-B specimens shown in chapter 3.
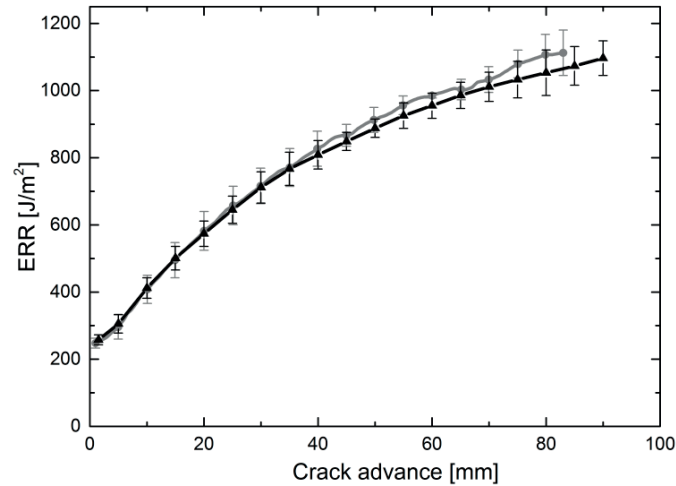
Figure 4.63: ERR curves of postcured (gray curve) and as-manufactured (black curve) DCB2-P1-B specimens.

Consequently the initial hypothesis is not maintained: the heat treatment, that DCB2-P1-A1 specimens incur in order to polymerize the adhesive layer, is not responsible of the difference observed on fibre bridging compared to bulk specimens. Moreover, DSC measurements (see Appendix 2) showed that no reaction takes place under 100°C thus showing that the composite is indeed fully cured after the autoclave production. The postcuring cycle applied to bonded joints specimens has thus no effect on the polymerization state of the composite epoxy matrix.

4.1.4 DCB1-P1-A1 delamination tests

In order to determine if the distance between the adhesive layer to the crack plane plays a role on the delamination behavior, asymmetric DCB bonded joints are manufactured with the crack starter positioned one ply above the bond layer. Indeed this decrease of asymmetry can play a role on the toughness properties as asymmetry is usually associated with increased mode mixity and bridging phenomena are known to be highly dependent on mode mixity [49].

A batch of three DCB1-P1-A1 is tested and compared with the results of DCB2-P1-A1 specimens. A small difference on the initial compliance due to a slight difference of initial crack length is observed but this is not related to a different delamination behavior [42]. The post peak response of the load displacement curves (which is representative of crack growth behavior) as well as fracture toughness at initiation and steady state are found to be nearly identical in both cases (see Figure 4.64.a and b). This consistency indicates that potential shear and mode mixity effects are either negligible or have similar effects in both DCB2 and DCB1. Thus, for sufficiently small crack plane offsets, the bridging behavior of the joint specimens is actually independent from that offset. It also shows that the DCB1-P1-A1 and DCB2-P1-A1 exhibit the same delamination behavior and can practically be reduced to a single case.
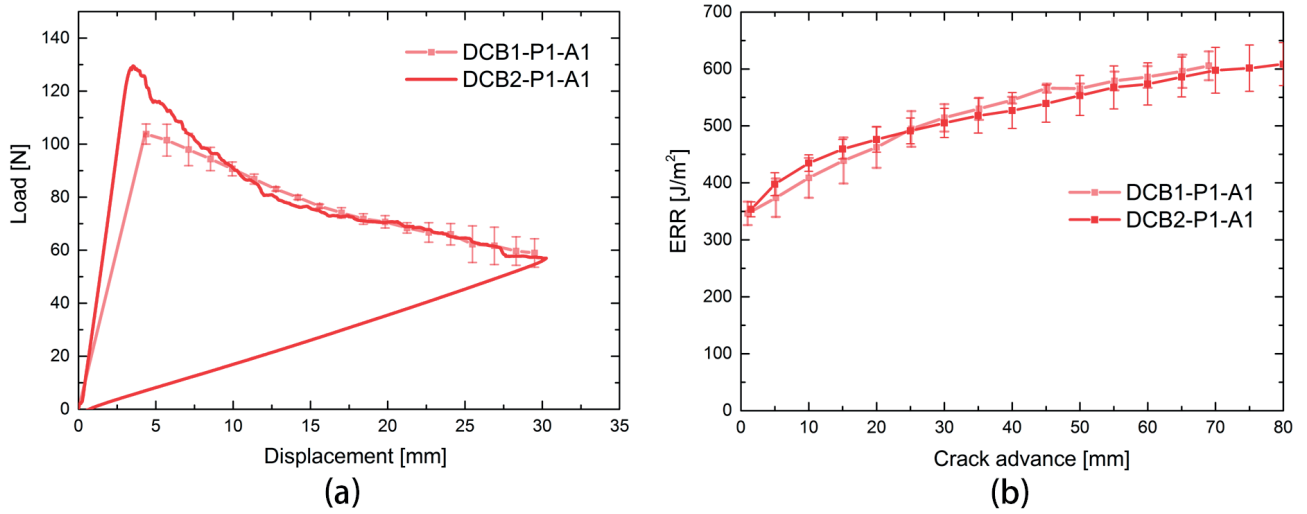
Figure 4.64: (a) Load displacement curves and (b) ERR curves from DCB2-P1-A1 specimens (red) and DCB1-P1-A1 specimens (light red).

Conclusion

The fracture behavior of asymmetric DCB unidirectional CFRP laminate is studied with and without the presence of an epoxy adhesive layer close to the crack plane. Results show that the bond layer significantly affects the steady state fracture toughness of the composite with a very significant reduction of the bridging contribution G_b. It is demonstrated that neither the crack position offset nor the postcuring step submitted to the specimens for polymerizing the adhesive are responsible for the observed decrease of ERR in the bonded joints. Transversal sections of the specimens are observed with an optical microscope and show that the fibre bridging is composed of relatively large bundles of fibres in the case of bulk composite specimens, while mostly small bundles and isolated fibres connect the two arms of bonded joints. As fibre bundles require more energy to break than isolated fibres [45], it is ascertained that the difference of type and magnitude of fibre bridging mechanisms is responsible for the observed change of the overall fracture behavior.

4.2 Asymmetric DCB specimens bonded with Gurit SA80 (A2)

The influence of an adhesive layer in the neighbourhood of the crack tip on the interlaminar delamination behavior of asymmetric DCB specimens has been assessed with the bi-component epoxy system Resoltech 3350-3358T which is applied as a paste and forms a thin adhesive layer of about 100 μm. In this chapter, the objective is to investigate if another epoxy adhesive system with vastly different characteristics has the same effect. Therefore the same experiments as in chapter 4.1 are performed, using the toughened epoxy adhesive film Gurit® SA80 (A2) instead of Resoltech® 3350-3358T (A1). In contrast to the fluid Resoltech adhesive, the Gurit SA80 adhesive comes in the form of a solid film with a light glass fibre carrier which results in much thicker adhesive layers (~400 μm) after curing due to the higher resin viscosity and the spacing imposed by the glass fiber carrier. Additionally, the potential presence of shear in mode I delamination of DCB2-P1-B and DCB2-P1-A2 specimens is investigated by means of DIC measurements. Indeed even a moderate mode II component in a mixed mode delamination has a considerable impact on the fibre bridging: the pull out fibres submitted to shear break and do not participate to the fracture toughness of the composite [49].

4.2.1 Delamination tests

Four DCB2-P1-A2 specimens are manufactured following the procedure described in section 2.3.3. Among those 4 specimens, two are tested with an Instron 5848 machine with a 2kN load cell, and two with a hydraulic Instron® test machine equipped with a 500 N load cell. Delamination tests are conducted in displacement control at 1mm/min.
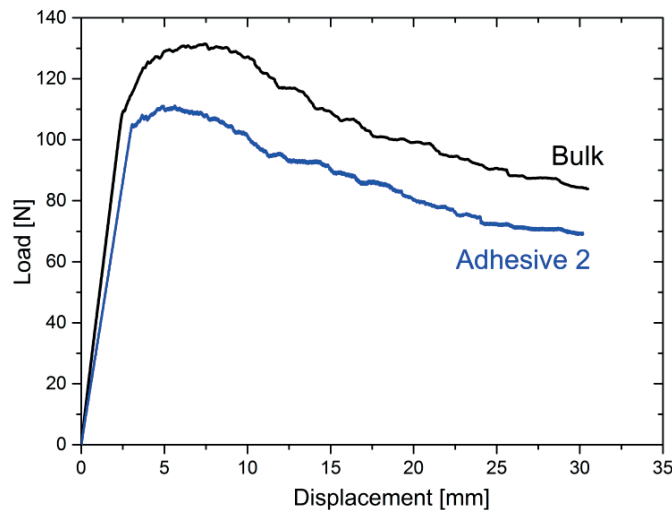
Figure 4.65: Comparison of load-displacement curves from DCB2-P1-B (black curve) and DCB2-P1-A2 (blue curve).

Typical load-displacement curves from DCB2-P1-B and DCB2-P1-A2 are shown in Figure 4.65. The unloading parts are not displayed for clarity. The different slopes observed in the linear part are not

material related but are due to the difference of initial crack length (after initial pop-in). However, the raising part taking place right after the non linearity point (onset of crack propagation), is much lower for bonded joints than for bulk specimens, which reflects a potentially lower level of fibre bridging in comparison with bulk specimens.

The fitting of the compliance with a modified power law (see eq. 2.9) during delamination test of a representative DCB2-P1-A2 specimen is shown in Figure 4.66. Overall, a very good fit quality is obtained for the whole range of crack length with this method. As described in section 2.8, for each specimen, the slope of this fit is used to calculate the ERR using the MCCM.
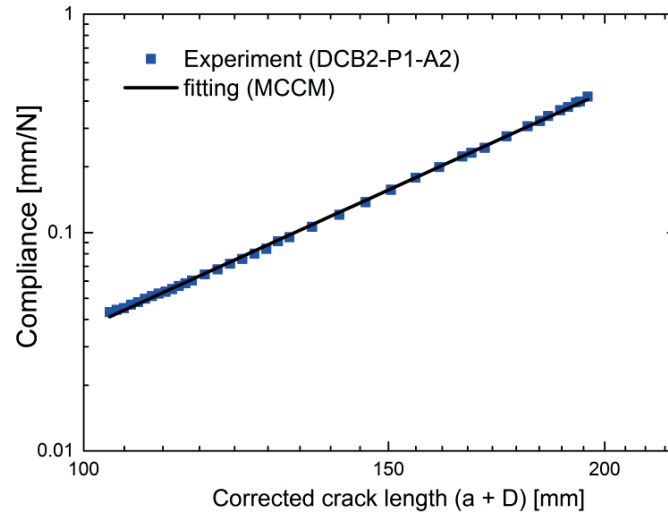
Figure 4.66: Compliance curve as a function of corrected measured crack length in log scale.

The R-curve of each specimen is computed independently using the MCCM method. The average R-curves and standard deviation from DCB2-P1-A2 tests are displayed in Figure 4.67.
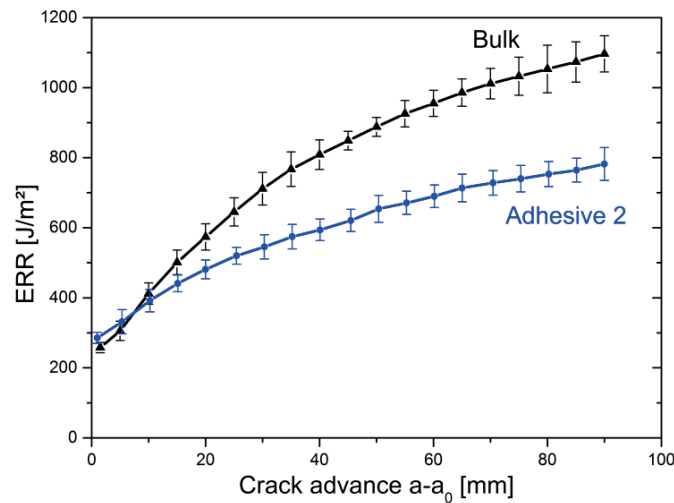
Figure 4.67: ERR curves from DCB2-P1-B (black curve) and DCB2-P1-A2 (blue curve) calculated with the MCCM.

The average R-curve of DCB2-P1-B is also shown for comparison. It can be observed that the values of G_{ss} differ significantly: more than 1000 J/m² for DCB2-P1-B and 700 J/m² for DCB2-P1-A2. Since the fracture toughness at initiation is similar for both types of specimens, the difference of G_{ss} values is directly related to a change in the bridging contribution G_b of -300 J/m² (-43%). Although the underlying mechanism is not identified yet, this very significant difference can be attributed to the presence of the adhesive layer that reduces significantly the intensity of bridging mechanisms.

This result is consistent with those obtained with the other type of adhesive in DCB2-P1-A1 series. Therefore it can be concluded that a layer of both epoxy adhesives A1 or A2, which have different composition and thickness, located near the crack plane have a strong influence on the interlaminar delamination of the UD composite.

4.2.2 Characterization of the adhesive film Gurit SA80 (A2)

The adhesive A2 is characterised in shear with Single Lap Shear (SLS) tests, following the procedure described in section 2.3.3. Dogbones tests are found not representative for this adhesive since the tensile test results mostly correspond to the behavior of the glass carrier under tension. When used as an adhesive, the glue film mostly deforms in shear or in transverse normal direction. These deformation modes are not significantly affected by the carrier fibres. Thus, in-plane tensile tests conditions are very different from those where the adhesive film is confined between two CFRP plates and submitted to mode I delamination. Consequently only SLS tests results are considered to obtain the hardening curve of the adhesive A2.

The obtained mechanical properties (see Figure 4.68) from those tests are the following (the material behavior is considered isotropic and obeying a Von Mises yield criterion):
- Young's modulus: 2.2 GPa
- Poisson ratio: 0.35
- Yield strength (Von Mises criterion): 25MPa
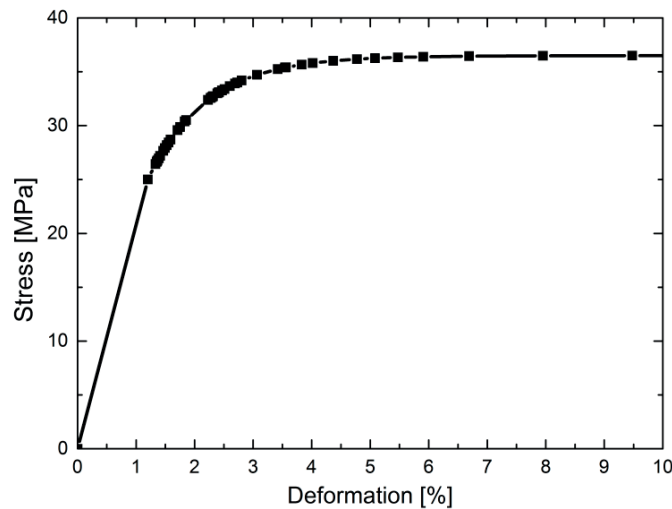
Figure 4.68: Stress-strains curve of adhesive A2 obtained from Single Lap Shear (SLS) tests.

4.2.3 Mode mixity determined with DIC measurements

The presence of the adhesive layer near the crack plane creates an asymmetry and a possible mode II loading at the crack tip that might explain the lower amount of fibre bridging observed in joints compared to bulk composite. To verify or reject this hypothesis, DIC is used to determine experimentally the extent of mode mixity occurring in mode I delamination of asymmetric specimens.

Delamination tests

Standard Mode-I delamination tests are repeated with a slightly different measurement setup. One side of each specimen is painted white and marked every millimetre to perform crack length monitoring, while the other edge is polished and lightly sprayed with white acrylic to obtain a very fine speckle pattern for DIC measurements (see Figure 4.69).
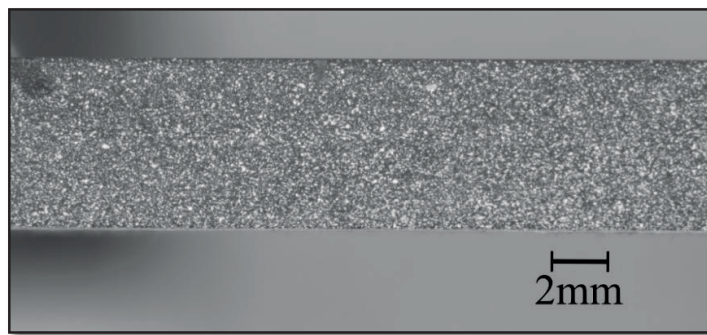
Figure 4.69: Fine speckle made with acrylic spray for DIC measurements on a DCB2-P1-A2 specimens' edge.

One DCB2-P1-B and one DCB2-P1-A2 specimens are tested with a hydraulic Instron® test machine, due to its capability to move both arms of a DCB specimen simultaneously, thus maintaining the crack plane in the field of view of the camera. This enables to take pictures of a specimen during the delamination test without moving the camera, which is required for DIC measurements (the initial picture acting as a reference).

One high resolution CCD camera (AVT Guppy F146, 1.3 Mpixels, ½'' sensor with 25mm focal length low distortion lens) focuses on one specimen's edge to follow crack length (see camera 2 view in Figure 4.70) while another takes pictures of the edge with a speckle at a rate of 0.5Hz (see camera 1 view in Figure 4.70). The targeted zone on the specimens' edge for DIC analysis is the end of the bridging zone at steady state, about 60mm from initial crack starter.

Data reduction is performed using the crack length monitoring, to ensure that the results are consistent with those from tests with the Instron 5848 machine. Since the ERR calculations show a very good reproducibility with previous results, both specimens are considered valid for DIC measurements.
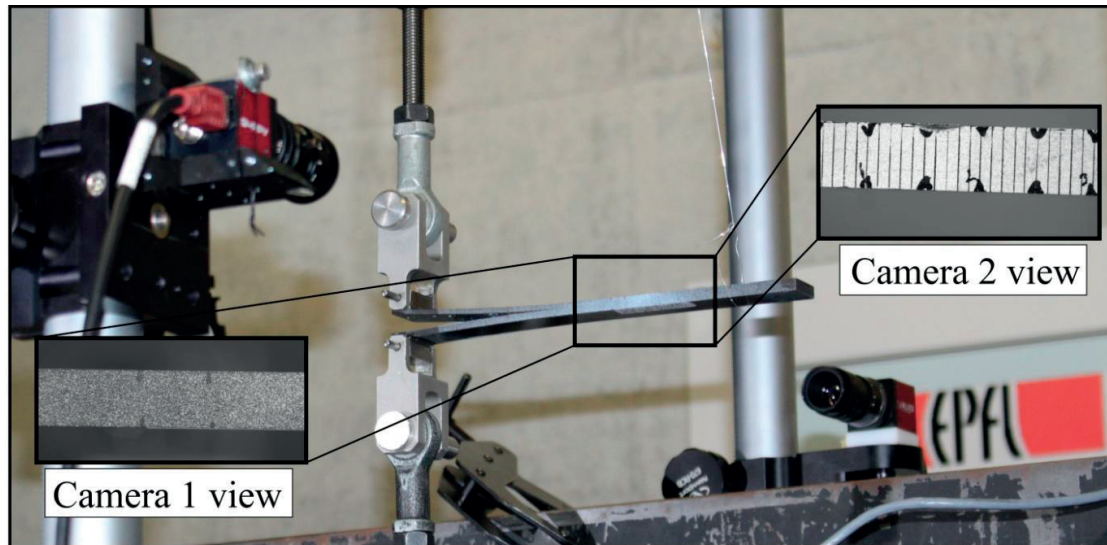
Figure 4.70: Set up of delamination test for data reduction and DIC measurements.

Choice of the parameters of DIC analysis

The pictures taken from camera 1 (see Figure 4.70) are analysed with the software VIC2D®. To achieve a robust and precise analysis, a trial and error optimization is performed on correlation parameters, which are found adequate with the following values:

- **Subset size**: 29 pixels. This parameter controls the area used for tracking the displacement between images. Hence it has to be large enough to ensure that there is a sufficiently distinctive pattern contained in the area used for correlation and sufficiently small to ensure a high enough spatial resolution of the reconstructed fields [69].
- **Step size**: 3 pixels. This parameter controls the density of analyzed data: a step size of 3 pixels means that every 3rd point in each direction will be analysed. A smaller step size returns more points but is time consuming, whereas a larger step size gives faster results but coarser data [69].
- **Splines type** for interpolation: 6-tap to ensure highly accurate displacement information.

Data extraction

The fineness of the speckle allows obtaining an excellent correlation when using the described parameters. The error of correlation is very low (less than 5% in the closest region to the crack planes, less than 0.7% otherwise).

The horizontal and the vertical components of the Crack Opening Displacement (COD_x and COD_y, respectively) are extracted along lines taken as close as possible to the crack plane. Besides, the lines for data extraction must not suffer any failure of correlation even for long crack lengths (see Figure 4.71). In the analysis of the displacement fields, a linear extrapolation of the values extracted from the lines (at 0.3 to 0.5mm from the crack plane) is used to obtain those on the crack plane. The COD_x component is directly correlated to mode II since a difference of horizontal displacement between the upper line and the lower line corresponds to a shear deformation. The vertical component corresponds to a combination of the dominant mode-I opening and a general rigid body translation rotation due to the asymmetry of the specimen. A detailed analysis of the vertical displacement

component allows determining the crack tip position, and more importantly, can be used to identify and subtract the effects of the rotation of the specimen in the calculation of the COD components.
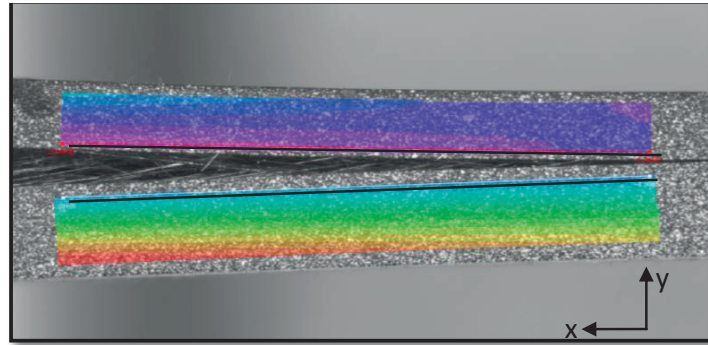
Figure 4.71: Relevant lines from which displacement is extracted for DIC analysis.

For the present analysis, the data are extracted at some relevant crack lengths only at which the fibre bridging is close to be fully developed: at a crack increment Δa=60 and 70mm for the DCB2-P1-B specimen, and at Δa=70 and 80mm for the DCB2-P1-A2 specimen.

Procedure to correct the rotation of the specimens

For each considered crack length, the COD_y component is extracted from both upper and lower lines (see Figure 4.72), and plotted on the same graph. The intersection of the obtained curves is found by fitting both of them with a 3rd degree polynomial. This intersection corresponds to the crack tip (see Figure 4.72), and the crack plane orientation is found by using a linear fit of the undelaminated part. The angle of rigid body rotation is obtained by comparing the crack plane at the deformed state with the crack plane in the reference picture (before delamination). Knowing the angle of rotation (comprised between 1.1 and 1.3° for both experiments) allows correcting the COD components through a rotation transformation matrix. Rigid body translations do not need to be compensated as only displacement differences are extracted.
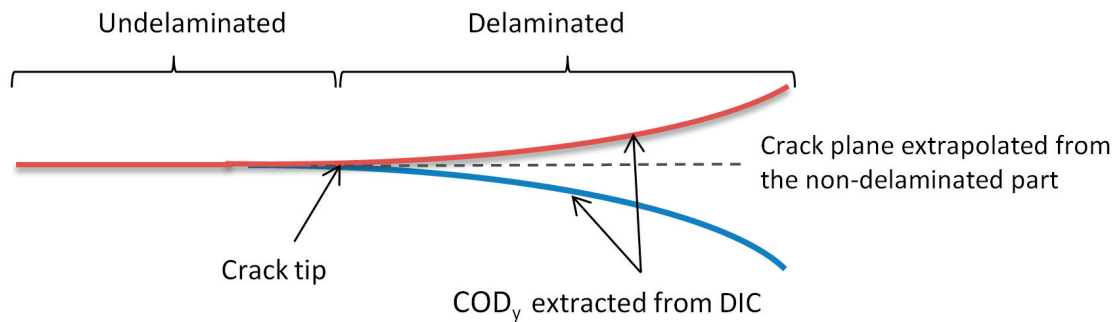
Figure 4.72: Schematic of the vertical displacement DIC measurements to determine the rotation of the specimen.

Results of the DIC analysis

The COD components, in the crack plane coordinate system, extracted from the DIC analysis of the DCB2-P1-A2 specimen are shown in Figure 4.73. The COD_x is found to be about ±0.02mm for both considered crack lengths, which is 2.5 times lower than the precision of the measurement. Also,

compared to the normal mode opening displacement, it can be considered that the shear component COD_x is negligible, i.e. there is practically no relative displacement in the fibres direction between the upper and lower beams. Mode II is thus negligible during crack propagation and mode mixity is therefore not responsible for the weakening of the fibre bridging effects observed in the presence of the adhesive layer. Moreover, these results show that the presence of the adhesive does not induce a significant mode II component in the studied configuration (DCB2-P1-A2).
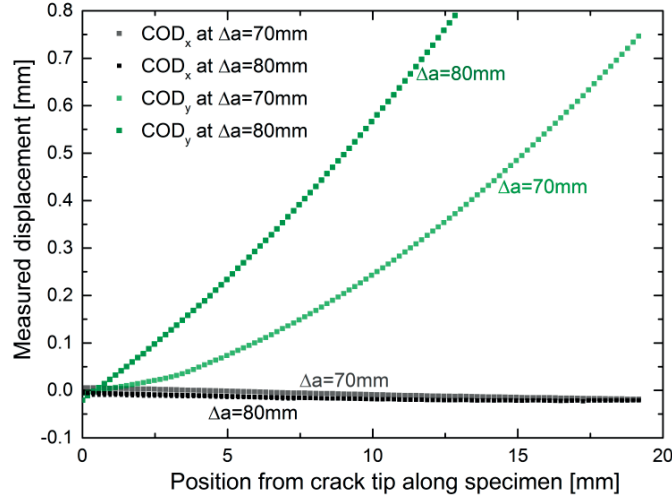
Figure 4.73: COD extracted from DIC measurements on the DCB2-P1-A2 specimen. The precision of the measure is 0.05mm hence the horizontal component COD_x can be considered negligible at both Δa=70mm and Δa=80mm.

Similarly, for the DCB2-P1-B specimen, the COD_x is found negligible (about 0.01mm) at both 60 and 70mm of crack propagation. It can be concluded that the asymmetry of the DCB2-P1-B specimens cannot induce a significant mode II component in the interlaminar delamination, which is consistent with the literature [35].

Moreover, it is verified in section 5.1 with VCCT modelling that the shear component at initiation is negligible for both studied configurations (bulk and joints). Overall, it can be concluded that the mode II component is negligible at both initiation and propagation in DCB2-P1-B and DCB2-P1-A2 specimens.

Conclusion

The mode I delamination behavior of DCB2-P1-A2 joint specimens using a thick adhesive film is investigated and results show that the fibre bridging is considerably affected by the presence of the adhesive layer. Indeed the ERR at steady state is reduced by 300 J/m^2 (-30%) for joints compared to bulk specimens while the fracture toughness at initiation remains the same for both configurations. This very significant toughness reduction can thus be attributed to a significantly lower bridging contribution to ERR, G_b, which is reduced from about 700 J/m^2 for bulk to only 400 J/m^2 in joint specimens.

Those results are consistent with results from DCB2-P1-A1 joint specimens. Both adhesives are epoxy resins but A1 is a bicomponent adhesive paste, leading to a thin adhesive layer after bonding, while A2 is a relatively thick epoxy adhesive film containing a glass carrier. Both adhesive require a very different curing cycle and show different yield strengths and hardening curves. This suggests that the observed trends are not specific to a given adhesive system. Thus, it is concluded that any epoxy adhesive layer in the surroundings of a crack in the studied unidirectional CFRP composite (SE 70 from Gurit®) can drastically weaken its mode I steady-state fracture behavior.

DIC measurements performed on DCB2-P1-A2 and DCB2-P1-B specimens subjected to mode I delamination showed that the shear displacement component during delamination is negligible for both configurations, hence neither the asymmetry nor the adhesive layer induce a substantial mode II component that could affect the fracture behavior of the composite. However the DIC measurements are performed on the specimen's edge, which is not fully representative of the whole specimens' width because of edge effect. Therefore FE modeling is necessary to investigate what happens in the bulk of the specimen.

4.3 Influence of the bondline on fibre bridging

It is now ascertained that in mode I delamination of asymmetric UD carbon epoxy laminates, fibre bridging is affected by the presence of an adhesive layer in the neighbourhood of the crack plane. In a first microscopic study, it is observed that a majority of isolated fibres are bridging in DCB2-P1-A1 and A2 while bundles of fibres, that exert larger closing forces, are bridging in the case of DCB2-P1-B specimens.

In this chapter the objective is to characterize more in depth the type of fibre bridging occurring in each laminate in terms of representative and quantifiable parameters. For both specimens' configurations DCB2-P1-B and DCB2-P1-A2, the number of isolated fibres and bundles of fibres involved in bridging are determined, and the local crack opening displacement along specimens' width is measured and analysed by means of wavelets decomposition. This gives an interesting comparison to understand the underlying differences in mechanisms between bulk and joints specimens.

4.3.1. Fibres Counting

In order to quantify the number of isolated fibres and bundles involved in bridging in each specimen configuration (DCB2-P1-A2 and DCB2-P1-B), transverse sections are realised and observed under an optical microscope. One representative specimen of each configuration is kept open after delamination: no unloading stage is performed in order to preserve the pull out fibres intact. The loading stage of each specimen is arrested in the region of stable crack growth in order to characterize a fully developed bridging. The open specimens are then embedded with mounting resin, and sliced with a diamond wire saw at 2, 7, and 15 mm from the crack tip (see Figure 4.74).
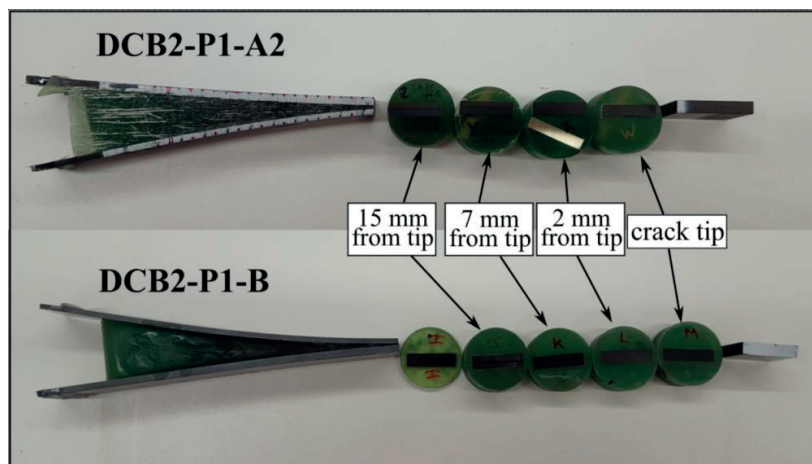
Figure 4.74: Photo of a DCB2-P1-A2 and a DCB2-P1-B specimen kept open after mode I delamination, embedded with resin, and cut to obtain microsections at some relevant points.

Afterwards the sections are polished with abrasive SiC paper with grit sizes from 800 to 4000 grit to be suitable for microscope observations. Images of the entire sections are taken with a magnification

x15; the images are combined into a single picture (covering the full width of the specimen) and the crack profile is isolated manually in Adobe Photoshop® (see Figure 4.75). The image contrast is then balanced spatially using a custom script in Matlab® and the obtained picture is converted to black and white image using a manually adjusted threshold to isolate the fibres. Similarly to the comparison in Figure 4.61, it is apparent in Figure 4.75 that only isolated fibres and small clusters of fibres are involved in bridging for joints specimens, versus substantial bundles in the case of bulk specimens. Those obtained crack profiles pictures are post-processed with a Matlab® code for counting the fibres (using the Matlab regionprops function). The number of fibres involved in bridging is determined by dividing the total fibres area by the area of a single fibre.
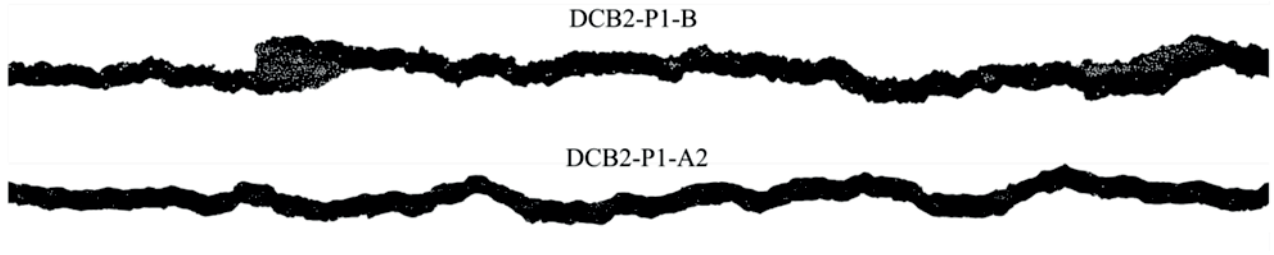
Figure 4.75: Portion of crack profiles isolated manually with Photoshop® to quantify the bridging involved in bulk and joints specimens. Those crack profiles originate from transverse sections at ~2mm from the crack tip.
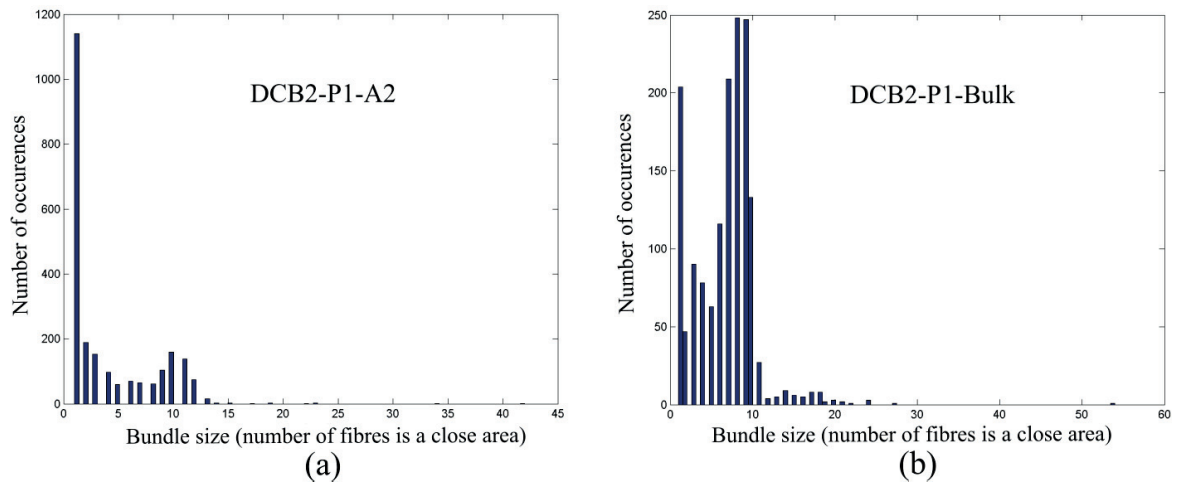
Figure 4.76: Occurrences of bundles of fibres as a function of their size for DCB2-P1-A2 specimens (a) and DCB2-P1-B specimens (b). Note that here the term "bundle" does not necessarily mean that many fibres are involved. Results obtained from transverse section at 2mm from crack tip for both considered configurations.

In order to distinguish bundles from isolated fibres, the number of neighbouring fibres is computed for each detected bundle as the area of the connected region divided by the area of a single fiber. The results are shown in Figure 4.76, where the occurrence number of bundles is plotted against the number of fibres in a connected bundle (from 1 for an isolated fibre, to 60 for a consequent cluster of fibres). It can be observed that in the bulk specimen, many clusters of 10 up to 54 fibres contribute to bridging, whereas an overwhelming majority of isolated fibres or bundles of less that 12 fibres are

73

measured in the joint specimen. More precisely, about 1150 isolated fibres are counted for joints versus only 200 for bulk. The same trend is observed in transverse sections at 7mm and 15 mm from the crack tip. Since bundles with many fibres dissipate much more energy than isolated fibres during delamination [45], it can be concluded that the difference of R-curve behavior observed between joints and bulk specimens can be attributed to a very different type of bridging fibre bundle size distribution.

4.3.2. Local COD measurements

The correlation between presence of an adhesive layer and a lower size of bundles is also evaluated with the reconstitution of the local crack opening profile along the whole width of the specimen: the local COD is calculated from reconstructed position of the upper and lower crack front in the microscopic sections. If a large bundle of fibres is present, the local COD will be more important locally due to the fibre detachment (see Figure 4.77), and thus can be used to evaluate the intensity and spatial distribution of fibre bridging.
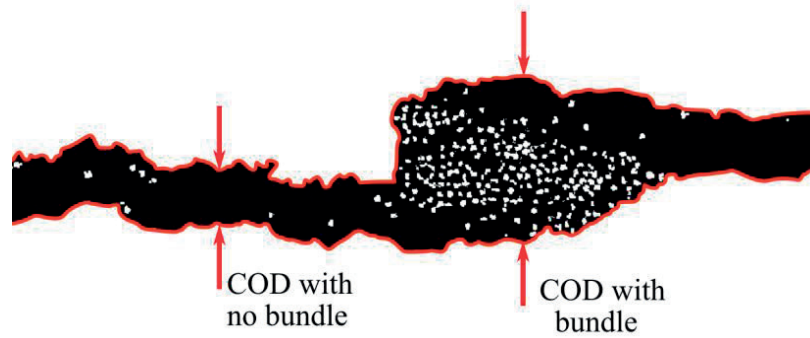
Figure 4.77: Measured difference of local Crack Opening Displacement with and without a bundle of fibres (detail view of the whole image).

To reconstruct the COD profile, the same manually defined crack profiles from microsections (see section 4.3.1) are post processed: for each specimen configuration (DCB2-P1-B and DCB2-P1-A2) the picture with the entire crack profile along the width is converted to black and white with no distinction for the fibres (see Figure 4.78). From the obtained image, the upper and the lower positions of the crack along the width are computed with a Matlab® code, and by subtracting the heights of the lower line from the heights of the upper line, the COD along the specimens' width is obtained with a high accuracy. In this signal, we are mostly interested in the spatial fluctuation of the COD around its mean value which represents indirectly a measure of the volume of fibre & matrix acting in the bridging zone.

Then the signal constituted by the COD profile along the width is analyzed using a discrete wavelet decomposition (using Matlab® signal processing toolbox). A total of 12 levels of Haar wavelet decomposition, each corresponding to a characteristic detail of a size of 2^n pixels (n = 1,12), are used to analyze each profile (bulk and joint).

crack profile from DCB2-P1-A2 or DCB2-P1-B cross section

Conversion to Black and white

Conversion to COD measurement
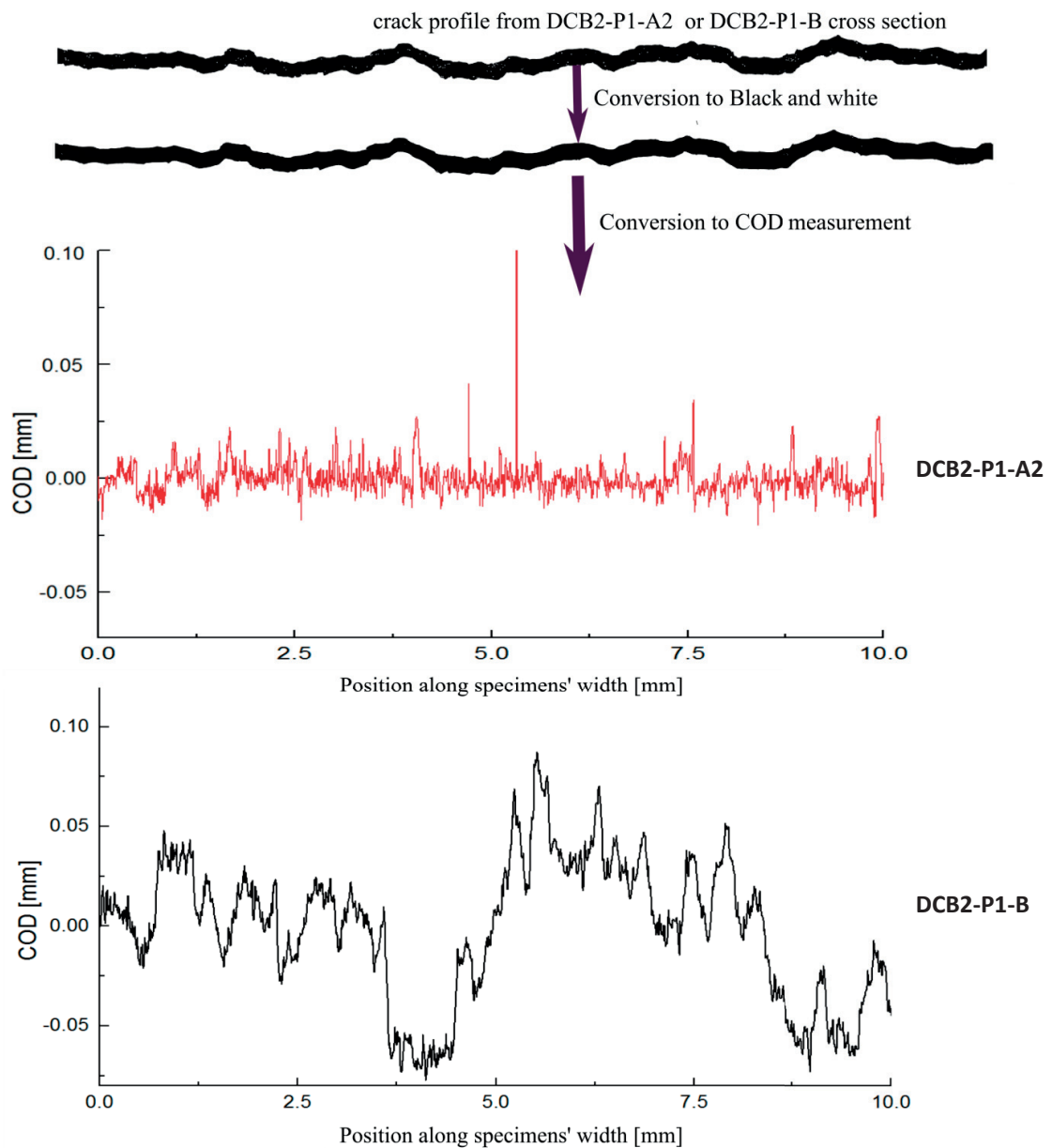
Figure 4.78: Post processing steps to obtain the COD profile from crack profiles for bulk and joints specimens.

The original signal is denoised by taking into account only the 8 first decomposition signals, which correspond to a scale ranging from the fibre level to the bundle level. In other words, the fluctuations of COD due to the global waviness of the crack are discarded from the analysis: only the variations of COD due to presence of bundles and fibres are retained and thus the obtained signal can be considered a measure of the amount and distribution of bridging ligaments.
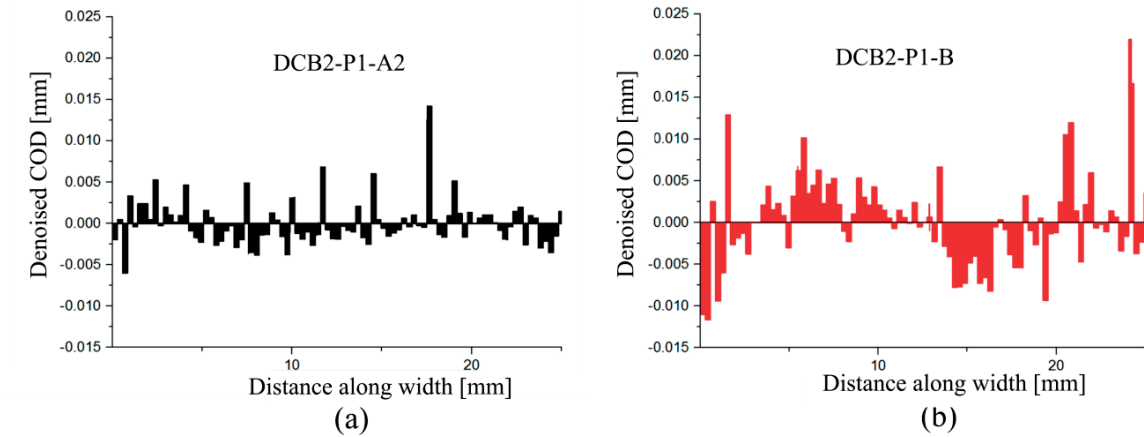
Figure 4.79: Denoised COD profiles obtained from upper and lower crack profiles along whole width of specimens DCB2-P1-A2 (a) and DCB2-P1-B (b).

The resulting denoised COD profiles are shown in Figure 4.79 for both bulk and joint specimens. It is clearly visible that the overall area of bridging ligaments is much smaller for joints than bulk. Also the profile is steadier and more homogeneous in the joint than in the bulk specimen. Only small size discontinuities are observed in the joint, corresponding to small fibre bundles while larger discontinuities are observed in the bulk specimen, which correlates well with larger bundle size..

This comparison of COD profiles along width is consistent with the results from fibre counting and bundle analysis (section 4.3.1): the delamination behavior difference can be explained by the absence of large bundles participating to the bridging in joints.

Conclusion

This section is devoted to quantify the fibre bridging mechanisms in terms of bundle size in both DCB2-P1-B and DCB2-P1-A2 specimens. The results show that fibres participating to bridging are mostly isolated in the case of joints, whereas they tend to congregate to form clusters in bulk specimens. It has been shown by [45] that in the latter case, the closing forces applied on the crack surfaces are much more important, leading to larger fracture toughness at steady state compared to joint specimens. It is also observed that the COD fluctuations due to bridging is more heterogeneous and intense in bulk than in joint specimens, and considering that largest amplitudes of COD variation are correlated with the presence of significant bundles of fibres, the results are consistent with the fibre counting and bundle size analysis. These observations qualitatively explain the observed difference in R-curve behavior of joint vs. bulk specimens however it remains to be understood why the presence of an adhesive layer triggers a development of a different bridging with more isolated fibres and few bundles.

Chapter 5: FE modeling

In this work several FE models with different modeling approaches are used with the following purposes:

1. Analysis of conditions prevailing at crack initiation without fibre bridging
2. Identifications of steady state bridging tractions in mode I delamination of adhesively bonded specimens DCB2-P1-A1.
3. Cohesive law formulation and prediction of mode I delamination behavior (load displacement curve and crack growth) of DCB2-P1-A1 specimens.
4. Assessment of the adhesive layer influence on the stress fields nearby the crack tip.

All those models have a shared goal: understanding the difference of interlaminar delamination behavior between asymmetric unidirectional bulk composite specimens and asymmetric bonded joints.

5.1 Crack analysis in 2D at initiation

Several numerical models are created to analyse the considered cracked specimens at initiation when the phenomenon of fibre bridging is not yet active. First a 2D model using the Virtual Crack Closure Technique (VCCT) is proposed to investigate the mode mixity, defined as $G_{II}/(G_I+G_{II})$, due to specimens' asymmetry. Subsequently a 2D simulation is performed to investigate the influence of plastic behavior of the adhesive layer in DCB2-P1-A1 specimens on the ERR at initiation.

5.1.1 Determination of the mode mixity with VCCT

Since the crack starter is not placed in the midplane in asymmetric DCB specimens, the asymmetry may cause a mode II component during remote mode I loading. A numerical study using the VCCT has been carried out to quantify the amount of mode mixity as a function of the crack starter position. For both bulk and joint specimens, three different crack plane offsets are investigated: DCB1, DCB2 and DCB3 (1,2 and 3 plies above bond layer, respectively) to determine the extent of mode II, thus a total of 6 models are built. Note that configuration DCB3 is not experimentally tested.

In order to implement the VCCT with Abaqus® v6.12, once a model of the desired asymmetry is ready, some modifications on the input file are required, since Abaqus/CAE window does not allow giving the necessary instructions[1]. The Benzaggagh-Kenane (BK) mixed mode fracture criterion successfully fits the trend of the fracture energy as a function of the applied mode mixity for the considered composite material [49], and is therefore used as crack propagation criterion in the model. This criterion is expressed as follows:

$$G_{equivC} = G_{IC} + (G_{IIC} - G_{IC}) \left(\frac{G_{IIC}}{G_{IC} + G_{IIC}} \right)^{\eta} \qquad \textbf{(5.1)}$$

where η is a fitting parameter and G_{IIC} the experimental critical energy in mode II.
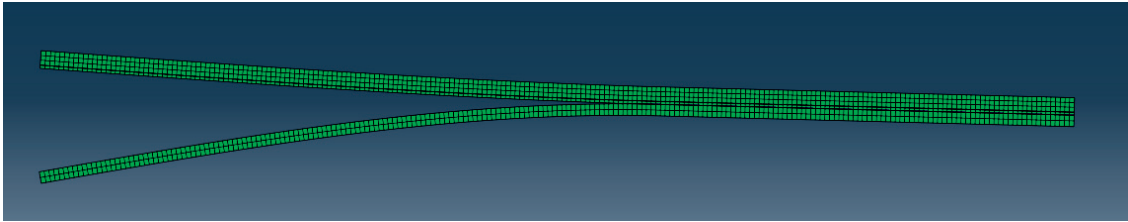
Figure 5.80: Coarse mesh suitable for crack analysis using VCCT in DCB3-P1-A1 configuration

---

[1] Thus the following command lines are added in the input file:
*INITIAL CONDITIONS,TYPE =CONTACT
 BOTSURF, TOPSURF, BNODES
 *CONTACT PRINT
*DEBOND,SLAVE=BOTSURF,MASTER=TOPSURF
*FRACTURE CRITERION,TYPE=VCCT,MIXED MODE BEHAVIOR=BK
where *BOTSURF*, *TOPSURF* are respectively the slave and master surfaces, bonded together with the set of nodes named *BNODES*.

Since the VCCT is known to incur convergence issues when refining the mesh size, the only suitable mesh is found to be relatively coarse (see Figure 5.80) and a total of 1540 biquadratic plane strain elements with reduced integration (CPE8R) are employed.

The two fracture components G_I and G_{II} are extracted from the models for each configuration in order to calculate the mode mixity defined as $G_{II}/(G_I+G_{II})$.

The results shown in Figure 5.81 demonstrate that the extent of mode II is overall higher for joints than for bulk specimens due to the increased compliance due to the adhesive layer. While it is negligible (<4%) for configuration with small crack offsets such as DCB1-P1-A1 and DCB2-P1-A1 , it can reach 10% for larger offsets (DCB3-P1-A1) at initiation. However, those simulations do not take into account the fibre bridging mechanism, which dissipates a significantly larger amount of energy and can induce large changes in the mode mixity at crack tip. Therefore the 10% of mode II contribution at initiation (~30 J/m^2) would become negligible when bridging is developed (total ERR of about 1000 J/m^2). Concerning the configurations DCB1 and DCB2 (for both bulk and joints specimens), numerical results are consistent with DIC measurements, and confirm that mode II component can be neglected for configurations DCB1 and DCB2. Those results are also in agreement with the literature [32,35].
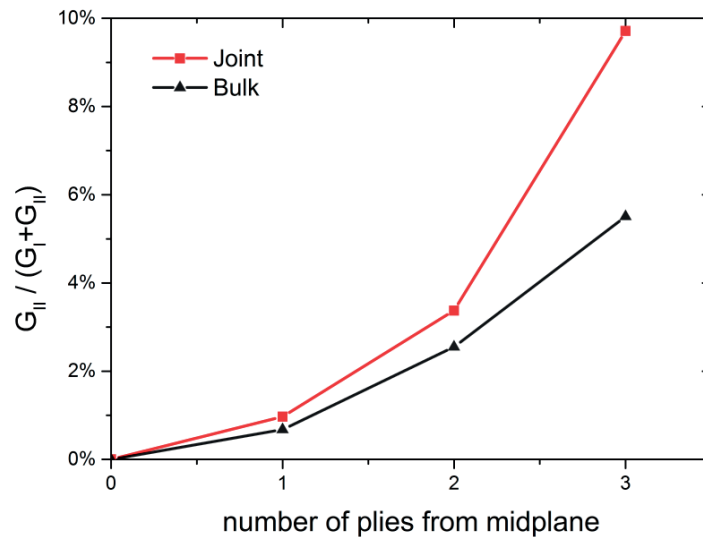
Figure 5.81: Mode II ratio as a function of crack plane offset for DCB specimens with and without adhesive layer.

5.1.2 Numerical analysis with J-integral calculations

Characterization tests showed that both adhesives A1 and A2 present an elasto-plastic behavior (see section 4.1.2 and 4.2.2). In order to investigate its influence on the stress fields around the crack tip at initiation, the DCB2-P1-A1 and DCB2-P1-B configurations are modelled in 2D plane strain elastic models, (see section 2.10.2 for details). A total of 87 500 quadratic plane strain elements (CPE8R) are employed for the simulation of the DCB2-P1-B specimen, and for the DCB2-P1-A1 configuration. The adhesive layer is modelled as an isotropic elasto-plastic material with Von Mises isotropic hardening defined according to the corresponding measured stress strain response (section 4.1.2).

The mesh is refined close to the crack tip (see Figure 2.26) and 10 contour integrals are computed for each configuration in order to ensure the path independency. The simulations are performed with displacement control at the loading pins with an opening displacement corresponding to the experimentally determined initiation point (Δ= 4.5mm).

The J-integrals extracted from models of DCB2-P1-B and DCB2-P1-A1 at initiation does not show a significant difference: 582 J.m^{-2} versus 580 J.m^{-2}, respectively. The reaction force at the loading point is almost identical. Also no significant difference in terms of stress at the crack tip is observed in the models between joints and bulk specimens. Nevertheless these models show that the stress field applied to the adhesive layer is high enough to produce plastic strain in the bond layer (the stress is higher than the yield stress). As shown by these J-integral calculations, the plastic deformation occurring in the adhesive layer only slightly affects the energy available for the crack propagation. However, as the model only represents initiation, it is not sufficient to rule out any further interference of plasticity with the bridging fibre phenomenon. This hypothesis is investigated in section 5.2.

Configuration	Extracted J-integral
DCB2-P1-A1	580 J/m^2
DCB2-P1-B	582 J/m^2

Table 5.4 : Extracted J-integral from 2D models at initiation with hardening behavior of the adhesive layer taken into account.
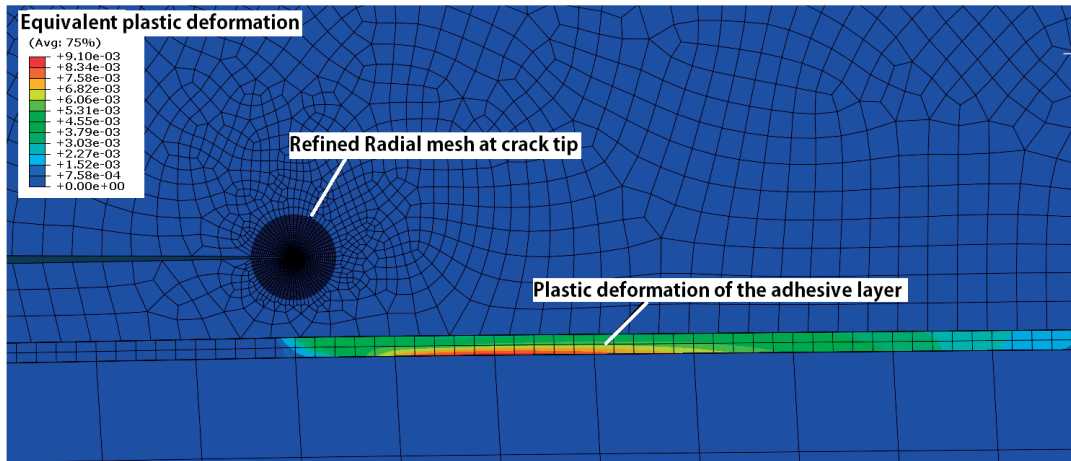
Figure 5.82: Snapshot of the model at initiation of a DCB2-P1-A1 showing that the adhesive layer incurs plastic deformation during mode I delamination.

Curvature comparison

The relatively high compliance of the adhesive layer can introduce a difference of curvature between the upper and the lower beam of a DCB2-P1-A1 specimen (or a DCB2-P1-A2). As described in [21], the curvature of the arms of DCB can affect the magnitude of bridging during delamination. To investigate this hypothesis, the same models used for the calculations of the J-integrals are employed to evaluate the curvature of the upper and the lower beams of joint DCB2-P1-A1 and bulk DCB2-P1-B specimens. Note that the considered crack length in the model is 110mm, and the applied

displacement 13.5mm and is consistent with the experiment. The curvature of each beam is calculated using 2 different ways:

- Calculation of the second derivative of the vertical displacement extracted on the crack surfaces
- Assuming the linearity of the strain field in the thickness of the arms, the longitudinal strains extracted on crack surfaces are divided by the distance from the neutral axis.
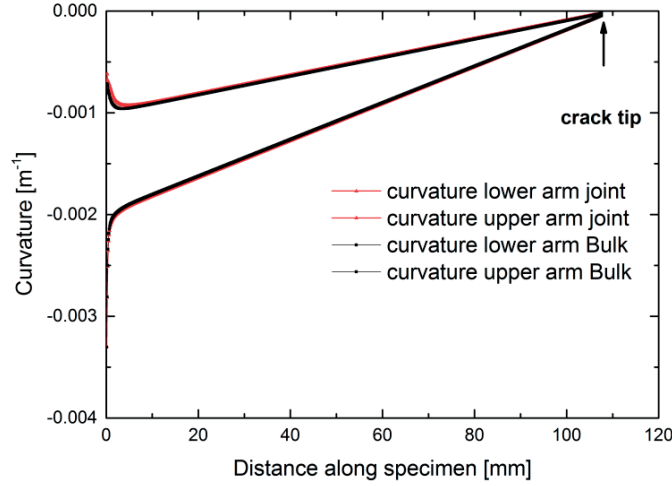
Figure 5.83: Comparison of the curvature of the beams for DCB2-P1-A1 and DCB2-P1-B specimens. The curvature is calculated by dividing the longitudinal strains extracted along crack surfaces by the distance from neutral axis.

The results calculated from the extracted strains (see Figure 5.83) show that for a given crack length and applied displacement, the curvature of the upper beam is the same for bulk and joint specimens, as well as for the lower beams. The curvatures calculated from the displacement fields give the same results. Consequently it can be concluded that the change of bending stiffness of the beams due the adhesive layer is negligible. In consequence, the different bridging mechanisms observed cannot be explained by curvature effects.

This is also confirmed by Classical Laminates Theory (CLT): the effective flexural modulus E_{11}^f is calculated for both DCB2-P1-A1 and DCB2-P1-A2 with the formula from CLT in order to determine an equivalent EI (using equation 3.8) and graphically determine the expected G_{ss} using the modified scale function graph defined in section 3.2.2. If only the change of compliance due to the adhesive layer is taken into account, the expected G_{ss} for DCB2-P1-A1 and DCB2-P1-A2 specimens are 927 and 940 J/m^2, respectively (see black square dots in Figure 5.84), thus almost unchanged compared to bulk specimens (934 J/m^2). Therefore, the change of compliance of the specimens with an adhesive layer (A1 or A2) has a negligible influence on the G_{ss} value.

It is noted that the experimental value of G_{ss} for bulk specimens is in excellent agreement with the predicted one, whereas the experimental results of joint specimens (see blue dots in Figure 5.84) are far from the expected values, thus the scale function derived by Farmand-Ashtiani *et al.* for bulk specimens is unable to predict the G_{ss} value of bonded joints specimens.
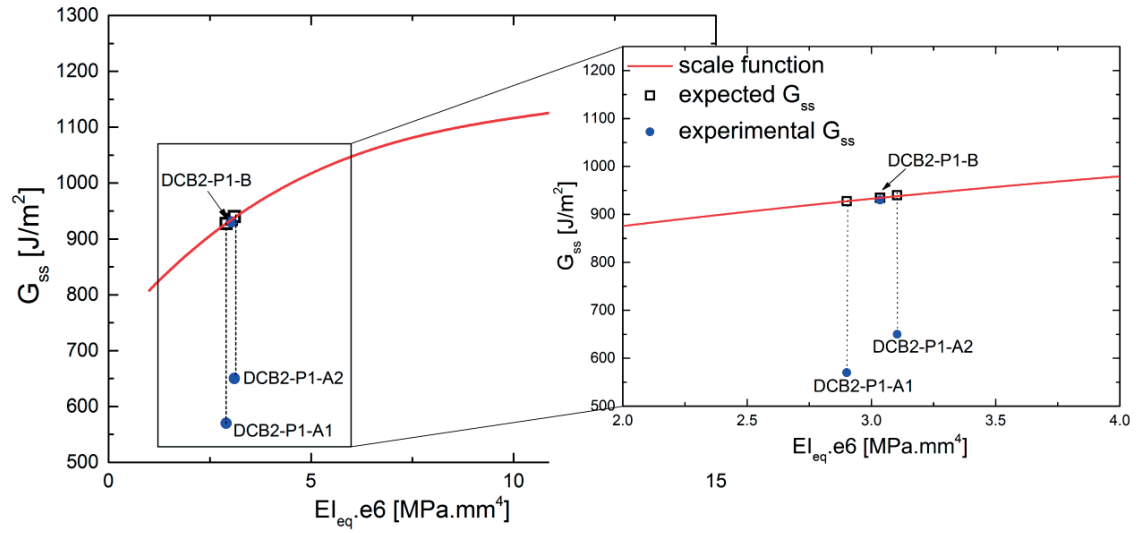
Figure 5.84: G_{ss} scale function adapted from [21] as a function of the equivalent EI_{eq}. Expected values are in black square dots, and experimental values are in blue dots. This scale function that takes into account the change of stiffness of the joint specimens fails to predict the G_{ss} values for both DCB2-P1-A1 and DCB2-P1-A2.

As a consequence of the results from both modelling (no change of curvature) and the use of the modified scale function (no impact on the G_{ss} value) it can be concluded that the change of compliance of a specimen due to the presence of an adhesive layer has almost no effect on the delamination behavior.

Conclusion

The results of the models without bridging show that the stress applied to the adhesive layer is high enough to induce plastic deformation of the epoxy adhesive (A1). Nevertheless neither the stress fields extracted from 2D models nor the J-integral contours are affected by the bond layer: they are identical for DCB2-P1-A1 and DCB2-P1-B configurations.

5.2 Cohesive element simulations

Since the stress applied to the adhesive layer is high enough to induce plasticity of the adhesive A1, it is necessary to investigate the interplay between interface damage and adhesive layer plastic deformation. Therefore a Cohesive Zone Model (CZM) is built for the configuration DCB2-P1-A1. The tractions separation law introduced in the CZM is determined with a parametric FE model following the same procedure as for DCB2-P1-B (see section 3.2). These cohesive elements simulations also aim to give more information in order to understand the involved mechanisms in the change of delamination behavior when an adhesive layer is added.

Identification of the bridging tractions

Similarly to DCB2-P1-B, a 2D plane strain simulation is first performed with the bridging tractions applied on both faces of the crack to account for fibre bridging. A total of 68600 quadratic plain strain elements with reduced integration (Abaqus CPE8R) are used for meshing the model. The procedure to determine the three bridging parameters σ_{max}, γ and z_{max} is described in this section.

As for bulk specimens, the value of σ_{max} is considered constant at 1.38 MPa (see section 3.2) based on the available literature for this composite material [18,21]. The value of bridging zone length z_{max} is graphically determined at ~60mm by plotting the crack increment against the applied displacement: when the curve becomes linear, the bridging is considered fully developed (steady state) and the corresponding crack increment is the maximum bridging length (see Figure 5.85).
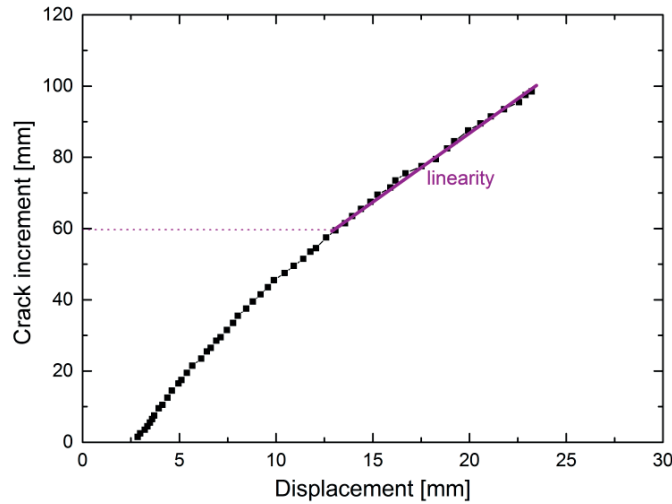
Figure 5.85: Crack growth as a function of applied displacement for a DCB2-P1-A1 specimen. The curve becomes linear at Δa=60mm denoting steady state condition.

The non linear decay of the tractions γ is identified at 0.24 mm^{-1} so that the numerical integration $\int_0^{\delta_{max}} \hat{\sigma}_b(\delta)\,d\delta$ corresponds to the contribution of bridging $G_{I,b}$= 170 J/m^2 as determined experimentally (see Figure 5.86). At each trial iteration, the Crack Opening Displacement $\delta(z)$ extracted from the model is combined with the bridging tractions $\sigma_b(z)$ to establish the tabular

83

cohesive traction-separation relation $\hat{\sigma}_b(\delta)$ and compute the bridging ERR integral. At the end of the identification process, the identified triplet of parameters σ_{max}, γ, z_{max} for joint specimens DCB2-P1-A1 is found as (1.38 [MPa], 0.24 [mm^{-1}], 60 [mm]).
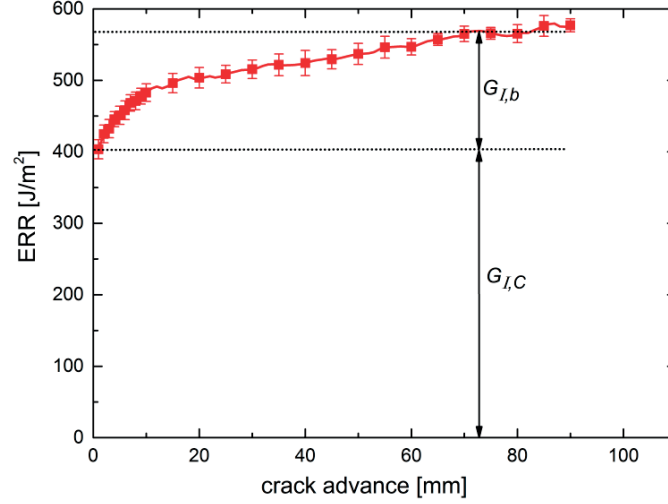
Figure 5.86: Average R-curve for DCB2-P1-A1 specimens calculated with CCM. The fracture energy at initiation is 400 J/m² and the contribution of bridging is about 170 J/m².

Cohesive law

Following the same procedure as for DCB2-P1-B in section 3.2, the initial linear decay part of the cohesive law is determined so that $G_{I,C}$ is equal to the measured initiation ERR 400 J/m² (see Figure 5.87). The critical transverse stress level σ_C is considered to be the same as for bulk configuration, with a value of 23MPa. A convergence study shows that the initial cohesive stiffness K_p taken equal to 9200 MPa.mm^{-1} ensures that the cohesive elements are rigid enough to not influence the loading response. The damage initiates at 12% of the opening δ_b occurring at the end of the initial part of the cohesive law.
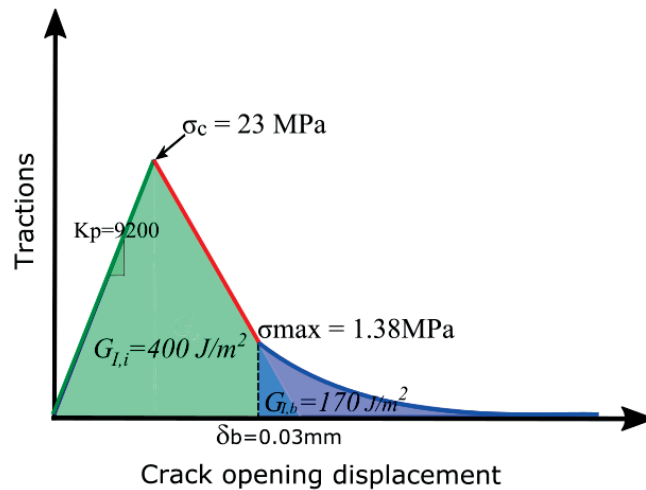
Figure 5.87: Identified cohesive law for DCB2-P1-A1 specimens.

84

The identified bridging law from the previous section $\hat{\sigma}_b(\delta)$ is appended to the second part of the curve (see Figure 5.87). Note that the area under the full obtained traction separation curve is equal to the total ERR G_{ss} =570 J/m^2 and is consistent with the experimental results.

The obtained cohesive law is introduced in Abaqus® through a tabular multi-linear damage evolution function (as described in section 3.1) to simulate crack growth in DCB2-P1-A1.
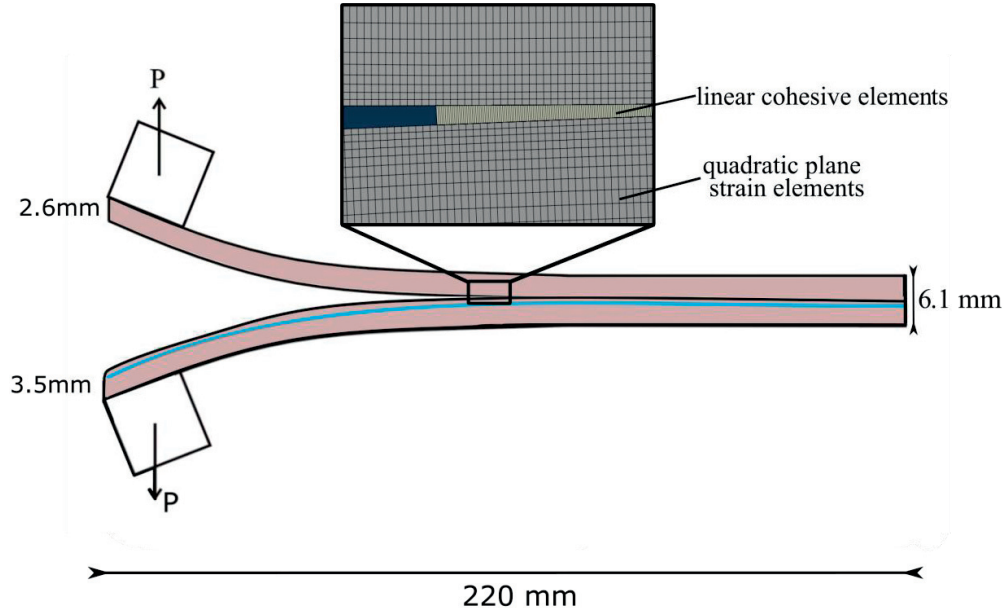
Figure 5.88: Cohesive Elements Model of a DCB2-P1-A1 specimen. The blue line represents the adhesive layer.

The simulation consists in predicting the crack propagation and the experimental load-displacement curve by using 2D-cohesive elements to represent the delamination process including bridging tractions. Both arms of the DCB2-P1-B are modelled, and discretized with 29400 quadratic plane strain (CPE8R) elements for the upper arm and 36000 for the lower arm, since the thickness of the beams is different. A 20 μm-thick layer of 6480 linear cohesive elements (COH2D4) is tied to the two arms along the delamination path, i.e. from the initial crack length to the end of the specimen. The adhesive layer is introduced as an isotropic elasto-plastic material with the properties obtained from the dogbones tests following a Von Mises yield criterion.

The simulation is run with a displacement control until 19.3 mm opening. The obtained load displacement response (see Figure 5.89) is in very good agreement with the experimental one, which proves the correctness of the identified cohesive law. In particular, the initiation and propagation load are well captured, and the overshoot in the raising part of the curve that is regularly encountered using this procedure, is satisfactorily low. Moreover, the crack growth prediction is very accurate (error <2.5mm).
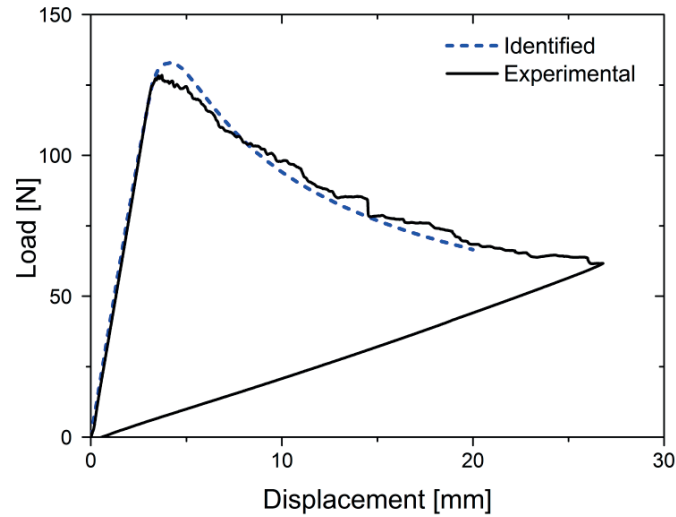
Figure 5.89: Experimental and numerical load displacement response of DCB2-P1-A1.
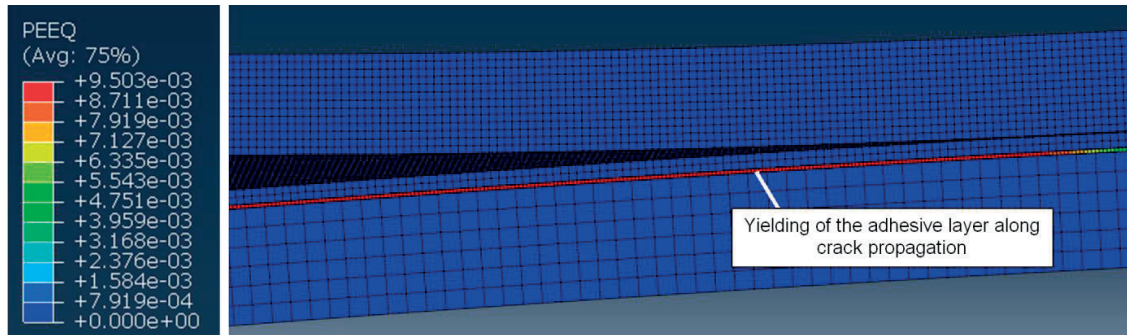
Figure 5.90: Picture of the deformed specimen (CZM) showing the equivalent plastic strain. It is observed that the adhesive layer is heavily deformed all along the crack propagation.

The results of this model simulating crack growth with bridging show that the adhesive layer is submitted to a stress beyond its yield point (see Figure 5.90). Indeed, the stress state close to crack front generates an equivalent plastic strain of up to 0.95% that remains in the wake of the crack. These results extend the first observations of yielding of the glue from the simulations at initiation (without bridging).

The energy dissipated by plastic deformation of the adhesive layer is extracted from the FE simulation, and compared to the total work of external forces involved in the process in Figure 5.91. It can be observed that the plastic deformation of the adhesive A1 is energetically negligible compared with damage: it dissipates less than 1.5% of the total energy, whereas the damage represents more than 60% of the total energy. Therefore the plastic behavior of the adhesive layer cannot energetically explain the change of fracture behavior between joint and bulk composite specimens.
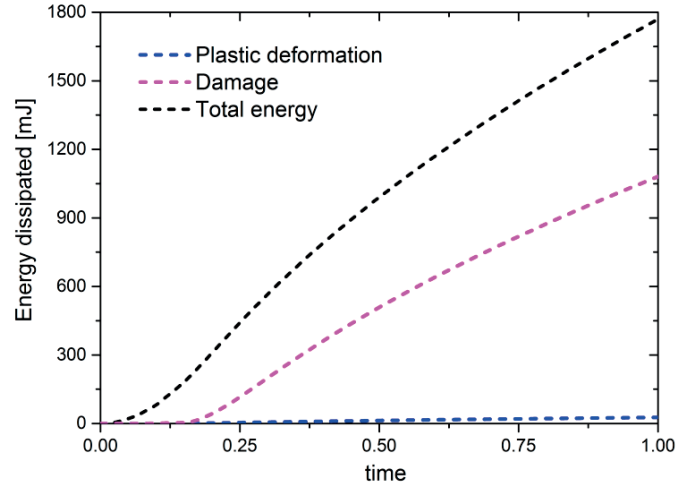
Figure 5.91: Energy distribution from the cohesive zone FE Model of a DCB2-P1-A1 specimen.

It is interesting to compare the identified cohesive laws for a DCB2-P1-B bulk specimen (see section 3.2) and for a DCB2-P1-A1 joint (see Figure 5.92), since both successfully describe the delamination behavior of the respective considered specimens. The first bilinear parts mainly differ by their initial slope and the area under the curve, corresponding to the fracture toughness at initiation (27% higher for DCB2-P1-A1 specimens than for bulk specimens).
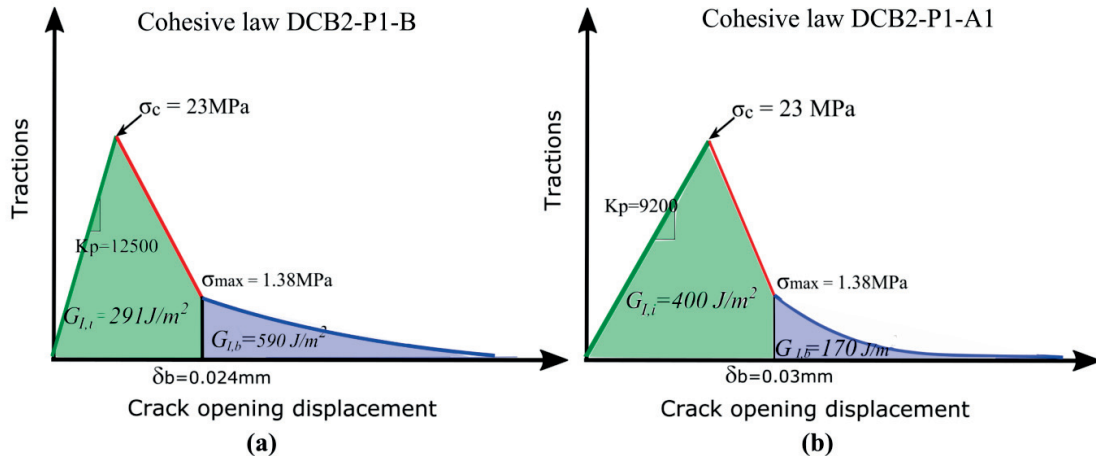
Figure 5.92: Schematic comparison of the cohesive laws of (a) DCB2-P1-B and (b) DCB2-P1-A1 specimens.

The smaller contribution of bridging in joint specimens is mainly visible by the higher rate of traction decay in the last part of the curve compared with the bulk case.

Summary

In this part, the bridging laws for both bulk and joint configurations have been identified and exhibit significantly different bridging parameters. Cohesive elements simulations were performed and found to fit the load displacement curves very well for both cases, and predict the crack length with good accuracy. This proves that this method, which consists to identify a cohesive model for a specific crack position offset in the presence of an adhesive layer, can be used for prediction purposes.

Moreover, it has already been shown by Farman-Ashtiani *et al.* [21] that the cohesive law is geometry dependent (and thus not a material property); and this study shows that it is also dependent on the presence of a ductile adhesive layer.

However, an energetic analysis extracted from the CZM showed that the plastic deformation occurring in the adhesive layer is not responsible for the change of toughness properties of the composite.

Therefore, it is necessary to employ a 3D-model to understand the influence on the stress field of a compliant layer close to the crack tip.

5.3 Modeling in 3D

In order to complete the investigation of the effect of the adhesive layer ductile behavior on the stress field in the vicinity of the crack tip, a 3D model of a DCB2-P1-A2 specimen is constructed with the software Abaqus®. Only half of the specimens' width is modelled, with adequate boundary constraints to satisfy the symmetry. The adhesive layer is modelled as an isotropic elasto-plastic material with Von Mises isotropic hardening defined according to the experimentally measured stress strain response (section 4.2.2). A second 3D model with the exact same geometry is also created, and referred to as "Equivalent Bulk" model since the adhesive layer is simply assigned bulk composite properties, keeping the same overall geometry as DCB2-P1-A2. By comparing the results from the 2 models, the influence on the stress field of the difference of properties between CFRP and adhesive can be assessed. Also, free-edge effects and shear through the width are taken into account in the 3D simulations. A partial view of the 3D-model is given in Figure 5.93 with details of the different parts around the crack tip.
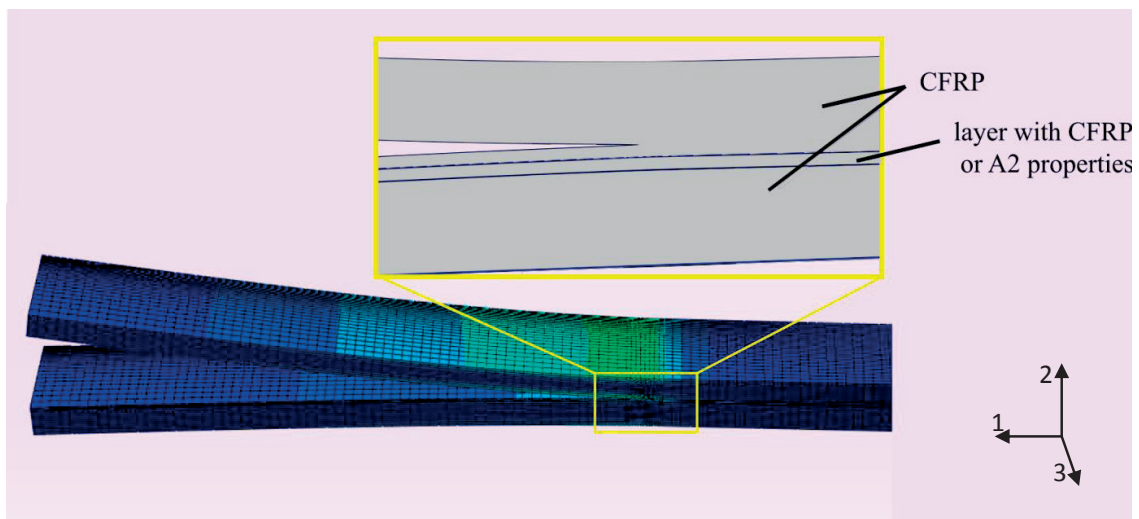
Figure 5.93: Partial view of the 3D models constructed with Abaqus with a detailed view of the parts near the crack tip. The geometry corresponds to a DCB2-P1-A2 specimen. In one model, the adhesive layer has the elastoplastic behavior of A2 extracted from SLS tests, whereas in the second model, the same layer is assigned with composite material properties.

Both models contain a total of 129 000 quadratic elements with reduced integration (C3D20R). The mesh is refined around the crack tip. Results are displayed with both 3D and 2D views for the different considered stress fields, followed by the plots of the extracted stresses along selected paths.

The stress fields in each normal direction are first represented in Figure 5.94, Figure 5.95 and Figure 5.96 where the model is cut at about 3 mm from crack tip to highlight the differences. The repartition of the stresses is obviously different when an adhesive layer is present. Considering the longitudinal stress field σ_{11} displayed in Figure 5.94, it is continuous in the Equivalent Bulk simulation, whereas a green layer indicating a much lower stress level is observed in the model with adhesive properties. Interestingly, the stress field presents a severe discontinuity, but stresses continue to spread beyond

the adhesive layer in the composite. This "shielding effect" of the adhesive layer is thus spatially limited.

The normal stress field in the opening direction σ_{22} represented in Figure 5.95 spreads over the adhesive layer upper border in the Equivalent Bulk model, while the stresses sharply decrease in the DCB2-P1-A2 model. Moreover, the size of the saturated stress level region (in grey) corresponding to values above 75MPa is more extended in the bulk model than in the adhesive joint model. It should be noted that thanks to the constraining effects, the adhesive layer is able to transfer a high normal stress of more than 60 MPa close to crack tip, which is above its unconfined yield stress.

The same observations can be made on the lateral normal stress field σ_{33} represented in Figure 5.96. In this latter case, the view cut in the 3D representation is made very close to the crack tip, revealing a much higher stress field in Equivalent Bulk compared to DCB2-P1-A2, as well as significant 3D effects: the stresses in direction 33 (in the width direction) are maximum in the middle of the specimen, and decrease to zero on the specimens' free edge over a distance of about one time the adherent thickness. As expected, the most part of the specimen is experiencing a quasi-plain strain condition in which the lateral stresses and triaxiality are important close to crack tip. Indeed the bulk composite and adhesive are in a state of triaxial tension close to crack tip. The free edge affected areas are experiencing a stress state close to plain stress as $\sigma_{33} = 0$ that is close to a biaxial tension. It is also interesting to note that the lateral stresses in the adhesive layer increase faster than in the bulk when moving away from the free edge. This effect is explained by the strong confinement experienced by the adhesive.
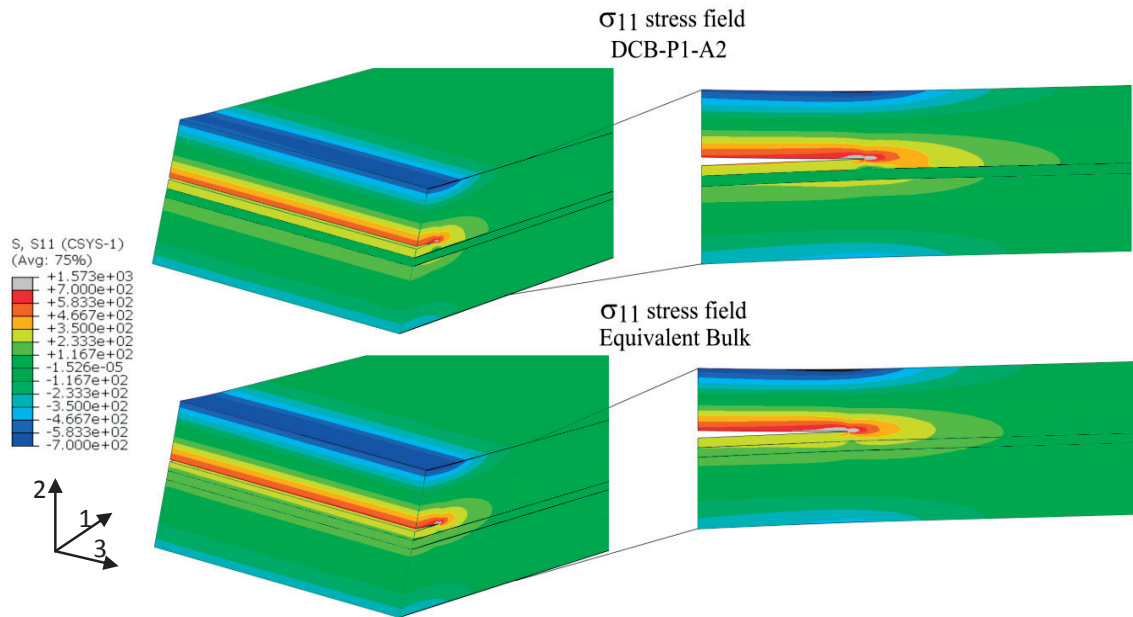
Figure 5.94: Stress field σ_{11} comparison from 3D FE Modeling with an applied displacement of 8mm. The stresses are in [MPa], and the visible edge is the bulk side (symmetry plane).
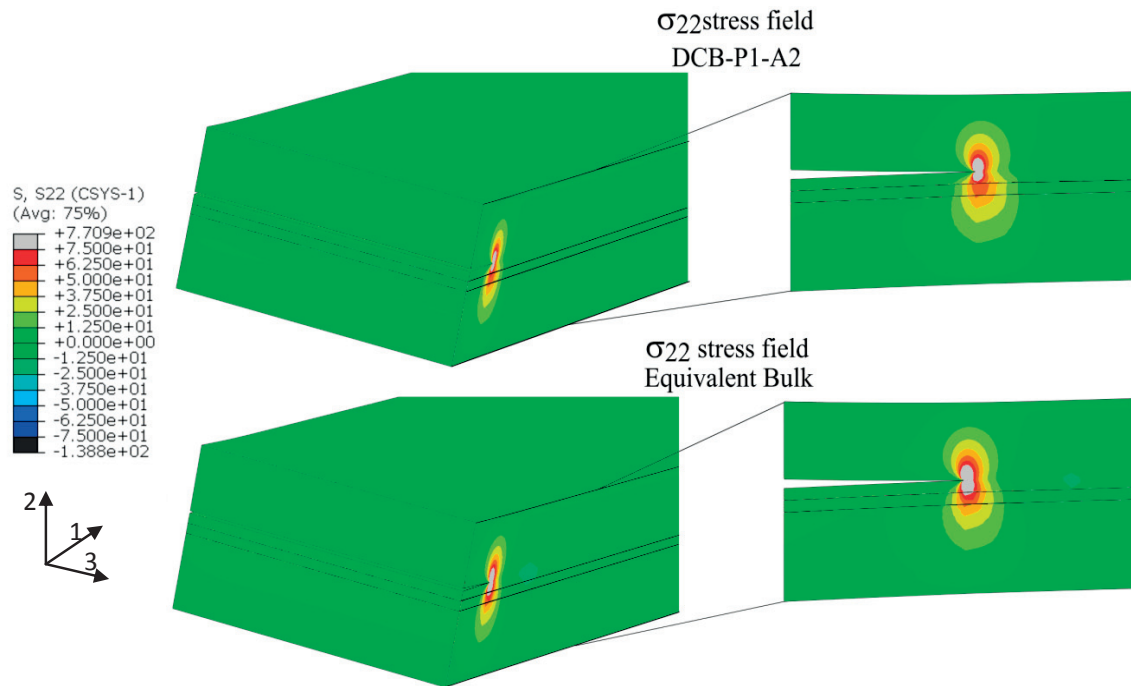
Figure 5.95: Stress field σ_{22} comparison from 3D FE Modeling with an applied displacement of 8mm. The stresses are in [MPa] , and the visible edge is the bulk side (symmetry plane) .
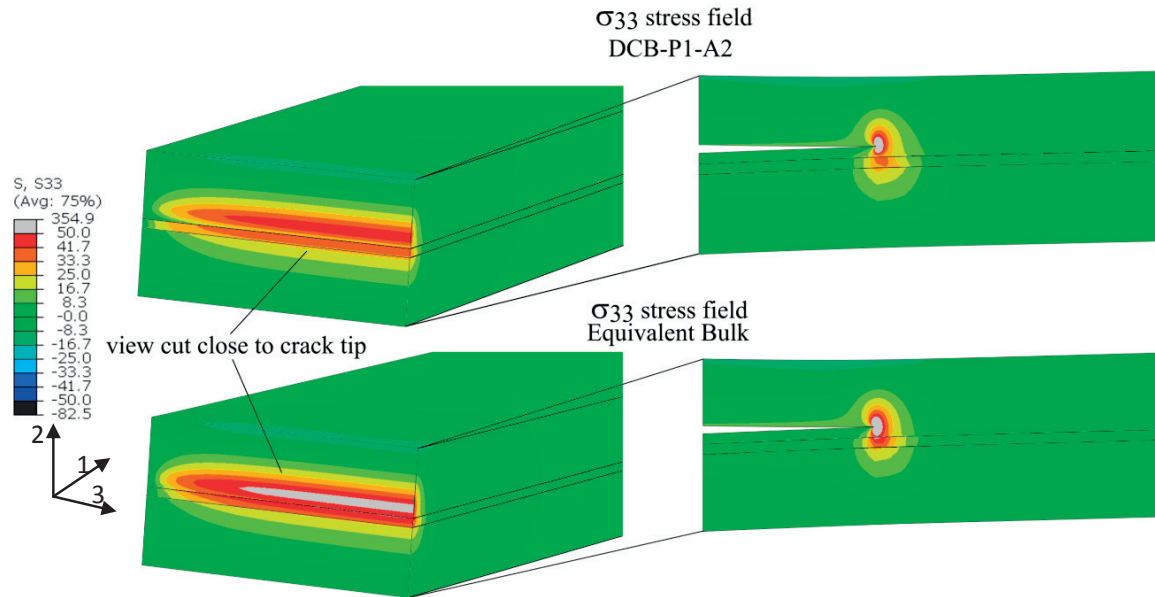
Figure 5.96: Stress field σ_{33} comparison from 3D FE Modeling with an applied displacement of 8mm. The stresses are in [MPa] , and the visible edge is the bulk side (symmetry plane).
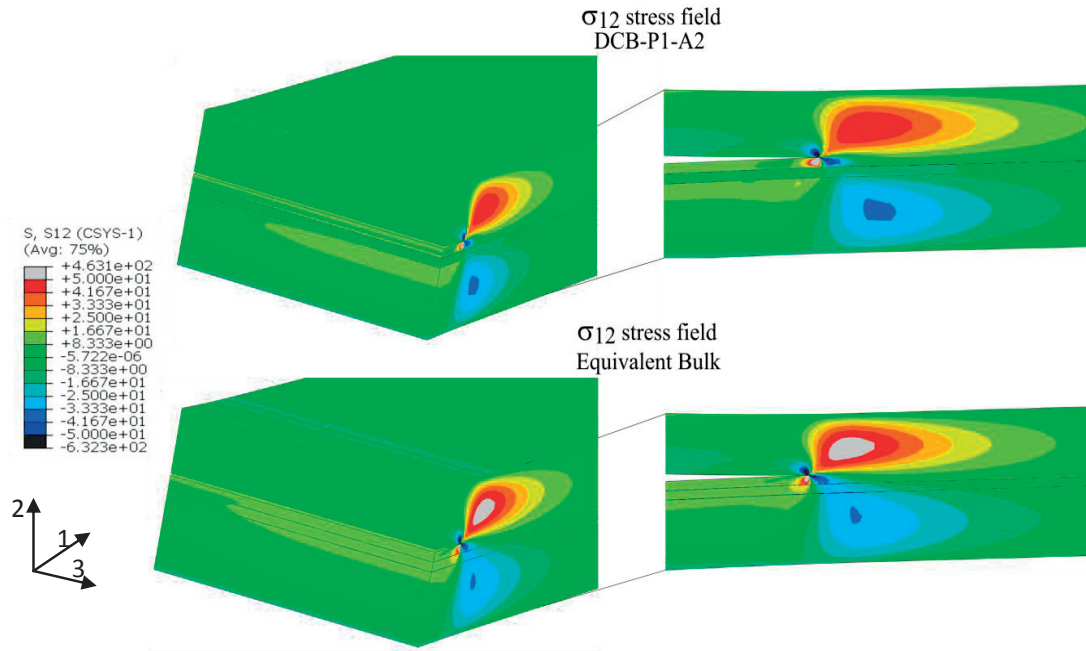
Figure 5.97 : Stress field σ_{12} comparison from 3D FE Modeling with an applied displacement of 8mm. The stresses are in [MPa], and the visible edge is the bulk side (symmetry plane).

Shear stresses

The extracted longitudinal-transverse shear stress related to a mode II component is represented in Figure 5.97. Similarly to the stress σ_{11}, the adhesive layer with adhesive properties acts like a shield, preventing the stresses from spreading continuously. It is also interesting to note that the shear stress distribution close to crack tip is significantly modified by the presence of the adhesive layer: the shear stresses are singular in a larger area in the Joint model compared to the Equivalent Bulk model.

The transverse-transverse shear stress σ_{23} is shown in Figure 5.98, with a view cut close to the crack tip. Those stresses only apply near to the specimens' free edge due to displacement discontinuity and free edge effects. Likewise, the shear stress concentration is much more pronounced in the case of Equivalent Bulk than joint due to the higher compliance of the adhesive layer.

Stresses extracted along specimens' free edge

Since there is a visible 3D effect on the stress repartition, the stresses are extracted from paths defined along specimens' free edge (see Figure 5.99) for both DCB2-P1-A2 and Equivalent Bulk model. Results show that there is no noticeable difference of stress field in the normal directions between a DCB2-P1-A2 specimen and an Equivalent Bulk specimen (see Figure 5.100) at the free edge. This is consistent with the results presented in the section 5.1.2 with 2D simulations: the presence of the adhesive layer does not influence the stress field around the crack tip on the specimens' free edge. Note that the results of the 3D stresses at the edge of the specimen are only qualitative due to the fact that the $\frac{1}{\sqrt{r}}$ singularity at the crack tip is not maintained.
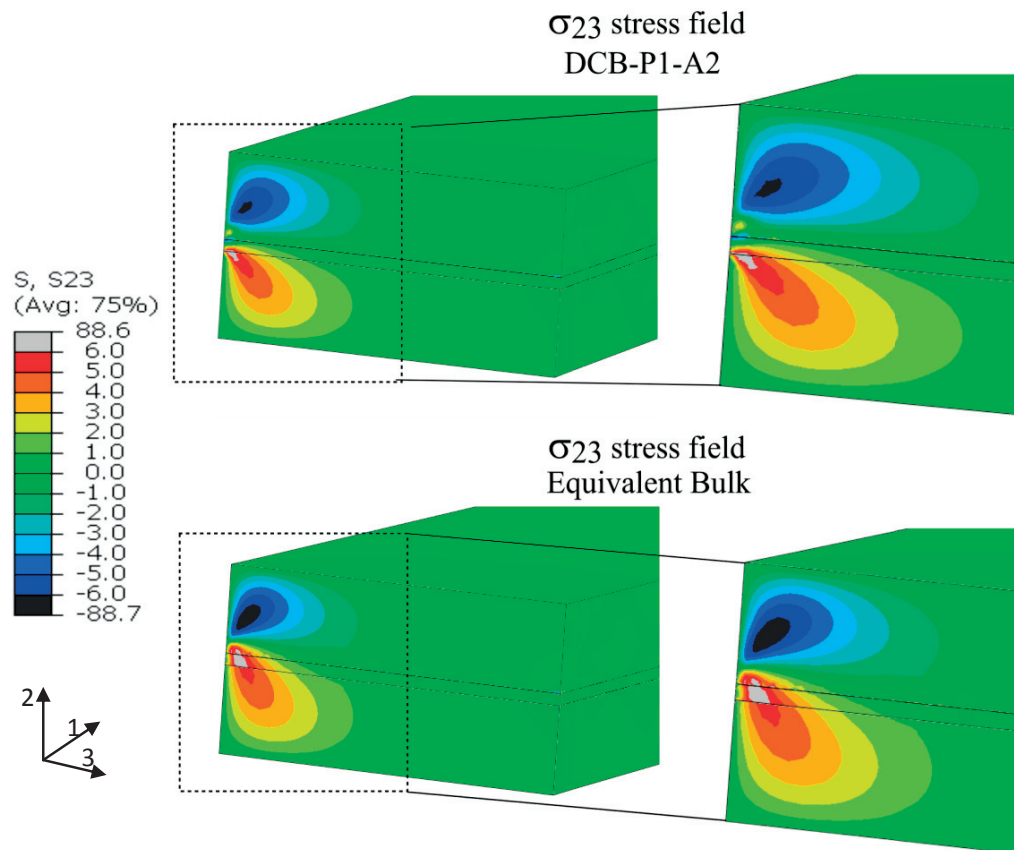
Figure 5.98: Stress field σ_{23} comparison from 3D FE Modeling with an applied displacement of 8mm. The stresses are in [MPa].
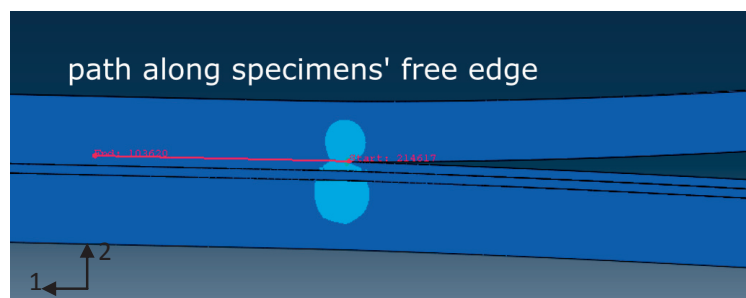
Figure 5.99: Path defined along specimens' free edge, in the crack plane in both 3D models. Stress fields are extracted along this path for analysis.

Stresses extracted in the middle of the specimen

Figure 5.101 shows the stress fields extracted from a path defined along the crack propagation on the symmetry plane of the 3D model, which corresponds to the middle of the specimen. In these plots, a non negligible difference can be distinguished between the joint specimen and the Equivalent Bulk one for all normal stresses, which leads to the conclusion that the adhesive layer properties also affect the local distribution of the stresses nearby the crack tip. The FE results show that the stress state in the close vicinity of the crack tip is affected by the presence of the adhesive.

Considering a point at 0.2mm distance ahead of the crack tip, which would be within the matrix cracking fracture process zone in a real specimen, the triaxial stress state in the Equivalent Bulk specimen is σ_{11}=825 MPa, σ_{22}= 129 MPa, σ_{33}=72 MPa in contrast to σ_{11}=843 MPa, σ_{22}= 110 MPa, σ_{33}=64 MPa for the joint specimen. Thus the presence of the adhesive layer induces, a small but noticeable change of +2.2% in axial stress, -14.7% in through the thickness normal stress and -11.1% in lateral normal stress in this region. Those results show that very locally, in a region close to the initiation of matrix cracking and fibre decohesion, the presence of the adhesive induces a significant change in the stress state in the composite: the presence of the adhesive reduces the transverse stresses by more than 10% and reduces the transverse to longitudinal stress ratio from 1/6.4 to 1/7.6. Potentially, these changes in local stress state in the region of damage initiation might trigger more significant changes in terms of micro scale damage initiation and distribution which could affect the further development of bridging bundles. However, this hypothesis would require more in depth evaluation by performing micro-scale FE simulations.

Summary

It can be concluded from the 3D modelling results that the elasto-plastic properties of the adhesive create a local perturbation of the stress fields around the crack tip. A shielding effect is even observed for some stresses such as σ_{11}, σ_{12}. The spatial repartition of stresses is affected both vertically and horizontally. The amplitude of the stresses, and more particularly close to the singularity, is affected by the adhesive layer properties. A local reduction of transverse normal stresses down to -14.7% is calculated in the presence of an adhesive layer in a region representative of the damage initiation zone.

The combined effects of all those changes in the neighbourhood of the crack tip are likely to create a different path for crack propagation, ending up with a different bridging behavior. Indeed the matrix cracking and interfacial debonding, that are the preliminary stages of delamination, can be affected by the different stress state ahead of the crack tip induced by the adhesive layer properties, leading to a path of delamination including many isolated fibres, but very few bundles of fibres participating to bridging. However, those damage mechanisms occur at the microscale and a further investigation at the micromechanics level is necessary to assess the influence of the adhesive on the formation of bundles of fibres.
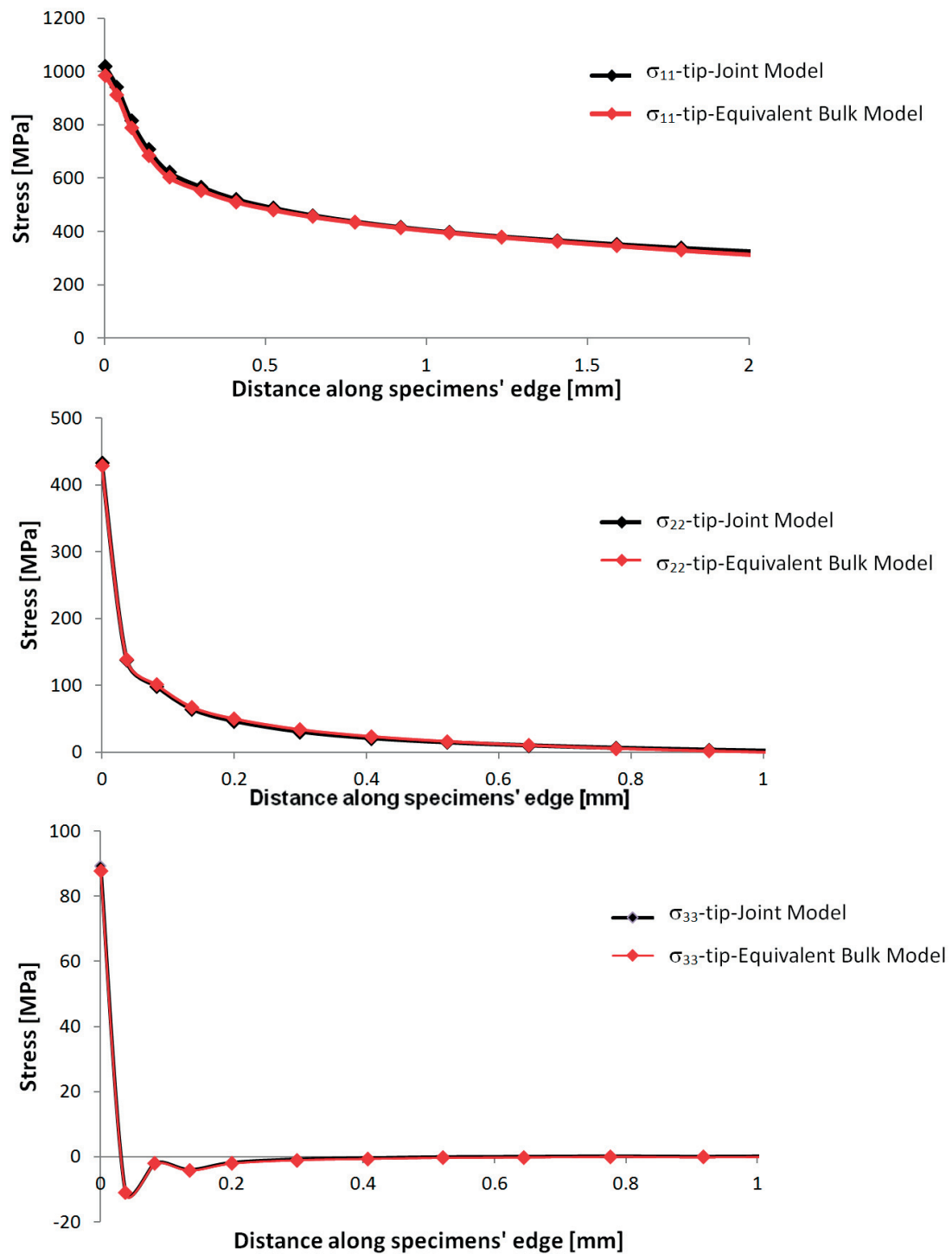
Figure 5.100: Stress fields in normal directions extracted along specimen's free edge from DCB2-P1-A2 3D model, and the Equivalent Bulk model.
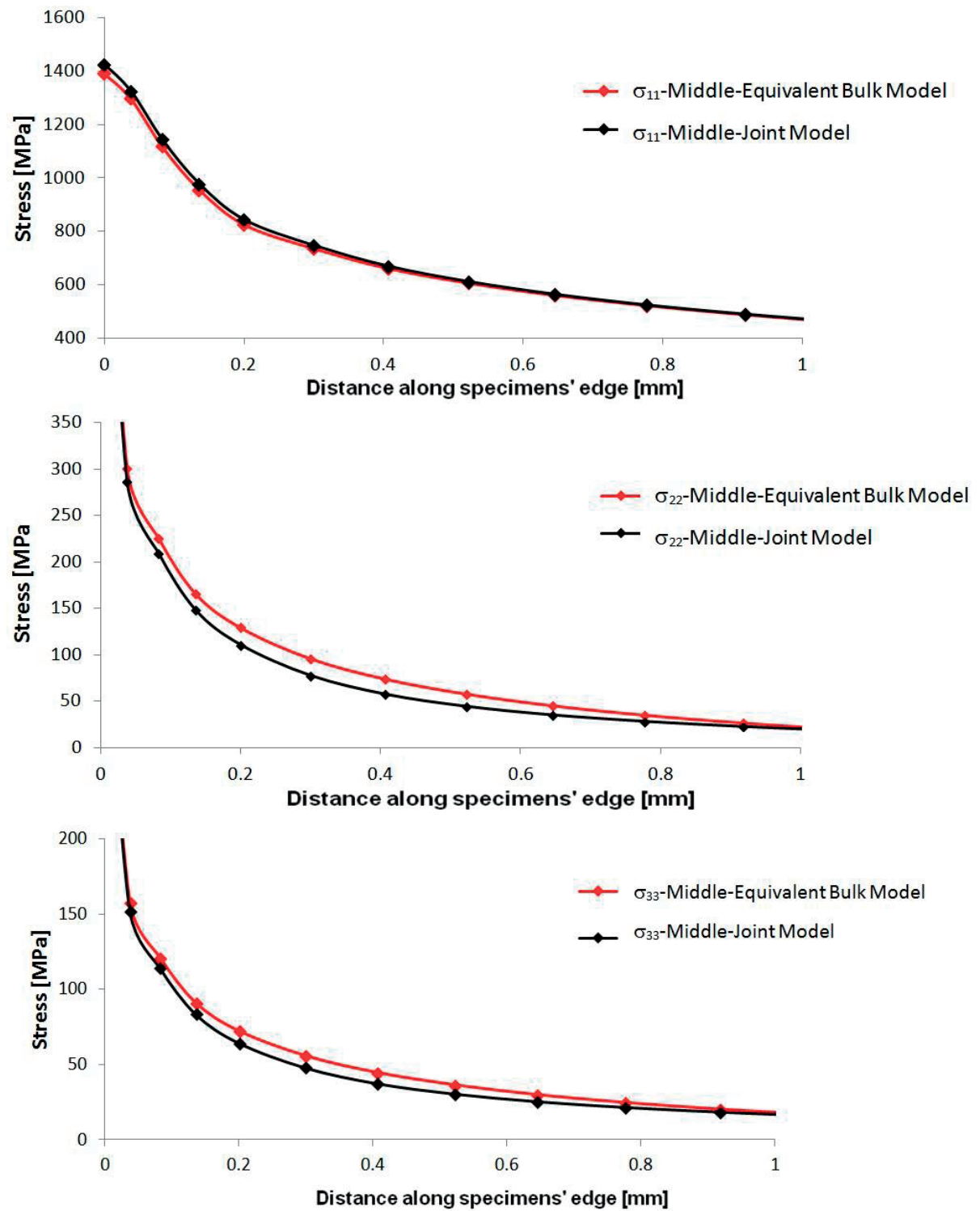
Figure 5.101 : Stress fields in normal directions extracted along crack plane in the middle of the specimens model from DCB2-P1-A2 3D model, and the Equivalent Bulk model.

Conclusion

Fracture behavior of asymmetric unidirectional CFRP laminate is numerically analysed with and without the presence of an adhesive layer close to the crack plane, aiming to find an explanation for the lower amount of fibre bridging observed with bonded joints specimens.

The mode II component assessed using the numerical method VCCT is negligible for the configurations experimentally tested, and thus the mode mixity is not responsible for weaker fibre bridging observed with bonded joints. Those results are consistent with the experimental DIC measurements presented in section 4.2.3. The 2D models at initiation show that the adhesive layer is submitted to a stress sufficient to induce plasticity. However results show that the non linear behavior of the adhesive does not significantly affect the stress fields nearby the tip, hence it cannot explain the difference of delamination behavior between joint and bulk specimens.

The bridging laws for both DCB2-P1-B and DCB2-P1-A1 configurations are identified and exhibit significantly different bridging parameters. It is assessed, thanks to the modified bridging scaling function, that the difference of compliance between the specimens with a bond layer (both A1 or A2) and DCB2-P1-B does not explain the difference of delamination behavior. The identification method is used to find the traction separation law describing the bridging of DCB2-P1-A1 joint specimens configuration, which is implemented in a cohesive elements model, and is found to successfully predict the experimental loading response and crack growth. This method is hence of interest for prediction purposes of both bulk and joint delamination behavior. An energetic analysis extracted from the cohesive elements model showed that the energy dissipated by plastic deformation of the adhesive layer is negligible compared to other mechanisms such as damage. Thus, the ductile behavior of the adhesive layer cannot energetically explain the change of toughness properties of the composite.

3D simulations of a DCB2-P1-A2 specimen are analysed and compared with a 3D model with the exact same geometry but with only CFRP properties. The adhesive layer with adhesive properties acts like a shield, preventing stresses from spreading continuously. The spatial repartition of normal stresses is affected horizontally, along fibre direction, and vertically, through the thickness, by the adhesive layer properties. Moreover, the intensity of shear stresses in the process zone is substantially affected by the compliant adhesive layer. The difference of bridging behavior between joint and bulk specimens can therefore be attributed, at least in part, to the decrease of intensity and change in distribution of the stress field around the crack tip due to the presence of the adhesive layer. The detailed sequence of damage mechanism leading to a different development of microscale damages and a different statistics of bridging ligaments remain to be explained. However, this study clearly demonstrates that the initial conditions prevailing at the start of that complex, stochastic sequence of damage process are indeed different when an adhesive layer is present. Further investigations at the micromechanics level would be necessary to further understand the underlying mechanisms.

Chapter 6: Mechanistic investigations at the microscopic scale

The macroscopic properties of a laminate highly depend on the microstructure: its stiffness depends on the average volume fraction of fibres and its strength can be reduced significantly with increasing heterogeneity of fibre distribution. Therefore it is crucial to consider relevant microstructural features to predict the fracture behavior of a composite. Moreover, the effective fracture properties of a heterogeneous material such as a UD laminate depend on the complex interactions between the different phases and their interfaces. A compliant layer in the neighbourhood of the process zone might influence these interactions: the change of stress distribution due to an adhesive layer can modify the amplitude or the sequence of failure micromechanisms, and generate a different bridging behavior.

In this work, the microscopic characteristics such as the fractured surface roughness and the variations of fibre volume fraction within the plies of the composite are investigated. Subsequently the influence of a compliant glue layer close to the process zone on the onset of damage is highlighted by a multiscale FE-model that takes into account micromechanisms such as interface decohesion between fibres and matrix, and yielding and damage of the epoxy matrix for a strain state equivalent to a mode I delamination.

6.1 Influence of the heterogeneity of the microstructure

Delamination is initiated by transverse cracking, which is known to start in regions with high fibre volume fraction [41]. It was shown in the previous chapters that DCB2-P1-B specimens' delamination behavior can be considered identical to the one of symmetric DCB specimens of the same thickness and made of the same prepreg material. However a different manufacturing process of the prepreg can lead to a laminate with a different microstructure. Indeed the extent of heterogeneity of the microstructure can be affected, which might lead to a different ERR at steady state [45]. In order to determine the influence of heterogeneity of the microstructure on the development of bridging fibres and fibre bundles, the same prepreg material (SE70 by Gurit®) is produced with a different prepreg production line which yields a more homogeneous microstructure. The obtained composite is referred to in the nomenclature as P2 (to distinguish it from the more heterogeneous composite P1). Mode I Delamination tests are carried out on symmetric DCB specimens made of P2, and on asymmetric bonded joints DCB2-P2-A2, and then compared with specimens made of P1. The considered features to compare P1 specimens with P2 specimens are the load-displacement response and R-curves, the crack path in transverse direction, and the roughness of the fractured surface.

6.1.1 Assessment of the difference of microstructure

Laminates of both P1 and P2 materials are fabricated by hand lay up of the prepreg sheets and cured in autoclave using the same procedure (see section 2.3). In order to verify the quality of the fabrication (low porosity) and also to compare the microstructure of composites P1 and P2, transverse sections of each are observed with an optical microscope (see Figure 6.102). These micrographs show that the microstructure is significantly different between the two materials:

- The succession of plies and resin rich regions is extremely regular for P2: each ply is clearly delimited from another with a zone with low fibre content. This is not the case in P1, where the interface between plies is less clear.
- The stacking is flat in the case of P2: plies are straight whereas P1 composite exhibit a significant ply waviness
- Many resin rich regions are present within the plies of P1 in the entire specimen. Fibres clustering are apparent all over the specimen. Thus high heterogeneity of fibre volume fraction is a key feature of P1. On the contrary, the local fibre volume fraction seems to be fairly constant within the plies of P2, thus P2 has a clearly more uniform fibre distribution with only limited resin rich regions within plies and only limited fibre clustering visible.

Therefore it can be ascertained that, on all aspects, the composite P2 is much more homogeneous than the composite P1.
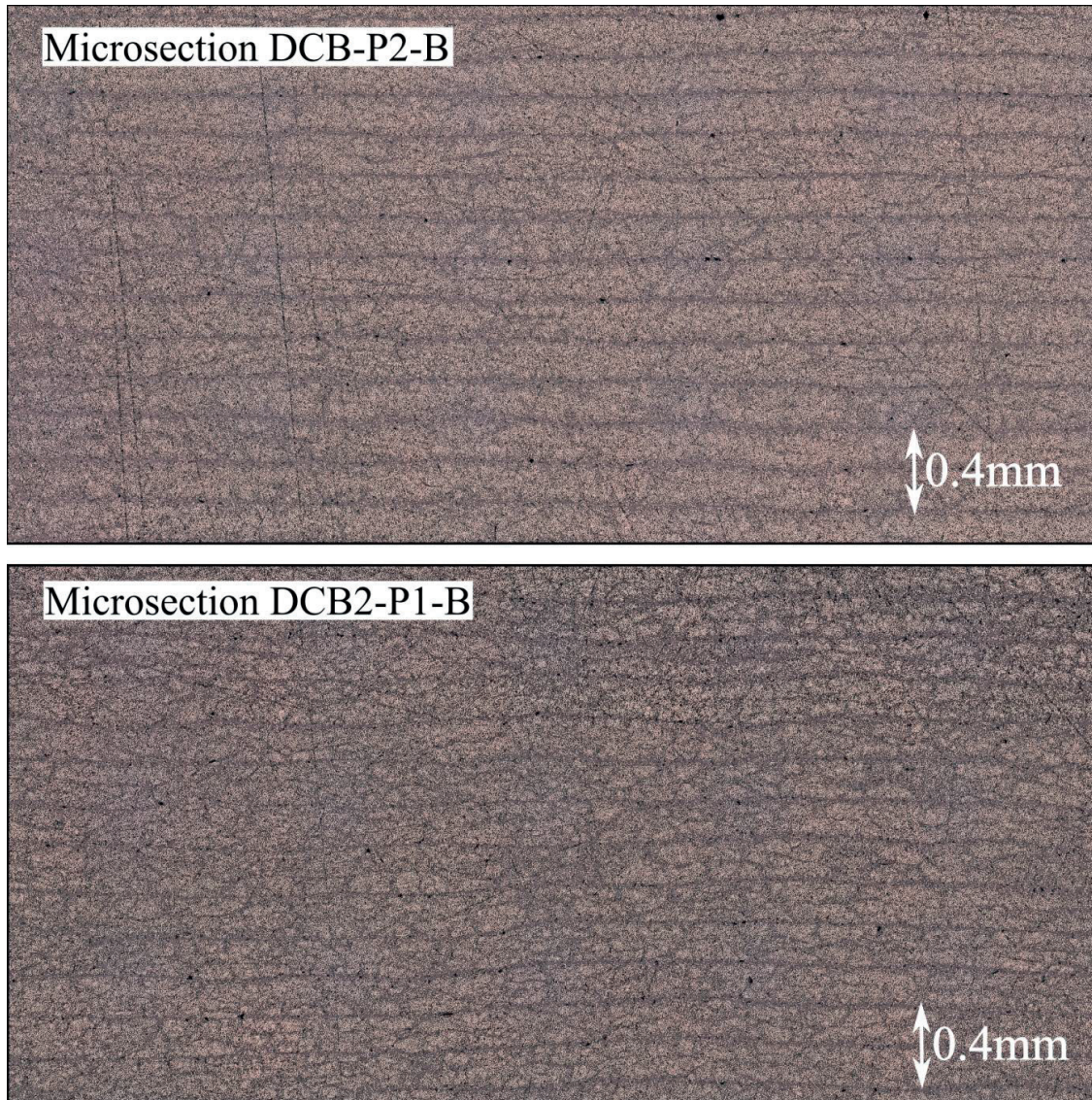
Figure 6.102: Micrographs showing the difference of microstructure between composites P1 and P2

6.1.2 Bulk symmetric DCB specimens

A total of 5 symmetric DCB specimens made of bulk composite P2 (referred to as DCB-P2-B) are tested under mode I delamination with the same testing conditions as specimens made of P1. The load displacement and calculated R-curves for each configuration DCB2-P1-B and DCB-P2-B are shown in Figure 6.103 and Figure 6.104, respectively, in which the curves correspond to the mean value of the batch and error bars represent the standard deviation.

It can be observed that both composites exhibit the same fracture toughness at initiation: about 300 J/m^2, but have very different R-curve effects: a very small amount of bridging is noticed in P2 laminates (G_b ~100 J/m^2). A similar effect of significantly reduced bridging intensity has been reported recently by Frossard *et al.* 2016 [45]: thin-ply composites exhibited a nearly suppressed

fibre bridging effect and the magnitude of the bridging contribution to ERR was shown to be correlated with the heterogeneity of the microstructure.
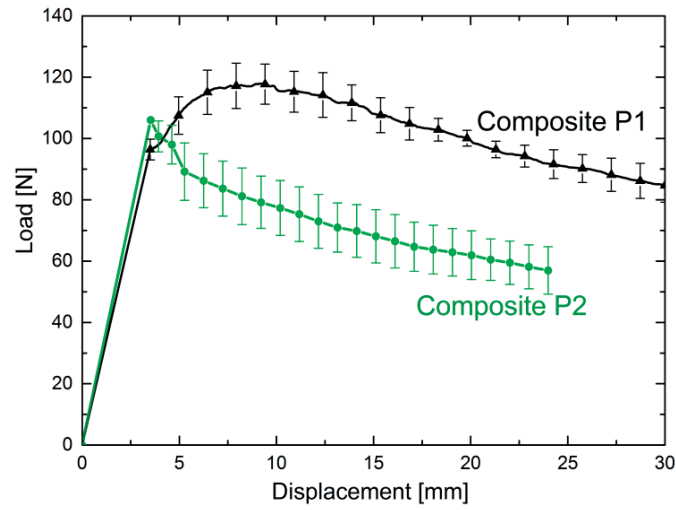
Figure 6.103: Experimental load displacement curves of Composite P1 (configuration DCB2-P1-B) and Composite P2 (configuration DCB-P2-B).
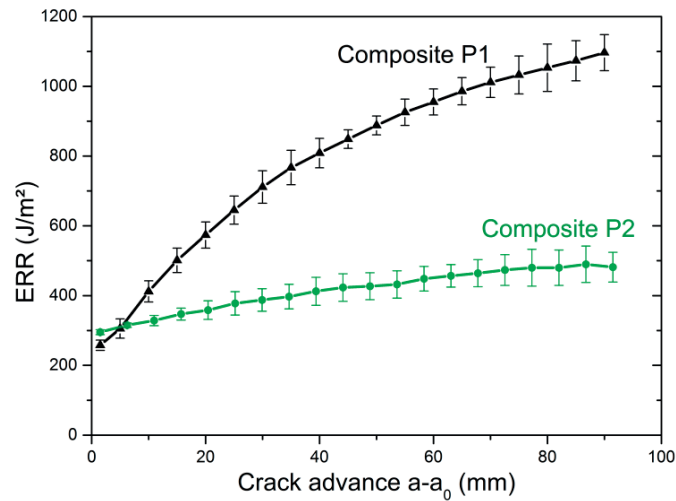
Figure 6.104: Experimental R-curves of Composite P1 (configuration DCB2-P1-B) and Composite P2 (configuration DCB-P2-B).

This difference of behavior might be attributed to:

Compaction

A different degree of compaction of the composites might explain this contrast, thus the consolidated ply thickness is measured, and is found to be exactly the same for both composites (193 micron per ply in average). Moreover, no noticeable difference is found in the results from different batches for different compactions (from 188 to 197 microns). The fibre areal weight being equal according to the supplier, it is thus expected that the final average volume fraction is comparable.

Curing state

Both prepreg are submitted to the same curing cycles and DSC measurements (see Appendix 2) show that the degree of cure is the same for both composites (similar residual enthalpy of reaction). Moreover, the DSC analysis shows that both composites are fully cured as expected.

By elimination of all other potential parameters, the difference of delamination behavior is thus mostly attributed to the change of microstructure in terms of fibre distribution heterogeneity and ply waviness.

6.1.3 Asymmetric bonded joints specimens

Two DCB2-P2-A2 joint specimens are fabricated and delaminated with the same conditions as specimens made of P1 composite. The load displacement and ERR curves are shown in Figure 6.105 and Figure 6.106, respectively, along with DCB2-P1-A2 curves for comparison. Since the reproducibility is satisfying (very small scatter), the results from the 2 tested specimens are considered representative of the material delamination behavior. Similarly to bulk specimens, the bonded joints made of P2 material exhibit the same fracture toughness at initiation and a very limited R-curve behavior implying a small amount of bridging. This result is expected since the bulk specimens made of P2 do not show much bridging either (see Figure 6.104). A comparative perspective of Figure 6.104 and Figure 6.106 shows that the difference of microstructure between P1 and P2 has a much stronger effect on the level of fibre bridging than the presence of the adhesive. It proves how importantly the microstructure, and by extension the microscale damage mechanisms, can influence the development of fibre bridging bundles in the wake of the crack front.
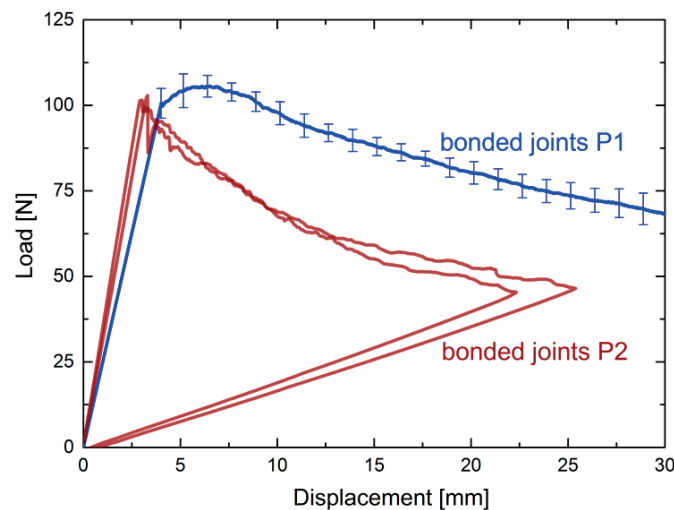
Figure 6.105: Experimental load displacement curves of bonded joints P1 (DCB2-P1-A2) and bonded joints P2 (DCB2-P2-A2). All specimens are bonded with the adhesive A2.
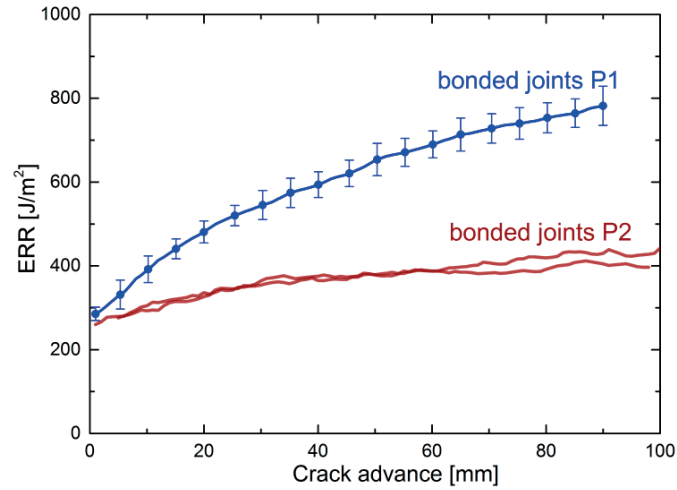
Figure 6.106: Experimental R- curves of bonded joints P1 (DCB2-P1-A2) and bonded joints P2 (DCB2-P2-A2). All specimens are bonded with the adhesive A2.

In order to determine if there is still a contrast of delamination behavior between bulk and joint specimens made of P2, the loading response and ERR curves are compared (see Figure 6.107 and Figure 6.108). The initiation ERR are similar, whereas a small reduction of ERR at steady state is observed in the joint specimens, which is compatible with previous findings. However, with such a small amount of bridging, the difference is close to the scatter level.
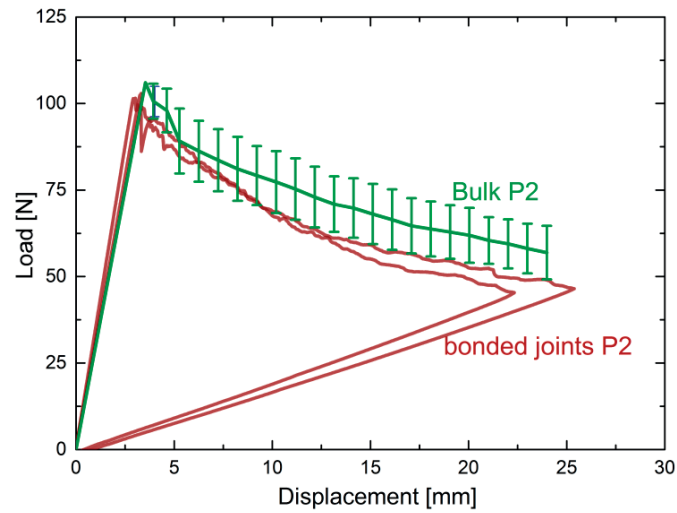
Figure 6.107: Experimental load displacement curves of DCB-P2-B (Bulk P2) and DCB2-P2-A2(bonded joints P2).
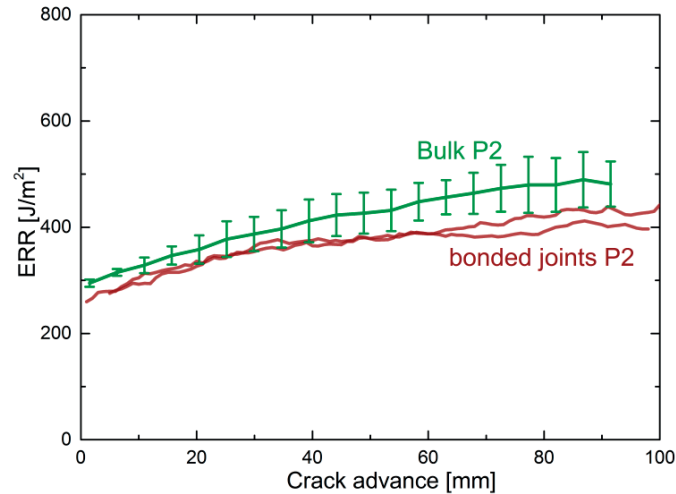
Figure 6.108: Experimental R-curves of DCB-P2-B and DCB2-P2-A2.

6.1.4 Comparison of fractured surfaces

During mode I delamination, bridging comes along with pulled out fibres that stay out of the crack plane after testing, resulting in a 3-dimensional fractured surface. A substantial amount of bridging is likely to result in a highly rough delaminated area, with broken fibres and bundles springing from the surface of the crack plane or grooves left after a bundle has been pulled out. Therefore, it is relevant to observe the morphology of the fractured surface of specimens after complete delamination. Delaminated surfaces of DCB2-P1-B and DCB-P2-B are observed with a Keyence VHX optical microscope, using the 3D reconstruction tool, which allows obtaining the precise topography of the region of interest.

The comparison between P1 and P2 specimens' fractured surfaces are performed in the region of steady state (60 mm from precrack). The considered area dimensions are 10mm x 25mm, which correspond to the whole width and 10mm in length. The resulting topography for both specimens' delaminated surface is shown in Figure 6.109. The maximum peaks, which represent pulled out fibres and bundles, are about 3 times higher for a bulk specimen made of P1 compared to a P2 bulk specimen. Moreover, the colour scales show that the average elevation with respect to the deepest details is about 1.2mm in P1 bulk specimens, thus 6 times higher than in P2 bulk specimens (~0.21mm of average height). This means that nearly no pulled out fibres/bundles are visible in the delaminated surface of P2 laminates, whereas the fractured surface of P1 laminates is covered with pulled out fibres/bundles. This can be correlated with the very different amounts of bridging participating to the materials respective toughness: low ERR at steady state due to small amount of bridging results in few pulled out fibres in the delaminated surface, and vice-versa.

In order to compare the roughness of the observed surfaces, the heights profiles are measured on 20 lines across the width of the considered area for both P1 and P2 specimens. The peak heights are suppressed from all profiles since they are due to pulled out fibres, and can distort the measure of the roughness.

105
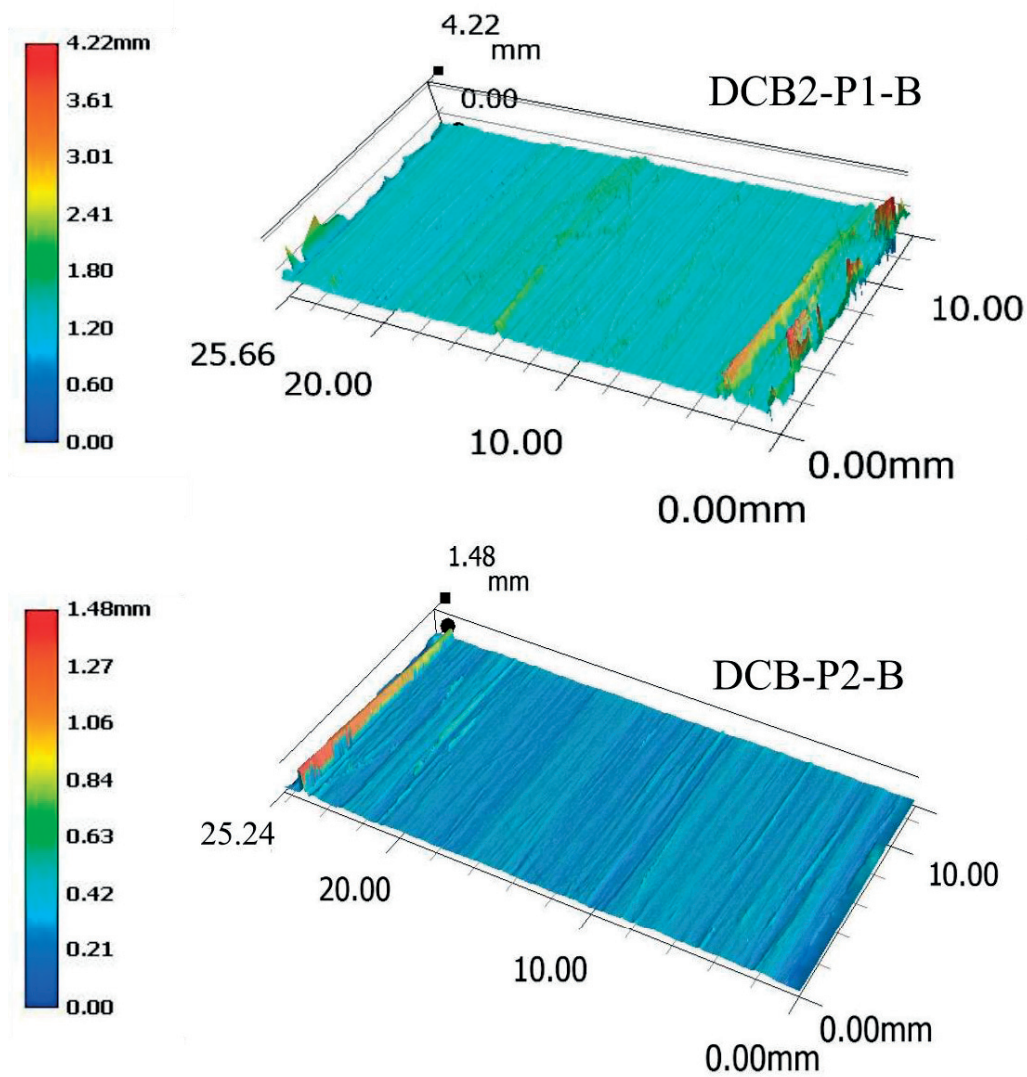
Figure 6.109: Topography of the delaminated surface in the steady state region for a DCB2-P1-B and a DCB-P2-B specimens.

The obtained average height profiles are shown in Figure 6.110. It can be noticed that for both specimens, the values oscillate around 0.2mm (one ply thickness), which can be considered as the mean crack plane surface. The oscillations are much more abundant, and their amplitude is higher in the case of P1 composite compared to P2. Assuming that the more variations of heights the larger degree of roughness, it can be concluded that the fractured surface is significantly smoother in P2 than in P1 specimens. This increased crack plane roughness follows thus the same trend as the observed fibre volume fraction heterogeneity and ply waviness.
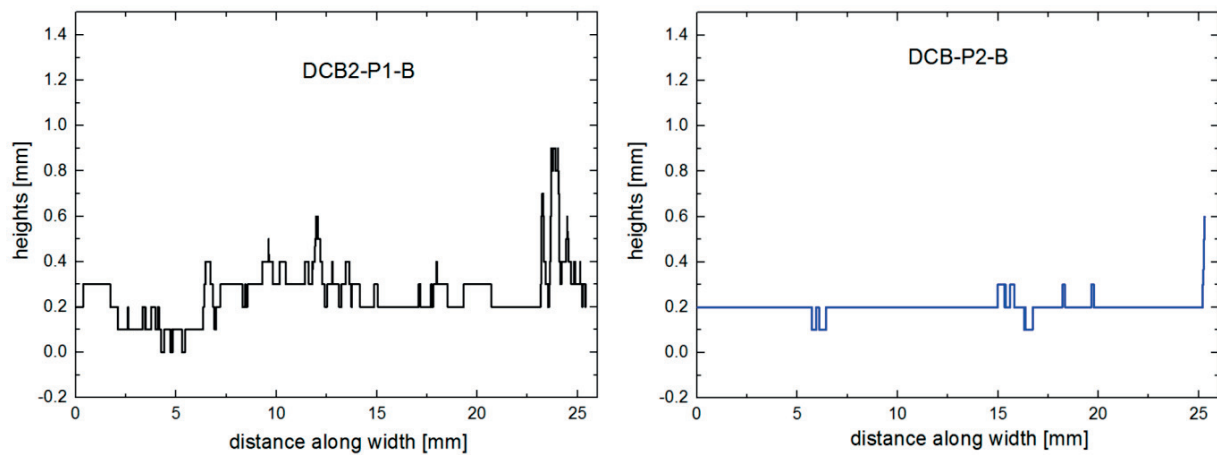
Figure 6.110: Average height profiles of the delaminated surface in the steady state region for a DCB2-P1-B and a DCB-P2-B specimens. Peak heights corresponding to pulled out fibres are not taken into account.

6.1.5 Comparison of transverse sections at the crack tip

The degree of roughness of fractured surfaces is a good indicator of the tortuosity of the transverse crack path during delamination: a rougher surface along the width can be correlated to a wavy crack path, which is more prone to involve more fibres and bundles in bridging during crack growth. Indeed, it is assumed that large bridging fibre bundles are created by the coalescence of offset microcracks as described in the schematic in Figure 6.111.
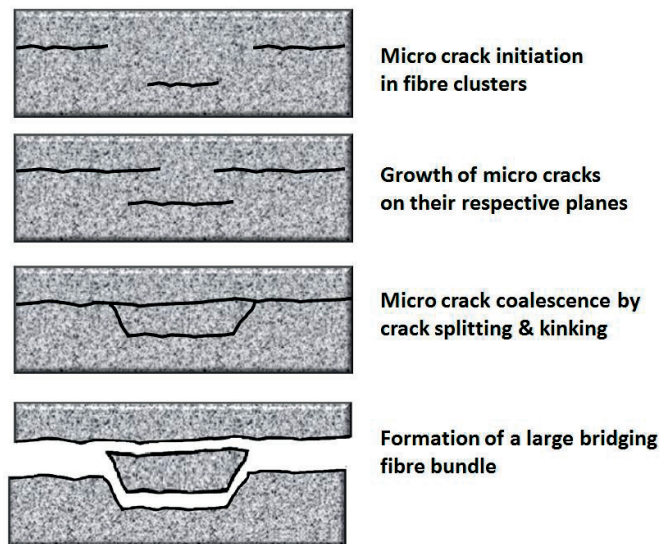
Figure 6.111: Potential formation process of large bridging fibre bundles by interaction and coalescence of offset microcracks and unstable crack front (vertical fluctuation of crack plane).

In order to investigate this hypothesis, and also to relate the crack profile to the microstructure, transverse sections are taken at the position of the visible crack tip for both DCB2-P1-B and DCB-P2-B specimens, polished and observed with a Keyence VHX microscope, with a magnification 200x, over the half width of each specimen. The obtained pictures are shown in Figure 6.112 and Figure 6.113.

107

Firstly, it can be observed that the porosity is very low in both composites, which indicates a good manufacturing quality.

Several important differences are noticed:

- In the heterogeneous composite (P1), the ply waviness is significant but the crack "stays" within the same ply over the entire width. Moreover the crack profile is relatively rough; indeed the crack goes up and down within the ply, with many micro-kinks, which is consistent with the previous observations made from the top.
- On the contrary, in the homogeneous composite P2, the crack path jumps from one ply to the other about 8 times along the width (only half is displayed). Crack profile remains relatively smooth and straight (low roughness) between two jumps, which is also in agreement with previous finding from the topography observations.
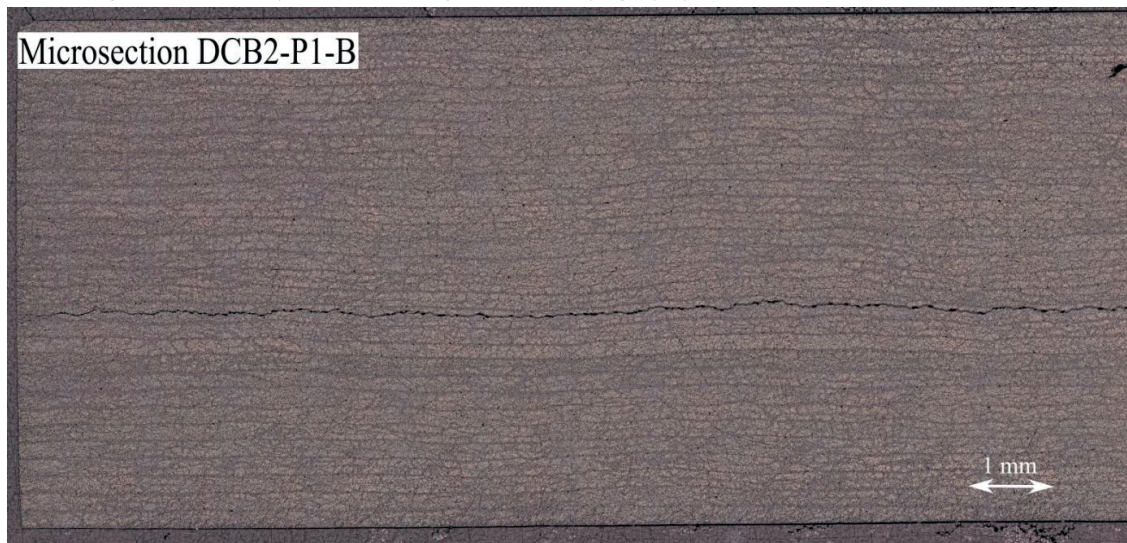
Figure 6.112: P1 composite micrograph from transverse section at the crack tip visible on the DCB2-P1-B specimen's edge. Half of the width is displayed.
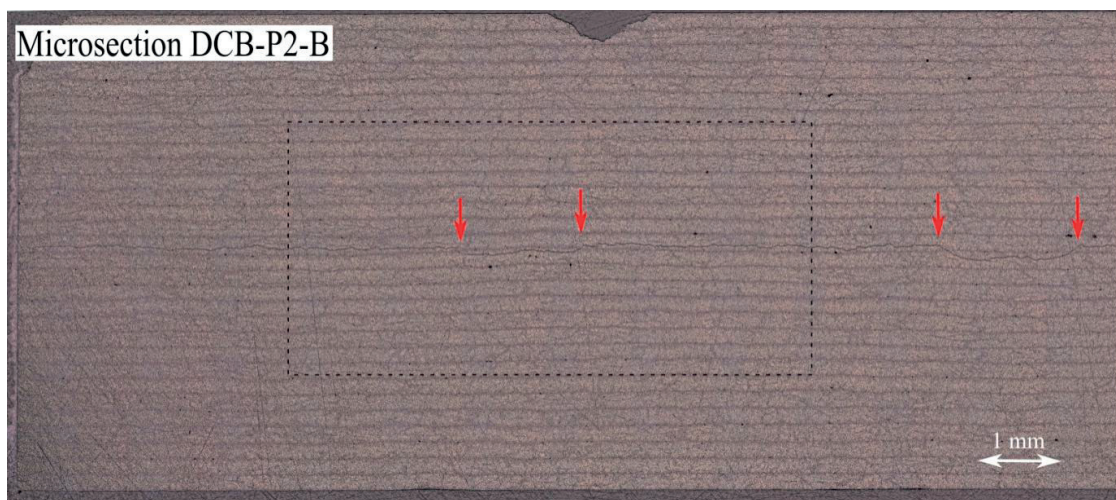
Figure 6.113: P2 composite micrograph from transverse section at the crack tip visible on the DCB-P2-B specimen's edge. Half of the width is displayed. The red arrows indicate the crack kinking. The rectangle indicates the area zoomed in Figure 6.114.

In order to compare the fibre and matrix distribution and the morphology and location of the crack paths, both pictures are enlarged in Figure 6.114 and Figure 6.115 to highlight a representative area.

Figure 6.114: P1 composite micrograph zoomed in.
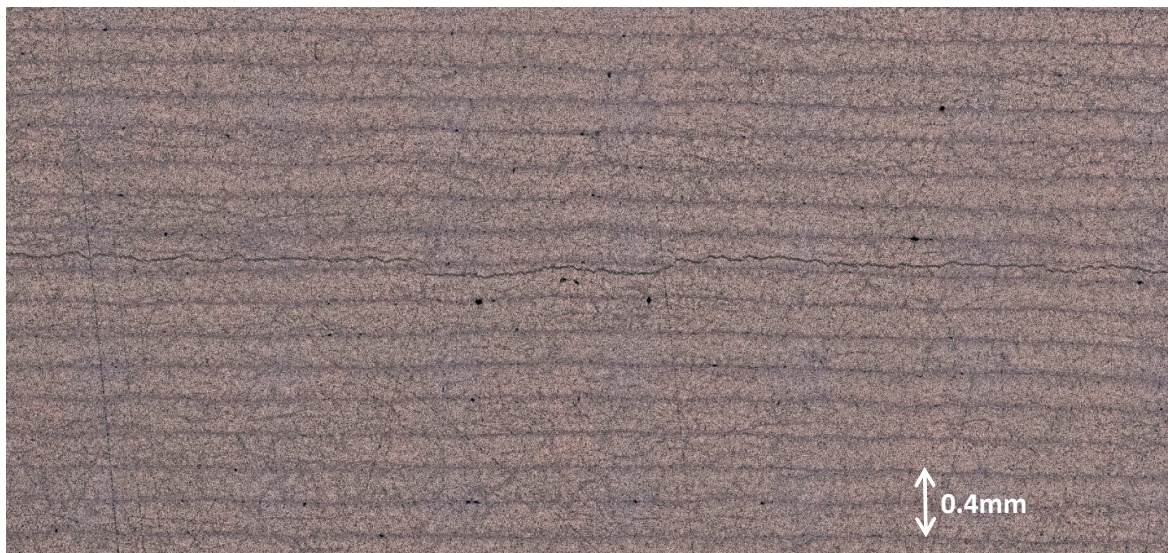
Figure 6.115: P2 composite micrograph zoomed in.

Aside from confirming the difference of microstructure heterogeneity and the roughness of the crack profiles, these detailed views allow to make the following observations:

- In the P1 composite, the resin rich regions are spread all over the specimen, resulting in a nodular fibre arrangement within each ply: clusters of fibres are separated by resin rich zones. Interestingly, the crack does not propagate in the resin rich regions but seems to follow regions of high fibre volume fraction. As those fibres-packed regions are spread apart the crack surface develops a significant roughness. It should also be noted that the increased ply waviness also contributes to the development of an unstable crack front.

- On the contrary, only a small number of resin rich zones within plies is observed in the P2 composite. The fibre distribution within ply is significantly different from P1: very homogeneous, with no visible nodular/ bundles arrangement. Moreover, the crack profile remains fairly flat between two jumps and the crack sharply kinks to neighbour plies a few times along the width. The only similarity with P1 composite is that the crack propagates preferentially in the regions of closely packed fibres (high fibre volume fraction in the middle of the ply here) and never propagates in resin rich zones (for example at ply interfaces).

Overall, three key features are analysed:
- **The crack propagation behavior**: Clearly different crack propagation behaviors are observed between P1 and P2 composites: P1 shows a rough crack surface that remains within a single ply while P2 exhibit flat crack segments and jumps between plies. In both cases, the roughness of the observed crack profile in the cross section is consistent with the observed surface roughness observed from the top (see section 6.1.4).
- **The ply waviness:** Despite an identical manufacturing process of the composite, the ply waviness is significantly different: UD laminate of P1 shows significant waviness, and a substantial ply thickness variation whereas P2 does not show such effect; plies are straight and of uniform thickness.
- **Crack propagation vs microstructure:** A rough crack profile correlates with the high heterogeneity of fibre volume fraction within ply, whereas flatter crack profile is consistent with the more homogeneous fibre distribution; only a few jumps across interfaces are observed. In both cases, crack propagates in fibre rich regions and avoids resin rich zones. In the more heterogeneous structure (P1), more resin rich zones are present and seem to deviate crack front, which could explain the roughness of the crack profile.

Conclusion:

The processing induced variation of microstructure of the prepreg SE70 is investigated by comparing specimens made of two prepreg of similar composition but produced on different impregnation lines. Significant differences are observed in the fracture tests between the delivered materials P1 and P2: a very limited amount of fibre bridging takes place during crack growth for the more homogeneous composite P2. A clear link is established between the extent of bridging and the microstructural features: more homogeneous fibre distribution leads to a smoother crack surface and less bridging. These results are consistent with the effects observed in by [45]. Moreover, the analysis of the fracture surface morphology of delaminated specimens shows that the microstructures' heterogeneity also has an impact both in terms of roughness and of number of pulled out fibres: nearly no pulled out fibres/bundles are visible in the more homogeneous prepreg P2. This result is consistent with the conclusions of Canal *et al.*, 2012 [46]: as cracks preferentially initiate in fibre rich regions, the tortuosity of the crack is controlled by the spatial fibre and matrix distribution. The contrast of delamination behavior between joint and bulk specimens observed with P1 prepreg remains with P2 composite but it is close to the scatter. Moreover, the effect of the microstructure on the magnitude of fibre bridging is found prominent over the effect of the adhesive layer.

6.2 Multiscale model

The UD composites studied in this work often fail by accumulation of fracture events that eventually combine to cause a transverse fracture. Indeed a crack is developed by the coalescence of the voids issued from decohesion of the fibre/matrix interface and the fracture of the matrix ligaments between voids [46]. The mismatch of mechanical properties of the fibres and epoxy matrix causes early interfacial debonding, whereas the matrix cracking is mostly controlled by the following parameters:
- matrix constitutive response
- residual stresses
- fibre/matrix interface
- heterogeneity of the microstructure

Since it has been shown in section 4.1.3 that a postcuring process close to the curing temperature of the composite (70°C) does not affect the delamination behavior, and due to the low curing temperature used in this work (82°C), the residual stresses are assumed to have negligible effects in the studied case. The other mentioned phenomena are investigated by employing a multiscale FE simulation based on a real microstructure and realistic material properties representative of a generic carbon-epoxy composite. This model can give valuable insight of the influence of an adhesive layer on the damage mechanisms that may lead to different levels of fibre bridging.

6.2.1 Computational Model

In order to determine the influence of the adhesive layer on the failure micromechanisms that control the crack propagation, two 3D embedded cell multiscale FE models are built: one with a glue layer, the other without (homogenized composite layer instead). For clarity, the model with bulk composite is referred as Bulk model, and the model with an adhesive layer as Joint model. Each model is divided in 3 regions (see Figure 6.116): 2 regions with homogenized properties and between them, a microstructured region, where all the fracture process occurs. Regions are bound together with tie constraints, and the displacement field is continuous between all regions.
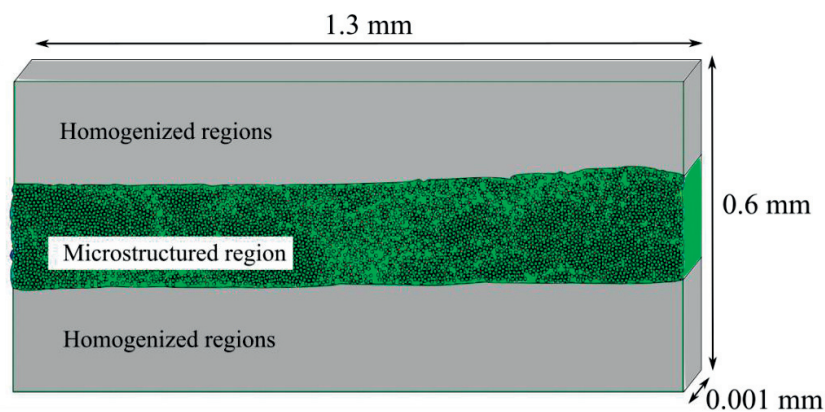
Figure 6.116: Schematic of the embedded cell 3D model

The thickness along the specimens' width of the investigated section (see Figure 6.116) is taken at 0.001mm to represent a small slice of the microstructure at a selected location ahead of crack tip.

6.2.2 Materials and interface properties definition

In the first model, both regions with homogenized material are assigned elastic bulk composite properties, (see table 2.1) whereas in the second model, the lower homogenized region is assumed to behave as the adhesive A1, whose elasto plastic properties were determined by dogbones testing and implemented as a Von-Mises isotropic hardening curve.

The microstructured region between the homogeneous layers is represented by circular carbon fibres Toray T700s (the same as in SE70) embedded in an 80°C curing epoxy matrix (NTPT TP80EP). The distribution of the fibres is taken from microscopic observations of a 150g/m^2 thin plies composite manufactured by NTPT® and where reconstructed by R. Amacher for his research at the laboratory. The carbon fibres Toray T700s are modelled with the anisotropic elastic properties described in Table 6.5. The elasto-plastic properties of the epoxy matrix are E=3.261GPa and v=0.35. Additionally, the epoxy matrix behaves according to a ductile Drucker-Prager plasticity model with a tensile hardening described in Table 6.6 which takes into account the sensitivity of the epoxy to hydrostatic pressure (compression), and its brittle behavior under triaxial tension. After a critical level of plastic strain is reached (function of triaxiality, see Table 6.7), the epoxy matrix fractures according to a linear decay cohesive law corresponding to a matrix toughness of 64 J/m^2.

E_{11} [GPa]	E_{22} [GPa]	E_{33} [GPa]	v_{12} [-]	v_{13} [-]	v_{23} [-]	G_{12} [GPa]	G_{13} [GPa]	G_{23} [GPa]
230	10	10	0.27	0.27	0.3	3.8	3.8	3.8

Table 6.5: Carbone fibres T700 properties (microstructured region).

Tensile yield stress [MPa]	Initiation Tension
40	0
60	0.0005

Table 6.6: Parameters in Drucker Prager hardening function.

Fracture strain	Stress triaxiality
0.25	-0.3333
0.0006	0
0.0006	0.3333
0.0006	1

Table 6.7: Ductile damage evolution defined in the FE model for the epoxy matrix in the microstructured region.

Finally, the fibre/matrix interface properties are modelled with a cohesive contact exhibiting the properties written in Table 6.8. The microstructure reconstruction in the embedded cell, as well as the resin and interface properties are taken from the work of Kohler *et al.* [47,55].

Interface Stiffness properties [MPa/mm]		
Knn	Kss	Ktt
20e7	40e7	40e7
Interface Strength properties [MPa]		
Normal Strength	Shear 1	Shear 2
40	60	60
Interface Toughness properties [J/m^2]		
7.5		
Stabilization viscosity coefficient		
0.001		

Table 6.8: Cohesive contact properties defined for the interface fibre/matrix in the embedded cell.

6.2.3 Boundary conditions

In order to apply a loading corresponding to a region representative of the damage initiation in Mode I delamination, the macroscopic stress field is extracted from the 3D model from section 5.3 at a distance of 0.2mm from the crack tip. The local stress state modelled here corresponds to a longitudinal stress of 800 MPa and transverse normal stress of 100 MPa and a lateral normal stress of 60 MPa. The stress state is then converted to a 3D macroscopic strain state using the compliance tensor of the UD composite.
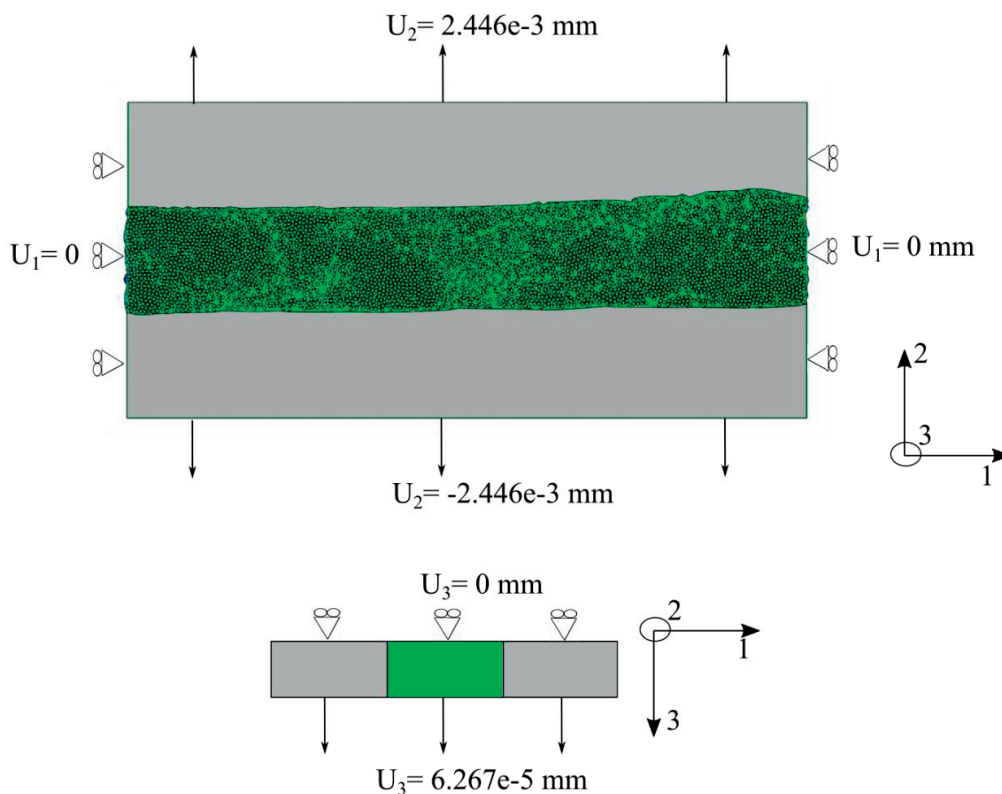
Figure 6.117: Boundary conditions applied to both multiscale FE Models.

The corresponding strain state corresponds to a plain strain conditions with a longitudinal strain of 0.63%, a transverse normal strain of 0.81% and zero lateral strain. On each face of the model, the displacement needed to induce the target strain field is applied (see Figure 6.117). Note that the same boundary conditions are applied to both multiscale models: the one with a glue layer, and the one with bulk composite.

Due to multiple instabilities generated during fibre-matrix debonding, the finite element problem is solved using Abaqus Explicit (dynamic explicit solver) with mass scaling adjusted to achieve a quasi static loading condition. Based on a convergence study for a similar case [47], the target critical time step was set to 5µs for a total simulation time of 1s, leading to a simulation requiring 2 million time steps. To limit dynamic effects, all boundary conditions are modulated over time by a smooth step function.

6.2.4 Results and discussion

First of all, the accuracy of the explicit simulations is assessed by verifying that the ratio of kinetic energy to external work is negligible in order to represent quasi-static fracture conditions. It is found that kinetic energy only represents about 0.2% of the total work up to the final failure, which is negligible.

Figure 6.118 shows the evolution of the damage dissipation energy during the simulation. It can be observed that the onset of damage appears earlier in the Bulk model than in the Joint model: as shown the damage starts at t=0.32, corresponding to a transverse strain of 0.2%, in the Bulk model and at t=0.38 , i.e 0.26% transverse strain in the Joint model. However, transverse fracture develops in both cases when a similar normal stress σ_{22}=40MPa is reached (see Figure 6.119).
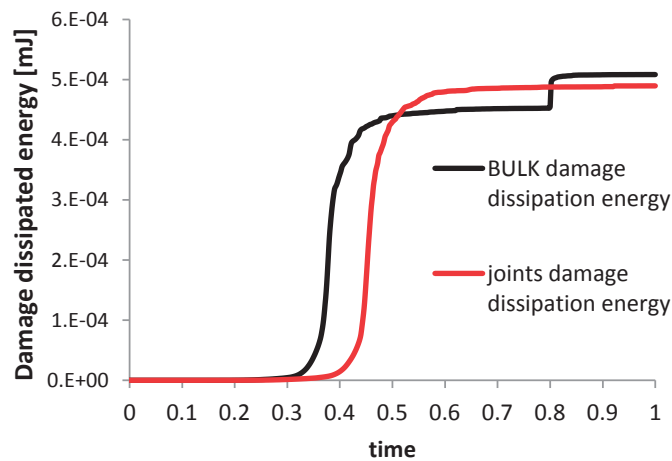
Figure 6.118: Damage dissipation energy as a function of time in multiscale models (with glue and without glue).

The difference in the applied strain at onset of fracture can simply be explained by the more compliant response of the elasto-plastic adhesive layer in the Joint model which requires a larger macroscopic strain to reach the critical transverse strength of the composite. However, it appears clearly that the transverse fracture initiates at a well defined transverse stress level of 40 MPa in all

cases and thus the in-situ transverse strength of the UD composite is not affected by the ductile adhesive layer.
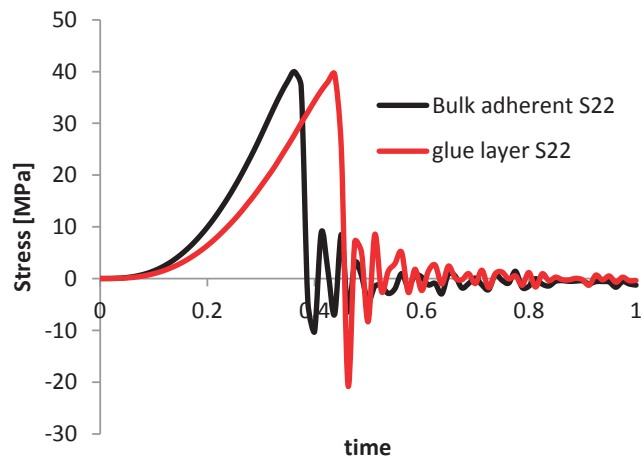
Figure 6.119: Stress field σ_{22} as a function of time comparison between Bulk Model and Joint Model. Data are extracted from one representative element in the microstructured region close to interface, and is found to be the same in the homogenized regions before onset of damage.
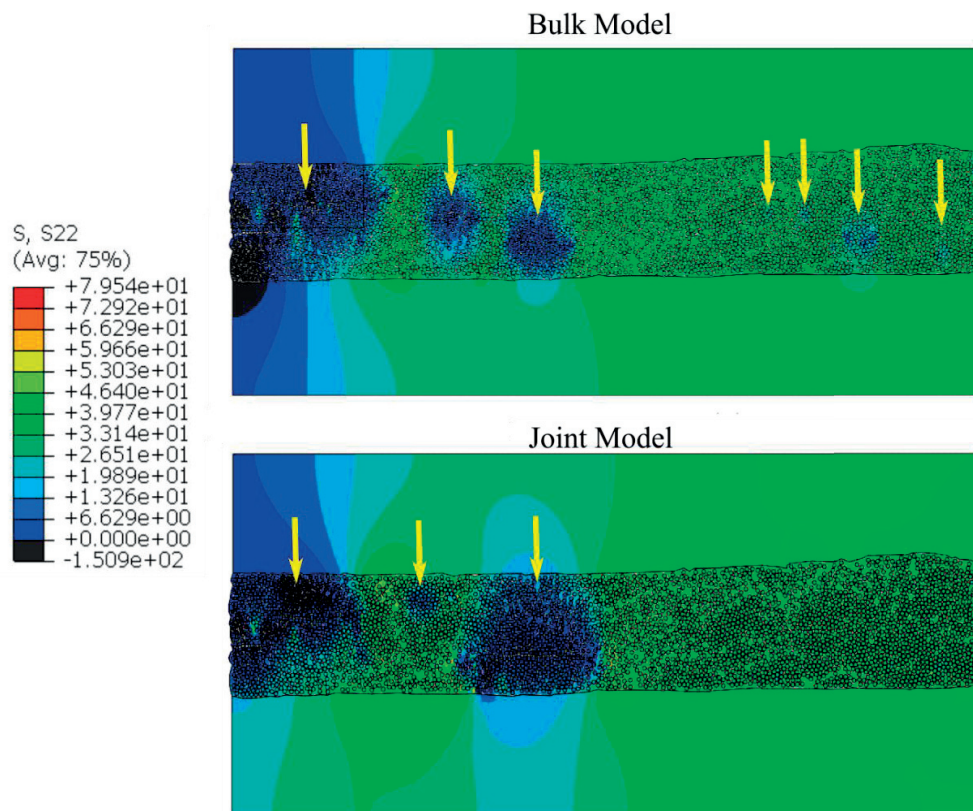
Figure 6.120: Stress field σ_{22} scale colour map for Bulk Model and Joint Model at the respective closest times after onset of damage. The blue areas indicate a complete unloading, subsequent to microcracking. All visible cracked areas are indicated by a yellow arrow.

115

The stress field σ_{22} right after onset of damage (defined as peak stress) is shown in Figure 6.120. Micro cracking can be observed in this figure by observing the unloaded regions surrounding microcracks, highlighted by yellow arrows. It can be observed that the micro cracking initiation is spread all over the simulated width in the Bulk model, and consists in a few large cracks combined on one side with a significant number of much smaller cracks on the other side. For the Joint Model, only a few large microcracks are observed, which stay localized on the left part of the model and thus represent a more compact region of damage initiation.

The stiffness degradation (damage) of the matrix is shown in Figure 6.121 for both models; which is a good indicator of the crack path. This view allows to notice that the fracture behavior is substantially changed by the presence of the adhesive. Indeed, in the Bulk model, the crack consists of many small damaged lines spread in different levels, still close to the middle, that eventually combine together (consistent with the mechanism described in Figure 6.111). It is also interesting to note that the final crack follows all the damage initiation sides identified previously. Thus, the more distributed microcracking initiation pattern observed in the Bulk model leads to a relatively rough crack path with multiple jumps in the thickness direction. The crack path in the Bulk model consists in approximately seven distinct segments corresponding to a density of 5.4 microcracks per mm which induce a relatively large number of discontinuities in the crack path (4.6 discontinuities per mm). On the other hand, the Joint Model presents an almost continuous crack, with only two main segments (1.5 microcrack per mm, ~1 discontinuity per mm) which develops relatively close to the borders of the ply. These significant differences can induce very different bridging behaviors between a joint and a bulk specimen.
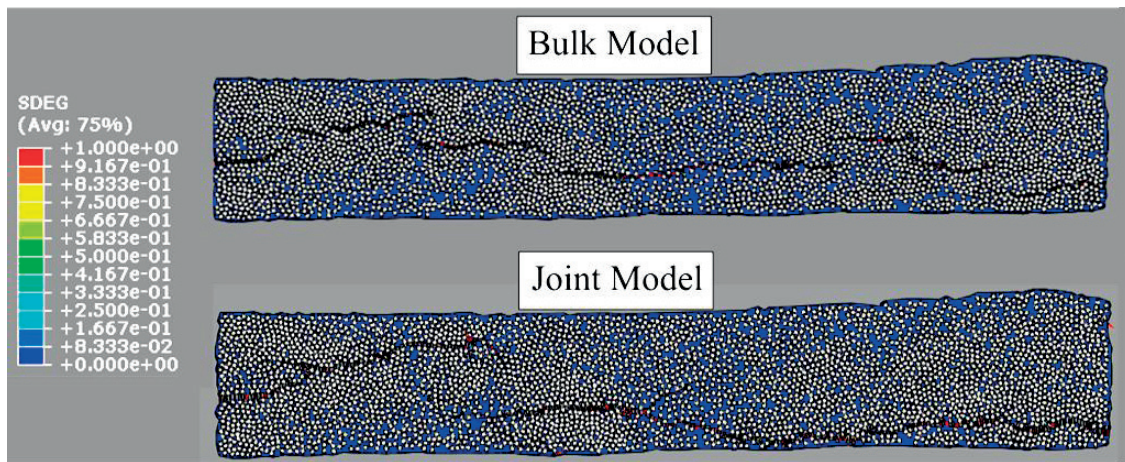
Figure 6.121: Matrix damage colour map for the Bulk model and the Joint model. Results are extracted shortly after onset of damage.

Embedded cells approach has demonstrated its ability to simulate the fracture behavior of heterogeneous materials in the literature [46,48] or to model quantitatively some complex phenomena such as the ply thickness effect on the onset of transverse cracking [47]. However, it is important to highlight the limitations of the present model:

- The limited dimensions and number of plies in the models only represent a small subset of a specimen, and therefore might not be fully statistically representative of the whole specimens' behavior. However, the model already includes more than 3700 fibres and interfaces which

correspond to about 150x the representative volume element, also called RVE (about 20-25 fibres per RVE). It is thus expected to be more than sufficient to represent the in-situ behavior of a ply up to transverse fracture onset. Moreover, as the model represents a real microstructure over a region covering about several times the cluster size, the model should be able to capture at least qualitatively the distribution of initial micro cracking sites and their coalescence.

- Since the development of bridging is a 3D phenomenon that involves several non trivial interactions at the microscale, the present model of a slice of microstructure is only representative of the early damage initiation and crack front formation but is not able to capture the development of potential fibre bundles after that point. A much larger volume of the composite material should be modelled to capture the development of bridging bundles such as in [43].

- Lastly, the microstructure and the fibre/matrix interface properties are taken from a different composite, which can obviously alter the quantitative prediction accuracy of the behavior of the considered material. However, the modelled ply thickness (both 200 μm), resin type (both 80°C curing prepreg) and fibre heterogeneity are all very similar for both materials and thus it is believed that the model is sufficiently representative of the reality to capture the main sequence of fracture mechanisms and give a qualitative understanding of the microscale fracture processes in the presence of an adhesive layer.

Despite a simplified representation, the micromechanical simulations are able to predict a significant difference in the pattern of microcracking at the onset of damage in the presence of an adhesive layer. Additionally, the crack path developed is also very different between the two models. Therefore, the embedded cell model is a powerful tool to investigate the influence of a joint on the micromechanics of damage of the composite and opens a way to explain the difference in the experimentally observed bridging.

Conclusion

A 3D-multiscale embedded cell modelling approach is employed to highlight the influence of an adhesive layer on the micromechanisms preceding fracture during a mode I loading. For given microstructure and material properties, the onset of damage is triggered later in the presence of a joint due to the more compliant response of the adhesive. Moreover, a different crack initiation pattern is created when the fracture is close to an adhesive layer: a more distributed cracking is observed in the bulk material than in the joint model. These differences in micro cracking initiation lead to a significantly more discontinuous crack profile propagating within the centre of the ply for the bulk composite while in the presence of an adhesive, the crack is much smoother with fewer discontinuities and it migrates towards the interfaces of the ply. These significative differences in the crack propagation morphology show that the adhesive layer has indeed a consequent influence on the early damage mechanisms responsible for development of bridging. Therefore, fracture behavior differences observed at the macroscale between bulk and joint specimens can be attributed, at least in part, to the changes of the repartition and amplitude of micromechanisms that triggers the formation of bridging fibre bundles in mode I delamination.

Summary

In this chapter, efforts are made to correlate the processing induced microstructure features to the bridging behavior during mode I delamination of UD CFRP laminates. It is demonstrated that the crack tends to grow in fibres-rich zones, and that a highly heterogeneous microstructure is likely to induce the development of large scale bridging, compared to a homogeneous one. It seems that the avoidance of resin rich regions by the crack is the main factor responsible for the tortuosity of the crack path. Moreover, a homogeneous microstructure annihilates the difference of delamination behavior observed so far between joint and bulk specimens. Moreover, analysis of fractographs show that a macroproperty such as the ERR at steady state is associated with the roughness of crack profile, and the number of pulled out fibres.

An embedded cell, multiscale FE model based on real microstructures and material properties showed that the presence of an adhesive layer close to the process zone induces a significantly different repartition of microdamages compared to a bulk specimen, which can lead to a considerably different global fracture behavior.

Chapter 7:
Conclusions and Perspectives

In this work, the mode I fracture behavior of asymmetric DCB unidirectional CFRP laminates is studied with and without the presence of an adhesive layer close to the crack plane. Using the data obtained from quasi-static tests, several numerical models are developed to understand the underlying mechanisms. Different analyses are carried out from the macro to the micro level in order to assess the influence of an adhesive layer on the delamination behavior of a UD composite.

In this chapter, the main conclusions of this work are summarized, followed by a concept map and some suggestions for future work.

Delamination of Asymmetric UD bulk composite specimens

The mode I delamination of asymmetric DCB specimens with the precrack positioned 2 plies from the midplane and no adhesive layer is analysed and compared with symmetric DCB specimens of the same thickness.

- Experiments show that the fracture toughness at initiation is not affected by the asymmetry, and its value is found consistent with the literature [18,21] for the same material.

- The measured ERR at steady state is in good agreement with the scaling reported in the reference work [21].

- An analysis based on a modified version of the thickness scaling function established by Farman-Ashtiani *et al.* [21] for the same material under the same testing conditions, shows that the difference of thickness between the upper arm and the lower arm of an asymmetric specimen has a negligible influence on the ERR at steady state compared to a symmetric specimen of the same thickness.

- The identified parameters of the bridging tractions relation are consistent with the values predicted by the thickness scaling function. This confirms that the effect of asymmetry (2 plies above central line) does not significantly affect the development of fibre bridging during crack propagation in bulk UD composites.

A strain monitoring by means of 2 optical fibres with FBG sensors is employed in an inverse identification method to assess bridging model at intermediate propagation states. The first optical fibre is placed in the transient state, where fibre bridging is not fully developed and the second optical fibre in the region where steady state is reached.

- A reliable, fast and simple procedure using a 4Point-Bending test on the delaminated part of the specimen with the optical fibres is used to correct the strains measured by the FBG sensors. This method gives an accurate strain distribution, and therefore could be implemented for any experiment involving FGB sensors.

- The predicted load-displacement response was found to match well with the experimental data for crack extensions larger than 35 mm but significant deviation was observed for shorter crack extensions. The crack growth is predicted with a good accuracy (maximum deviation of 3.5mm).

- For an intermediate crack extension of ~25 mm, the axial strain distribution is very well predicted which validates the use of a single cohesive traction separation relationship to predict both the local strain and load-displacement for intermediate to large crack lengths.

Delamination of Asymmetric bonded joints

- R-curves measurements show that the bond layer considerably affects the steady state fracture toughness of the composite with a very significant reduction of the bridging contribution.

- This effect is observable with two types of epoxy adhesives: different curing cycles, elasto-plastic properties, and thicknesses (from 0.1 to 0.4mm). Thus, it is concluded that any epoxy adhesive layer in the surroundings of a crack in this UD composite (SE 70 from Gurit®) can drastically weaken its mode I steady-state fracture behavior.

- Neither the crack position offset nor the postcuring step submitted to the bonded specimens (to cure the adhesive) are responsible for the observed decrease of ERR in the bonded joints.

- The results show that fibres participating to bridging are mostly isolated in the case of joints, whereas they tend to congregate to form bundles in bulk specimens. As fibre bundles require more energy to break than isolated fibres, the observed change of the overall fracture behavior is attributed to the difference of type and magnitude of fibre bridging mechanisms.

- Microscopic observations and morphometric analysis of transversal sections of the specimens show that the COD fluctuations due to bridging are more heterogeneous and intense in bulk than in joint specimens. Largest amplitudes of COD variations are correlated with the presence of significant bundles of fibres, which is consistent with the fibre counting and bundle size analysis. These observations qualitatively explain the observed difference in R-curve behavior of joint vs. bulk specimens

- The results of FE models with and without bridging show that the stress applied to the adhesive layer is high enough to induce plasticity of the epoxy adhesive. However, this plastic deformation cannot energetically explain the change of toughness properties of the composite.

- Results from both modelling (no change of curvature) and the use of the modified scaling function (no impact on the ERR at steady state value) show that the change of compliance of a specimen due to the presence of an adhesive layer has almost no effect on the delamination behavior.

- Identified bridging laws for both bulk and joint configurations exhibit significantly different bridging parameters. The maximum tractions at the crack tip and the length of the bridging zone remain similar but the rate of decay of bridging tractions are significantly higher for joints compared to bulk specimens.

- It is already known that the cohesive law is geometry dependent (and thus not a material property); and this study shows that it is also dependent on the presence of a ductile adhesive layer.

- Cohesive elements simulations of the delamination of an asymmetric joint specimen fit the experimental load displacement curve very well, and predict the crack length with good accuracy. This proves that this method, which consists in identifying a cohesive model for a specific crack position offset in the presence of an adhesive layer, can be used for prediction purposes.

- 3D modelling results show that the elasto-plastic properties of the adhesive create a local perturbation of the stress field around the crack tip. The adhesive layer with adhesive properties acts like a "shield", preventing stresses from spreading continuously.

- The amplitude and the spatial repartition of stresses, especially in the process zone, are affected both vertically and horizontally by the adhesive layer properties. The combined effects of all those changes in the neighbourhood of the crack tip are likely to create a different path for crack propagation, ending up with a different bridging behavior.

Mode Mixity

- DIC measurements on the specimens' edge showed that the shear displacement component during delamination is negligible for both bulk and joint specimens, hence neither the asymmetry nor the adhesive layer induce a mode II component that could affect the fracture behavior of the composite.

- Those experimental observations are confirmed by FE analysis: numerical methods are used to assess that the mode II component is negligible, and thus the mode mixity is not responsible for this change of behavior.

Mechanistic investigations at the microscopic scale

Aiming at understanding why the presence of an adhesive layer triggers a development of a different bridging with more isolated fibres and few bundles, an analysis of processing induced microstructure features is performed. A multiscale FE model with an embedded cell based on real microstructures and material properties is also used to compare the micromechanisms at the onset of damage in joint versus bulk specimens during a mode I loading.

- A clear link is established between the extent of bridging and the roughness of the crack surface: more homogeneous fibre distribution leads to a smoother crack surface and less bridging, whereas a highly heterogeneous microstructure is likely to induce the development of large scale bridging.

- The crack tends to grow in fibres-rich zones, avoiding regions with high resin content. The tortuosity of the crack is mainly controlled by the spatial fibre and matrix distribution.

- A homogeneous microstructure annihilates the difference of delamination behavior observed so far between joint and bulk specimens. The influence of an adhesive layer is far less critical for the development of large scale bridging than a change of microstructure.

- For given microstructure and material properties, a different microcrack initiation pattern is created when the fracture is close to an adhesive layer: a more distributed cracking is observed in the bulk material than in the joint model.

- Significant differences in the crack propagation morphology show that the adhesive layer has indeed a consequent influence on the early damage mechanisms responsible for development of bridging. A significantly more discontinuous crack profile propagating within the centre of the ply is observed for the bulk composite while in the presence of an adhesive the crack is much smoother with fewer discontinuities and it migrates towards the interfaces of the ply.

- Fracture behavior differences observed at the macroscale between bulk and joint specimens can be attributed, at least in part, to the changes of the repartition and amplitude of micromechanisms that trigger the formation of bridging fibre bundles in mode I delamination.

Concept map

Delamination Behavior of UD CFRP

— depends on → **Presence of an adhesive layer**

— depends on → **Heterogeneity of Microstructure**

Presence of an adhesive layer — creates → **Perturbation of Stress field in process**

Perturbation of Stress field in process — triggers → **Microcrack initiation Pattern**

Heterogeneity of Microstructure — controls → **Tortuosity of the crack**

Microcrack initiation Pattern — controls → **Tortuosity of the crack**

Tortuosity of the crack — Leads to the formation of → **Isolated fibres in bridging**

Tortuosity of the crack — Leads to the formation of → **Bundles of fibres in bridging**

Isolated fibres in bridging — affect → **Extent of large Scale Bridging**

Bundles of fibres in bridging — increase → **Extent of large Scale Bridging**

Extent of large Scale Bridging — Strongly correlated with → **Fracture toughness at steady state**

Fracture toughness at steady state — Useful for → **Damage tolerance**

Perspectives

- First of all, ***fatigue tests*** should be considered to determine if an adhesive layer also has an important effect on the development of large scale bridging.

- Perform the same investigation with ***another prepreg carbon epoxy system***, and eventually ***another composite***, such as glass fibre reinforced composite. Since adhesive bonding are used to connect all kinds of composites, it is necessary to investigate the most representative of them.

- Assess the ***loading rate dependency***: the adhesive may become more brittle, leading to a higher load transfer to the crack.

- Take into account the results of those investigations in ***damage tolerance design***.

- Only UD laminates are considered in the present work, but the investigation of the adhesive layer effect should be extended to ***cross-plies***.

- High performance CFRP and toughened epoxy adhesives are mainly used in the aircraft industry, in which the structures incur ***a wide range of temperatures***. Thus experimental tests should be performed at different temperatures. The observed effect of adhesive layer on the delamination behavior of UD laminates can be impaired, intensified, or suppressed at other temperatures.

- The ***effect of moisture*** on the adhesive can also be an important parameter to investigate.

- In this work the only considered surface treatment prior to bonding is the sand blasting. Using another widespread technique for secondary bonding of composite such as ***peel-ply*** would be of great interest.

- In composite patch repairs, the ***composite is often co-cured*** with the adhesive, which might lead to very different properties and delamination behavior.

- Further ***micromechanical approach*** should be considered in order to develop multiscale models with a much larger volume of the composite material (and not only a small subset) to capture the development of bridging bundles such as in [43].

References

[1] **AA. Baker, P.J Callus, S Georgiadis, Falzon, Dutton, KH. Leong.** *An affordable methodology for replacing metallic aircraft panels with advanced composites*, 2002, Composites Part A: Applied Science and Manufacturing, Vol. 33, pp. 687–696.

[2] **F. Benyahia, A. Albedah, B. Bachir Bouiadjra**. *Analysis of the adhesive damage for different patch shapes in bonded composite repair of aircraft structures*. 2014, Materials & Design, Vol. 54, pp. 18-24.

[3] **A.J. Brunner, B.R.K. Blackman, P. Davies.** *A status report on delamination resistance testing of polymer–matrix composites.* 2008, Engineering Fracture Mechanics, pp. 2779–2794.

[4] **Tay, TE.** *Characterization and analysis of delamination fracture in composites: An overview of developments from 1990 to 2001. 2003*, Appl Mech Rev, Vol. 56.

[5] **A.A. Baker**. *A summary of work on applications of advanced fibre composites at the Aeronautical Research Laboratories*, Australia, Composites, Volume 9, Issue 1, 1978, Pages 11-16.

[6] **P. Chalkley, A.A. Baker**, *Development of a generic repair joint for certification of bonded composite repairs*, International Journal of Adhesion and Adhesives, Volume 19, Issues 2–3, April 1999, Pages 121-132.

[7**] G. J. Tsamasphyros, G. N. Kanderakis, D. Karalekas, D. Rapti, E . E . Gdoutos, D. Zacharopoulos and Z . P. Marioli-Riga**, *Study of composite patch repair by analytical and numerical methods*, Fatigue & Fracture of Engineering Materials & Structures 24(10):631 – 636, 2001.

[8] **Mahdi, S., Kinloch, A.J., Matthews, F.L. and Crisfield, M.A.** *The Mechanical Performance of Repaired Stiffened Panels. Part I. Experimental Characterisation.* 5, 2002, Composites Part B: Engineering, Vol. 33, pp. 343-354.

[9] **Breitzman TD, Iarve EV, Cook BM, Schoeppner GA, Lipton RP**. *Optimization of a composite scarf repair patch under tensile loading.* Compos Part A: Appl Sci Manuf 2009;40:1921–30.

[10] **Brighenti Roberto, Carpinteri Andrea, Vantadori Sabrina.** *A genetic algorithm applied to optimisation of patch repair for cracked plates*. Comput Meth Appl Mech Eng 2006;196:466–75.

[11] **Rachid Mhamdia, Serier B, Bachir Bouiadjra B, Belhouari M.** *Numerical analysis of the patch shape effects on the performances of bonded composite repair in aircraft structures.* Compos: Part B 2012;43:391–7.

[12] **Hexcel Composite®,** *Composite repair guide*, 1999

[13] **Qing XP, Beard SJ, Kumar A, Hannum R.** *A real-time active smart patch system for monitoring the integrity of bonded repair on an aircraft structure.* Smart Mater Struct 2006;5:66–73.

[14]**D. Ouinas, B. Bouiadjra , B. Serier.** *The effects of disbands on the stress intensity factor of aluminum panels repaired using composite materials.* Compos Struct 2007;78:278–84.

[15] **D. Ouinas, B.** Bouiadjra , T. Achour, N. Benderdouche. *Influence of disband on notch crack behavior in single bonded lap joints.* Mater Des 2010;31:4356–62.

[16] **Chin-Teh Sun and Zhihe Jin.** *Fracture Mechanics*, 2012, Elsevier

[17] **S. Sridharan.** *Delamination behavior of composites* – Woodhead Publishing, 2008.

[18] **S. Stutz, J. Cugnoni, J. Botsis.** *Crack – fiber sensor interaction and characterization of the bridging tractions in mode I delamination.* 2011, Engineering Fracture Mechanics, Vol. 78, pp. 890-900.

[19] **S.M. Spearing, A.G. Evans.** *The role of fiber bridging in the delamination resistance of fiber reinforced composites.* 1992, Acta metall, mater, Vol. 40, pp. 2191-2199.

[20] **Cox, B.N., Marshall, D.B.** *The determination of crack bridging forces.* 1991, International Journal of Fracture, Vol. 49.

[21] **Farmand-Ashtiani, E., J. Cugnoni, and J. Botsis.** *Specimen thickness dependence of large scale fiber bridging in mode I interlaminar fracture of carbon epoxy composite.* International Journal of Solids and Structures 55 (2015): 58-65.

[22**] Griffith AA.**, *The phenomena of rupture and flow in solids.* Philosophical Transactions of the Royal Society of London, Sereis A, 221:163-198, 1921.

[23] **G. R. Irwin**, *Analysis of Stresses and Strains near the End of a Crack Traversing a Plate*. Journal of Applied Mechanics, Vol. E24, 1957

[24] **Brett, M.A. de Oliveira.** *Prediction of performance of adhesively bonded composite joints.* 2011. PhD thesis.

[25] **Xie D, Biggers SB.** *Progressive crack growth analysis using interface element based on the virtual crack closure technique.* 2006, Finite Elem Anal Des, Vol. 42, pp. 977–984.

[26] **R., Krueger**. *The virtual crack closure technique: history, approach and applications*.2004, Appl Mech Rev, Vol. 57, pp. 109-143.

[27] **ASTM D5528-03**. *Standard Test Method for Mode I Interlaminar Fracture Toughness of Unidirectional Fiber-Reinforced Polymer Matrix Composites,* 2006.

[28] **ASTM D 6671/D 6671M – 06** *Standard Test Method for Mixed Mode I-Mode II Interlaminar Fracture Toughness of Unidirectional Fiber Reinforced Polymer Matrix Composites*, 2006

[29] **Martin RH, Davidson BD.** *Mode II fracture toughness evaluation using four point bend, end notched flexure test.* 1999, Plastics,Rubber and Composites, Vol. 28, pp. 401-406.

[30] **M. Shahverdi, A. P. Vassilopoulos, T. Keller.** *A phenomenological analysis of Mode I fracture of adhesively-bonded pultruded GFRP joints.* 2011, Engineering Fracture Mechanics, pp. 2161–2173.

[31] **Ye Zhang, A. P. Vassilopoulos, T. Keller.***Mode I and II fracture behavior of adhesively-bonded pultruded.* 2010, Engineering Fracture Mechanics, Vol. 77, pp. 128-143.

[32] **M. Shahverdi, A. P. Vassilopoulos, T. Keller.** *Modeling effects of asymmetry and fiber bridging on Mode I fracture behavior of bonded pultruded composite joints.* 2013, Engineering Fracture Mechanics, Vol. 99, pp. 335–348.

[33] **Choupani, Naghdali.** *Experimental and numerical investigation of the mixed-mode delamination in Arcan laminated specimens.* 1-2, 2008, Vol. Materials Science and Engineering: A, pp. 229-242.

[34] **N. Blancoa, E.K. Gamstedt, J. Costa , D. Trias.** *Analysis of the mixed-mode end load split delamination test.* 2006, Composite Structures, Vol. 76, pp. 14-20.

[35] **V. Mollón, J. Bonhomme, J. Viña, A. Argüelles.** *Theoretical and experimental analysis of carbon epoxy asymmetric dcb specimens to characterize mixed mode fracture toughness*. 2010, Polymer Testing , Vol. 29, pp. 766-770.

[36] **Williams, JG.** *On the calculation of energy release rates for cracked laminates.* 1988, International Journal of Fracture, Vol. 36, pp. 101-119.

[37] **Hutchinson JW, Suo Z.** *Mixed mode cracking in layered materials.* 1992, Adv Appl Mech, Vol. 29, pp. 64-122.

[38] **ISO 25217** - *Determination of the mode 1 adhesive fracture energy of structural adhesive joints using double cantilever beam and tapered double cantilever beam specimens.* 2009.

[39] **ESIS TC4 Protocol** - *The determination of the mode II fracture resistance, GIIC, of unidirectional fibre-composites using the calibrated end loaded split (C-ELS) test and an effective crack length approach.* (2006)

[40] **M. Li, S. Ghosh, O. Richmond.** *An experimental–computational approach to the investigation of damage evolution in discontinuously reinforced aluminum matrix composite.* Acta Materialia, Volume 47, Issue 12, 29 September 1999, Pages 3515-3532   .

[41] **Isaac M. Daniel, Ori Ishai.** *Engineering Mechanics of Composite Materials,* 2nd Edition Oxford University Press, 1994.

[42] **Stutz, S., J. Cugnoni, and J. Botsis**, *Studies of mode I delamination in monotonic and fatigue loading using FBG wavelength multiplexing and numerical analysis.* Composites Science and Technology, 2011. **71**(4): p. 443-449.

[43] **L.P.Canal, M. Alfano, J. Botsis**, *A multi-scale based cohesive zone model for the analysis of thickness scaling effect in fiber bridging*, Composites Science and Technology, 139, pp. 90-98, 2017.

[44**] Salvatore Torquato**, *Random heterogeneous materials*, Springer, 2001.

[45] **G. Frossard, J. Cugnoni, T. Gmür, and J. Botsis**, *Mode I interlaminar fracture of carbon epoxy laminates: Effects of ply thickness*, 2016, Composites Part A, Volume 91, Part 1, December 2016, Pages 1–8.

[46] **L. P. Canal, C. Gonzalez, J. Segurado, J. LLorca**, *Intraply fracture of fiber-reinforced composites: Microscopic mechanisms and modeling*, 2012, Composites Science and Technology, Volume 72, Issue 11, 28 June 2012, Pages 1223-1232.

[47] **S. Kohler, J. Cugnoni, J. Botsis**, *3D Microcracking evolution in thin ply composites under tensile loading: experiments and anaylsis, Proceedings of the 8th* International Conference on Composites Testing and Model Identification, 2017.

[48] **Carlos Gonzalez, Javier LLorca**, *Multiscale modeling of fracture in fiber-reinforced composites,* Acta Materialia 54 (2006) 4171–4181.

[49] **M. Borotto**, *Bridging effects on Mixed Mode delamination: experiments and numerical simulation*, PhD thesis, Lausanne: EPFL, 2016.

[50] **L. Sorensen, John Botsis, Thomas Gmür, Joël Cugnoni**, *Delamination detection and characterisation of bridging tractions* using long FBG optical sensors , Composites Part A: Applied Science and Manufacturing, Volume 38, Issue 10, October 2007, Pages 2087-2096.

[51] **Behzad D. Manshadi, Anastasios P. Vassilopoulos, John Botsis**, *A combined experimental/numerical study of the scaling effects on mode I delamination of GFRP*, Composites Science and Technology , Volume 83, 28 June 2013, Pages 32–39.

[52] **Michel Del Pedro, Thomas Gmür, John Botsis,** *Introduction à la mécanique des solides et des structures*, PPUR presses polytechniques, 3ème édition, 2012.

[53] **L. Sorensen, J. Botsis, Th. Gmür, L. Humbert**, *Bridging tractions in mode I delamination: Measurements and simulations, Composites Science and Technology, Volume 68, Issue 12, September 2008, Pages 2350-2358.*

[54] **N. Shibata, S. Shibata, and T. Edahiro.** *Refractive index dispersion of lightguide glasses at high temperature*. Electronics Letters, 17(8):310–311, 1981.

[55] **S. Kohler, J. Cugnoni, R. Amacher, J. Botsis**, *Damage mechanisms in thin-ply composites: free edge/bulk measurements and multiscale modelling.* Proceedings of the 17th European Conference on Composite Materials, Germany, 2016.

[56] **De Morais, A., et al.,** *Mode-I interlaminar fracture of carbon/epoxy cross-ply composites.* Composites Science and Technology, 2002. 62(5): p. 679-686.

[57] **Sørensen, B.F. and T.K. Jacobsen**, *Large-scale bridging in composites: R-curves and bridging laws.* Composites Part A: Applied Science and Manufacturing, 1998. 29(11): p. 1443-1451.

[58] **Nairn, J.A.**, *Analytical and numerical modeling of R curves for cracks with bridging zones.* International journal of fracture, 2009. 155(2): p. 167-181.

[59] **Rice, J.R.**, *A path independent integral and the approximate analysis of strain concentration by notches and cracks*, 1967, DTIC Document.

[60] **Rice, J.R.,** *A path independent integral and the approximate analysis of strain concentrations by notches and cracks.* Journal of Applied Mechanics, 1968. 35: p. 379-386.

[61] **Anderson, T.L. and T. Anderson,** *Fracture mechanics: fundamentals and applications*2005: CRC press.

[62] **Davies, P., et al.,** *Measurement of G IC and G IIC in carbon/epoxy composites.* Composites Science and Technology, 1990. 39(3): p. 193-205.

[63] **Davies, P., et al.,** *Round-robin interlaminar fracture testing of carbon-fibre-reinforced epoxy and PEEK composites.* Composites Science and Technology, 1992. 43(2): p. 129-136.

[64] **N. Nasri, J. Cugnoni, J. Botsis**, *Effect of adhesive layer on the mode I interlaminar delamination of unidirectional cfrp bonded joints,* Proceedings of the 17th European Conference on Composite Materials, Germany, 2016.

[65] **Sorensen, L., T. Gmür, and J. Botsis**, *Residual strain development in an AS4/PPS thermoplastic composite measured using fibre Bragg grating sensors.* Composites Part A: Applied Science and Manufacturing, 2006. 37(2): p. 270-281.

[66] **Nairn, J.,** *Fracture mechanics of composites with residual thermal stresses.* Journal of Applied Mechanics, 1997. 64(4): p. 804-810.

[67] **Schizas, C., et al.,** *Monitoring of non-homogeneous strains in composites with embedded wavelength multiplexed fiber Bragg gratings: A methodological study.* Composite structures, 2012. 94(3): p. 987-994.

[68] **De Morais, A**., *A new fibre bridging based analysis of the Double Cantilever Beam (DCB) test.* Composites Part A: Applied Science and Manufacturing, 2011. 42(10): p. 1361-1368.

[69] Vic-2D software testing guide, 2009.

[70] **Bing Pan, Huimin Xie, Zhaoyang Wang, Kemao Qian, and Zhiyong Wang**, *Study on subset size selection in digital image correlation for speckle patterns,* 2008 Optical Society of America.

[71] **C. González, .J. Segurado., J. LLorca**, Numerical *simulation of elasto-plastic deformation of composites: evolution of stress microfields and implications for homogenization models,* Journal of the Mechanics and Physics of Solids, Volume 52, Issue 7, July 2004, Pages 1573-1593.

[72] http://www.fbgs.com/technology/fbg-principle/

Appendix 1: Matlab code to obtain the Correction vector

```matlab
% strains
clear all
close all

%Skript to treat MPX data.

% Load data
dFBG0=load('initialfbgstrains4PB.txt');
dFBG=load('fbgstrains4PB.txt');
OLCR=flip([145.94 142.74 139.88 136.76 134.09 131.00 127.99
124.94 122.06 118.88]);

%Computation of strains
f0=mean(dFBG0(:,2:end));
nFBG=10;
for k=1:nFBG
    A(:,1+k)=(dFBG(:,k+1)-f0(k))/f0(k)/0.7852; % the parameter
0.7852 is (1-pe)
end
A(:,1)=dFBG(:,1);

%filter fbg data
n=10;
h = fspecial('average', n);
for i=1:nFBG
    A(:,1+i)=n*filter2(h,A(:,1+i));
end

%slope calculee quand c'est lineaire: entre t=60 et t=90s
ind1=find(A(:,1)<=60,1,'last');
ind2=find(A(:,1)<=90,1,'last');
fit=[];
for i=1:10
    plot(A(:,1),A(:,i+1));
    hold on
    p=A(ind1:ind2,1)\A(ind1:ind2,i+1);
    legendInfo{i}=['FBG #',num2str(i),'    ',num2str(p)];
    fit(i)=p;
    xlabel('time')
    ylabel('fbg strains')

end
% legend(legendInfo)
hold off
```

```matlab
figure,
plot(OLCR, fit/mean(fit),'o')
xlabel('FBG position')
ylabel('slope normalized by mean')
hold on

%vecteur Correction (coefficient de transfert) à multiplier
pour chaque fbg

Correction=(fit/mean(fit));
%Correction=[0.980607896811321  0.990631802542389
0.994259075446780   1.00422227742641    0.994775970933551
1.00169157329128    1.01388680416760    1.01028061731097
1.00964398206970];
%fit/mean(fit);

%Correction of strains
for k=1:nFBG
    B(:,k+1)=(A(:,k+1)/Correction(k));
    B(:,1)=A(:,1);
end

%CORRECTED slope calculee quand c'est lineaire: entre t=60 et
t=90s
ind1=find(B(:,1)<=60,1,'last');
ind2=find(B(:,1)<=90,1,'last');
fitCorr=[];
figure
for i=1:10
    plot(B(:,1),B(:,i+1));
    hold on
    v=B(ind1:ind2,1)\B(ind1:ind2,i+1);
    legendInfo{i}=['FBG #',num2str(i),'    ',num2str(v)];
    fitCorr(i)=v;
    xlabel('time')
    ylabel('CORRECTED fbg strains')
end
legend(legendInfo)
hold off

figure,
plot(OLCR, fitCorr/mean(fitCorr),'o')
xlabel('FBG position')
ylabel('CORRECTED slope normalized by mean')
```
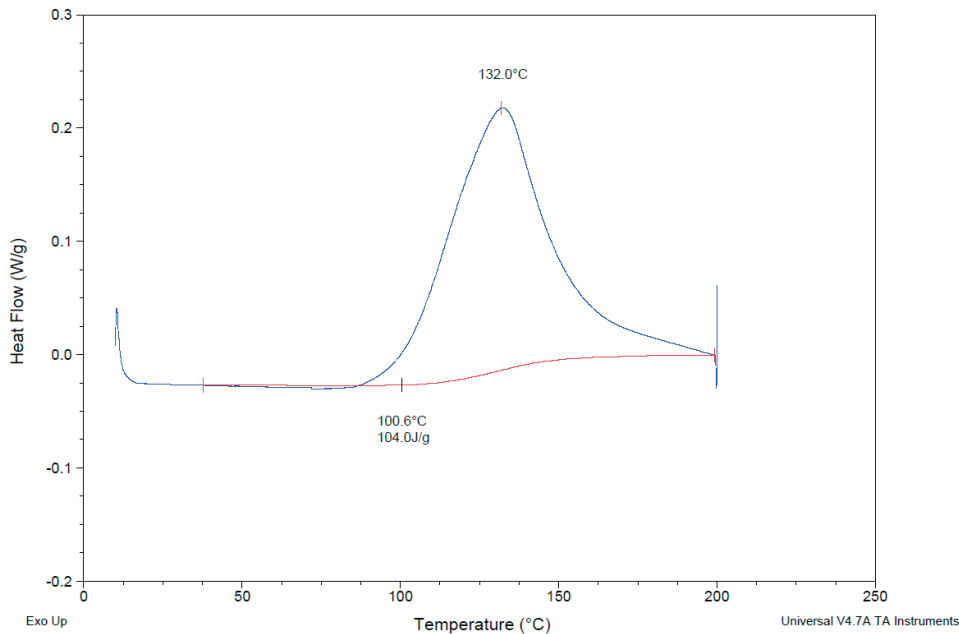
Appendix 2 : DSC measurements

Sample: uncured prepreg P2
Size: 7.0600 mg
Method: CFRP-SE70

DSC

File: D:...\ech3-uncured_pregSE70_June2016.001
Operator: NN
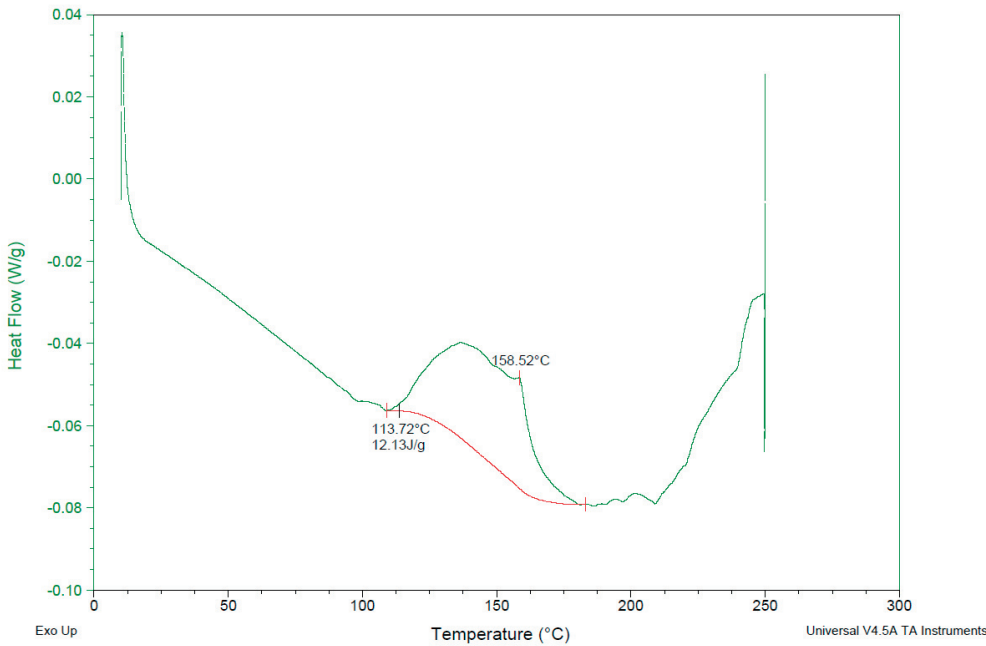Run Date: 07-Jul-2016 15:31
Instrument: DSC Q100 V9.9 Build 303

132.0°C

100.6°C
104.0J/g

Heat Flow (W/g)

Exo Up

Temperature (°C)

Universal V4.7A TA Instruments

Sample: cured prepreg P2
Size: 8.2300 mg
Method: CFRP-SE70

DSC

File: ech1-dcb_sym_juin_2016_new_preg_bad.001
Operator: NN
Run Date: 07-Jul-2016 11:59
Instrument: DSC Q100 V9.9 Build 303

158.52°C

113.72°C
12.13J/g

Heat Flow (W/g)

Exo Up

Temperature (°C)

Universal V4.5A TA Instruments

133

Sample: uncured prepreg P1
Size: 7.9500 mg
Method: CFRP-SE70

DSC

Operator: NN
Run Date: 07-Jul-2016
Instrument: DSC Q100 V9.9 Build 303

131.79°C

100.33°C
106.0J/g

Exo Up

Universal V4.5A
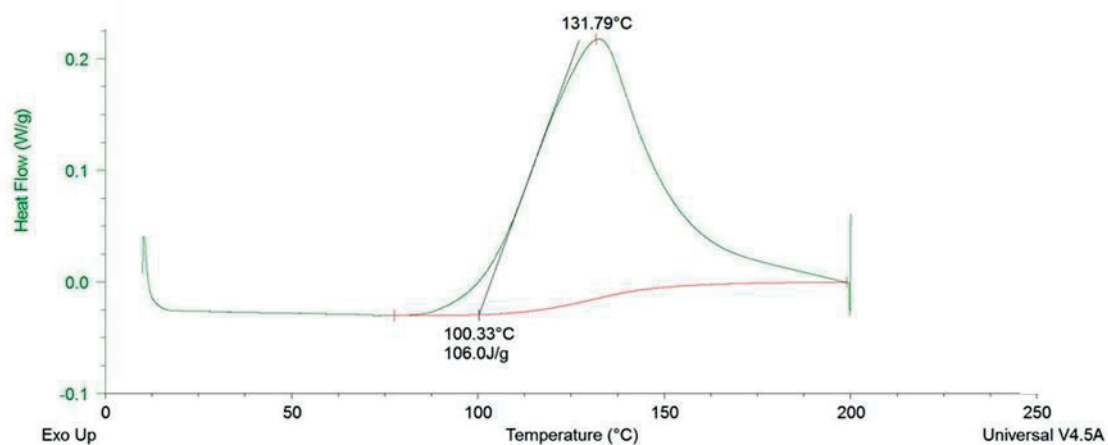
Sample: cured Prepreg P1
Size: 7.6800mg
Method: CFRP-SE70

DSC

Operator: NN
Run Date: 07-Jul-2016
Instrument: DSC Q100 V9.9 Build 303

134.76°C

108.85°C
8.021J/g

Exo Up

134
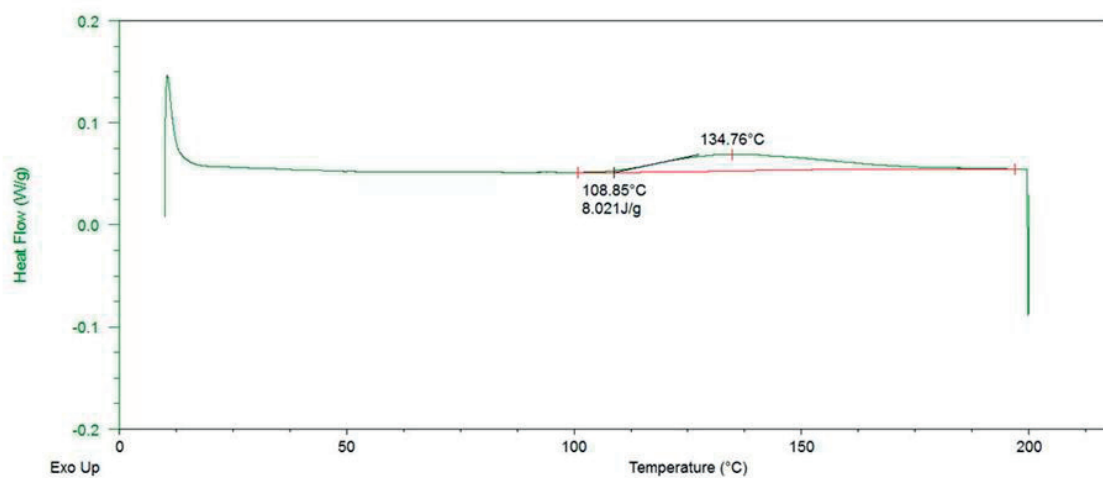
Curriculum vitae - NASSIMA NASRI

PERSONNAL DATA

Address: Chemin des Noutes 7
                    1023 Crissier
                    Switzerland
Telephone: ++ 41 789 65 40 49
Email: nassima.nasri@hotmail.fr
Birth date: 29/05/1989 - 27 years old
Nationality: Algerian and French

EDUCATION

2013-2017
Ph.D. Candidate
Laboratory of Applied Mechanics and Reliability analysis.
Ecole polytechnique Fédérale de Lausanne. **(EPFL),** *Lausanne, Switzerland***.**

2010-2012
European M.Sc. in Material Science and Engineering. European School of materials science and engineering (EEIGM), *Nancy*, *France*

2011
Erasmus Semester at Etseib, Universitat Politècnica de Catalunya
Part of my M. Sc. in Material Science,   *Barcelona, Spain*

2007 – 2010
B.Sc. in Material Science and Engineering, European School of Materials Science and Engineering (EEIGM)   *Nancy, France*

2007
Baccalauréat S (with major in maths and physics) with distinction
Secondary School Marc Chagall   *Reims, France*

LANGUAGE PROFENCIENCY

French, mother tongue.
English, very good level (C1), Certificate of Advanced English (CAE).
German, very good level (B2 – C1), 10 years of studies, several trips, 1 year in Germany.
Spanish, Good level (B2).

WORK EXPERIENCE

2012-2013
3 months internship - Laboratory of Applied Mechanics and Reliability analysis.
(EPFL), *Lausanne, Switzerland*. Debond growth assessment in sandwich structures

2011-2012
1 year Internship - Airbus Operations GmbH,   ***Bremen, Germany***
Subject: Fracture Mechanics: Development of Fracture Toughness
Test Methods for CFRP Bonded Joints. Part of my MSc.

01/2011
1 month Internship - MERSEN, R&D department on graphite and metals
Pagny-sur-Moselle, France
Highlights: viscosimetry, tensile tests, bending tests, polishing and control quality.

Summer 2010
1 month internship - Thin Film Centre at the University of the West of Scotland,
Paisley, Scotland
Subject : Determination of the ageing of thin coat of palladium with
Kelvin's probe. Tests realized for the company **Johnson and Johnson**

Summer 2009
Six weeks training in the Hochschul-Sozialwerk**,   *Wuppertal, Germany***

2008-2010
Chess instructor for primary school pupils, part-time employment
with CEN "Contrat Educatif Nancéen". ***Nancy, France***

COMPUTER SKILLS

Microsoft Office package (Word, Excel, PowerPoint, etc), Abaqus, Matlab,
Basic knowledge of Catia V, Solidworks, LabView,

Conference proceedings

N. Nasri, J. Cugnoni, J. Botsis, , *Effect of adhesive layer on the mode I interlaminar delamination of unidirectional cfrp bonded joints,* 17th European Conference on Composite Materials, Germany, 2016.

E. Farmand-Ashtiani, **N. Nasri**, J. Cugnoni, J. Botsis, *"Debond growth assessment in GFRP-balsa sandwich structures",* 6th International Conference on Composites Testing and Model identification, April 2013, Aalborg, Denmark.